PTB bericht
Wissenschaftliche Veröffentlichungen

Diss-25
Januar 2026

Dissertation

Alexander Putz

Particle Characterization in Flow Cytometry – modelling new measurement approaches

ISSN 2941-1297
ISBN 978-3-944659-57-2

DOI 10.7795/110.20260122

Alexander Putz

Particle Characterization in Flow Cytometry – modelling new measurement approaches

Dissertationen
PTB-Diss-25

Braunschweig, Januar 2026

ISSN 2941-1297
ISBN 978-3-944659-57-2

DOI 10.7795/110.20260122

Empfohlene Zitierweise/recommended citation

Putz, A., 2026. *Particle Characterization in Flow Cytometry – modelling new measurement approaches*. Dissertation, Technische Universität Berlin.
Braunschweig: Physikalisch-Technische Bundesanstalt.
PTB-Bericht Diss-25. ISBN 978-3-944659-57-2.
Verfügbar unter: https://doi.org/10.7795/110.20260122

Herausgeber:
Physikalisch-Technische Bundesanstalt
ISNI: 0000 0001 2186 1887

Presse und Öffentlichkeitsarbeit

Bundesallee 100
38116 Braunschweig

Telefon: (05 31) 592-93 21
Telefax: (05 31) 592-92 92
www.ptb.de

Particle Characterization in Flow Cytometry

modeling new measurement approaches

vorgelegt von
Alexander Putz, M. Sc.

an der Fakultät II - Mathematik und Naturwissenschaften
der Technischen Universität Berlin
zur Erlangung des akademischen Grades

Doktor der Naturwissenschaften
Dr. rer. nat.

genehmigte Dissertation

Promotionsausschuss:
Vorsitzender: Prof. Dr. Dieter Breitschwerdt
Gutachter: Prof. Dr. Holger Stark
Gutachter: Prof. Dr. Rainer Macdonald
Gutachter: Prof. Dr. Oliver Otto
Tag der wissenschaftlichen Aussprache: 01. Dezember 2025

Berlin 2025

https://doi.org/10.7795/110.20260122

https://doi.org/10.7795/110.20260122

Zusammenfassung

Durchflusszytometer sind entscheidend für die Analyse von Blut und Mikropartikeln und ein fester Bestandteil heutiger Medizinlabore. Es besteht jedoch weiterhin ein großer Bedarf darin die Nachweisgrenze hin zu kleineren Partikeln zu verschieben, Forminformationen über die Partikel zu gewinnen und verbesserte Koinzidenzkorrekturverfahren zu entwickeln um die Messgenauigkeit weiter zu erhöhen.

Um die absolute Größe von (Sub-)Mikropartikeln zu messen, müssen die optischen Parameter des Durchflusszytometers vorher bestimmt worden sein. Eine neue, einfache und zeitsparende Methode zur Bestimmung dieser Parameter wurde entwickelt, bei der nur grobe Startwerte der optischen Parameter benötigt werden. Die wahren Werte der optischen Parameter werden mittels Differential Evolution durch die Optimierung von theoretisch berechneter Streulichtintensität zu gemessener bestimmt. Für die Vorwärtsrichtung liefert diese Methode stabile Ergebnisse mit geringer Streuung, während die Streuung in der Seitwärtsrichtung größer ausfällt. Eine genaue Validierung ist jedoch nur schwer möglich.

Im Gegensatz zu herkömmlichen Durchflusszytometern, die nur einen Intensitätswert pro detektiertem Partikel erfassen, wurde in dieser Arbeit der gesamte Durchgang eines Partikels durch den Laser zeitlich erfasst. Durch die Auswertung der zeitlichen Breite des Pulses können Koinzidenzen von gleichgroßen Partikeln deutlich präziser erkannt und korrigiert werden als z.B. mit der Pulsfläche alleine. Unter Zuhilfenahme der Schiefe des Pulses konnten darüber hinaus Koinzidenzen von deutlich unterschiedlich großen Partikeln größtenteils detektiert werden, was mit den bisher üblichen Koinzidenzkorrekturverfahren nicht möglich ist. Ein Vorteil dieser Methode ist der Erhalt des Zugriffs auf die individuellen Koinzidenzen und die Anwendbarkeit der Koinzidenzkorrektur für Messungen in denen keine Poisson-Verteilung vorliegt.

Zusätzlich wurde eine statistische Koinzidenzkorrektur entwickelt, welche auf der exponentiellen Wartezeitverteilung von aufeinanderfolgenden Events basiert. Aus der Wartezeit für Events, die größer als eine definierte Abschneidezeit sind, kann über die Selbstähnlichkeit der Wartezeitverteilung auf die Wartezeit der gesamten Verteilung geschlossen werden und damit auf die statistisch korrekte Anzahl an Zählereignissen. Vorteilhaft an dieser Methode ist, dass nur eine Messung für die Koinzidenzkorrektur vonnöten ist, ganz im Vergleich zur Verdünnungsreihe bei der mindestens vier Messreihen mit unterschiedlichen Verdünnungen gefordert sind.

Durch die Entwicklung von bildgebenden Durchflusszytometern wurde es möglich in Seitwärtsrichtung Streulicht abzubilden. Für sphärische Partikel erhält man unerwarteterweise anstelle einer kreisförmigen Abbildung mehrere helle Flecken mit einem Abstand, der in etwa dem des Durchmessers des Partikels entspricht. Es konnte nachgewiesen werden, dass die hellen Flecken in Seitwärtsrichtung für sphärische Polystyrol-Mikropartikel mit den aus anderen

https://doi.org/10.7795/110.20260122

Bereichen bekannten *Glare Points* erklärt werden können. Ein Abbildungsmodell basierend auf einer idealen Linse und dem Rayleigh-Sommerfeld Beugungsintegral wurde entwickelt, um dieses Phänomen zu beschreiben. Theoretische Untersuchungen zu deformierten Kugeln zeigten, dass bei einem hohem Brechungsindex von z.B. Polystyrol weitere regelmäßige helle Flecken erscheinen, die bei undeformierten Kugeln nicht sichtbar sind.

Abschließend wurde die Eignung eines Quadrantendetektors zur Unterscheidung von Kugeln und nicht-Kugeln theoretisch untersucht. Hierfür wurde ein Verhältnis R als Maß für die Asphärizität definiert. Es stellte sich heraus, dass dieses sehr gut geeignet sein kann, da die Reihenfolge der Seitenverhältnisse von verschiedenen Teilchentypen auch der des Verhältnisses R über einen weiten Größenbereich entspricht. Vergrößert man die numerische Apertur, wird auch das Verhältnis R vergrößert, was die Empfindlichkeit für Variationen im Seitenverhältnis weiter erhöht.

https://doi.org/10.7795/110.20260122

Abstract

Flow cytometers are essential tools for the analysis of blood and microparticles and are a standard component of modern medical laboratories. However, there remains a strong need to lower the detection limit toward smaller particles, to extract shape-related information from the particles, and to develop improved coincidence correction methods to further enhance measurement accuracy.

To measure the absolute size of (sub-)microparticles, the optical parameters of the flow cytometer must be known in advance. A new, simple, and time-efficient method has been developed to determine these parameters, which only requires rough initial estimates. The true values of the optical parameters are determined using Differential Evolution by optimizing the agreement between theoretically calculated and measured scattered light intensity.

For the forward direction, this method provides stable results with low variance, whereas the variance in the sideward direction is higher. However, precise validation remains difficult.

In contrast to conventional flow cytometers that capture only a single intensity value per detected particle, here the entire transit of a particle through the laser over time is recorded. By evaluating the temporal width of the pulse, coincidences of similarly sized particles can be detected and corrected significantly more accurately than with, for example, the pulse area alone. Using the skewness of the pulse, even coincidences of particles with significantly different sizes could largely be detected—something not possible with previously established coincidence correction techniques. An advantage of this method is the ability to access individual coincidence events and to apply coincidence correction to measurements that do not follow a Poisson distribution.

In addition, a statistical coincidence correction method was developed, based on the exponential waiting time distribution of successive events. From the waiting times of events that exceed a defined cut-off time, the waiting time of the full distribution can be inferred using the self-similarity property of the waiting time distribution—thus enabling determination of the statistically correct number of counting events. A key advantage of this method is that only a single measurement is required for coincidence correction, unlike dilution series which typically requires at least four different dilution steps.

With the development of imaging flow cytometers, it became possible to image scattered light in the sideward direction. For spherical particles, surprisingly, instead of a circular image, several bright spots appear, spaced approximately by the particle diameter.

It was demonstrated that these bright spots observed in the sideward direction for spherical polystyrene microparticles correspond to the from other fields known *Glare Points*. An imaging model based on an ideal lens and the Rayleigh-Sommerfeld diffraction integral was developed to describe this phenomenon. Theoretical investigations of deformed spheres showed that, for

https://doi.org/10.7795/110.20260122

high refractive indices such as polystyrene, additional evenly spaced bright spots appear that are not visible in undeformed spheres.

Finally, the suitability of a quadrant detector for distinguishing spherical from non-spherical particles was theoretically investigated. A ratio R was defined as a measure of asphericity. It was found that this ratio is highly suitable, as the order of aspect ratios for different particle types closely matches the order of R over a wide size range. Increasing the numerical aperture also increases the ratio R, which further improves sensitivity to variations in the aspect ratio.

https://doi.org/10.7795/110.20260122

Dedicated to the doctors and nursing staff who tirelessly care for patients with autoimmune diseases. Without their dedication, this thesis would not have been possible. May advanced cytometers ease your invaluable work.

https://doi.org/10.7795/110.20260122

https://doi.org/10.7795/110.20260122

Danksagung

Zuerst möchte ich meiner Frau danken, die während meiner Doktorandenzeit von meiner Partnerin zu meiner Ehefrau wurde. Der Satz "In diesem Jahr bin ich aber wirklich fertig mit der Doktorarbeit" wurde schließlich zu einem "Jetzt bin ich fertig". Danke fürs Durchhalten in all den ungewissen Jahren.

Weiterhin möchte ich meinem Mentor, Dr. Martin Hussels, danken, der mir vom ersten bis zum letzten Tag mit Rat und Tat zur Seite stand. Außerdem möchte ich Dr. Jonas Gienger danken, der mir besonders bei mathematischen und theoretischen Fragen enorm geholfen hat. Seine Expertise und sein Ideenreichtum auf diesem Gebiet sind einfach außergewöhnlich.

Ich möchte mich auch ausdrücklich bei Herrn Prof. Dr. Rainer Macdonald, meinem (ehemaligen) Fachbereichsleiter von 8.3., für seine Zuversicht, Rückendeckung und seinen Einsatz für mich bedanken, als ich gesundheitlich sehr zu kämpfen hatte. Ich danke ihm außerdem für das großzügige Korrekturlesen der Arbeit.

Herrn Prof. Dr. Holger Stark danke ich dafür, dass er sich bereit erklärt hat, mein universitärer Betreuer zu sein, Herrn Prof. Dr. Oliver Otto als meinen zweiten Gutachter und Herrn Prof. Dr. Dieter Breitschwerdt dafür, dass er den Vorsitz der Prüfungskommission übernimmt.

LUM GmbH möchte ich für die gute Zusammenarbeit danken und die Möglichkeit Messdaten von ihren Zytometern zu verwenden.

Danken möchte ich auch Susanne Engel, Alexander Hoppe und erneut Dr. Martin Hussels, welche viele der in dieser Arbeit verwendeten Messungen mit großer Sorgfalt durchgeführt hat.

Meinen Mitdoktoranden Yannik Hein, Christian Goerke, Samira Gulich und Leila Motamed-Jahromi danke ich für die vielen tollen und lustigen Stunden im Büro. Unvergessen bleibt die Organisation des ersten online PhD-Days während des Corona-Lockdowns 2021, der unheimlich viel Zeit gekostet hat, aber emotional ein großer Gewinn war.

Diese Doktorarbeit wurde aus einem TranMeT Projekt mit der Projektnummer *TranMeT Projekt 2019-II-02* finanziert.

https://doi.org/10.7795/110.20260122

https://doi.org/10.7795/110.20260122

Table of Contents

https://doi.org/10.7795/110.20260122

https://doi.org/10.7795/110.20260122

List of Figures

https://doi.org/10.7795/110.20260122

https://doi.org/10.7795/110.20260122

https://doi.org/10.7795/110.20260122

https://doi.org/10.7795/110.20260122

https://doi.org/10.7795/110.20260122

https://doi.org/10.7795/110.20260122

List of Tables

https://doi.org/10.7795/110.20260122

https://doi.org/10.7795/110.20260122

Abbreviations

FPGA Field Programmable Gate Array

PMT Photomultiplier Tube

NA Numeric Aperture

FSC Forward Scatter

SSC Side Scatter

.tdms Technical Data Management Streaming (file format)

ADDA (Amsterdam) Discrete-Dipole Approximation

GLMT Generalized Lorenz-Mie Theory

LMT Lorenz-Mie Theory

MPI Message Passing Interface

FFT Fast-Fourier Transform

SNR Signal-to-Noise Ratio

SPES Single Particle Extinction and Scattering

CV Coefficient of Variation

DIN Deutsche Industrie Norm

ISO International Organization for Standardization

https://doi.org/10.7795/110.20260122

https://doi.org/10.7795/110.20260122

1

Introduction

Who would have thought in the 13. century that the discovery of glass stones, used as visual aids for better reading, would open up a completely new perspective on the world. Experiments with multiple combined lenses eventually led to the invention of the first microscope by Hans and Zacharias Janssen in 1590 [2]. While the naked eye is limited by natural constraints, the precise shaping of lenses made it now possible to magnify tiny structures that had previously remained invisible and would have been unreachable. This marked the beginning of a scientific revolution that fundamentally changed our understanding of biology, medicine, and physics. About 100 years later, in 1674 Antonie van Leeuwenhoek rendered the first illustration of red blood cells, described by him as "red corpuscles" [3]. After Antonie van Leeuwenhoek's first detailed observation of red blood cells, the pace of discoveries in microscopy and hematology began to accelerate. Scientists soon realized that blood was far more complex than just a simple red fluid. In the 18th century, William Hewson, often regarded as the father of hematology, uncovered the role of fibrin in blood clotting and provided a clearer distinction between red and white blood cells [4]. By the 19th century, researchers like Rudolf Virchow further advanced the field by identifying and classifying blood disorders, including leukemia [5]. With each technological improvement in microscopy and staining techniques, scientists gained deeper insights into the cellular composition of blood, paving the way for modern hematology and transfusion medicine. An important step in this process was the invention of the Coulter counter in 1953 by Wallace H. Coulter [6], the very first cytometer. This device revolutionized hematology by enabling rapid and automated blood cell counting. It works on the principle of electrical impedance: as cells pass through a small aperture submerged in an electrically conductive fluid, they momentarily change the resistance of an applied electrical current. These changes, or pulses, are recorded and correspond to the number and size of the cells passing through. Unlike a microscope, which relies on visual observation, the Coulter counter allowed for precise, reproducible, and large-scale cell measurements. The first demonstrated Coulter counter was able to measure up to 6000 Events per second, surpassing the capabilities of human counting by magnitudes[7]. Due to improvements in technique modern Coulter counters can reach the recording of ten thousand events per second, as for example the Beckman Coulter

https://doi.org/10.7795/110.20260122

Multisizer 4e [8]. However, a Coulter counter is still a limited cytometer, as it can only measure cell size and concentration without distinguishing between different cell types of same size.

The first fluorescence-based flow cytometers, capable of differentiating cells based on their physical and biochemical properties, were developed in the late 1960s and early 1970s [9–11]. A flow cytometer works by suspending cells in a fluid stream and passing them one by one through a laser beam. As the laser interacts with each cell or particle, the scattered light and possibly fluorescence signals are detected, providing information about cell size, granularity, and surface markers. By using fluorescence labeled antibodies, specific cell types can be identified based on the presence of unique proteins on their surface. The scattered and fluorescence light is focused by a microscope objective onto a detector, converting the counted photons into electric signals. These are analyzed by a computer depending on predefined conditions and either saved or discarded. A trigger algorithm is typically employed to detect the presence of a particle in the laser beam, activating data recording and significantly reducing the amount of generated data. This technique allows for rapid and highly detailed analysis of blood, cells and particles, making it an essential tool in research, diagnostics, and even clinical applications such as immune profiling. Numerous advancements in flow cytometry have led to modern flow cytometers achieving reported speeds in the range of 100 000 events per second [12, 13], however common counting rates of commerial devices are in the range of several hundred to several thousand events per second [14, 15].

Such high event rates come with drawbacks. A measurement setup inherently has a dead time during which a new event cannot be recorded. If the time between two consecutive events is shorter than the dead time, the two events can no longer be distinguished and are registered as a single event. This phenomenon is called *coincidence*. As event rates increase, the likelihood of coincidences rises exponentially [16]. To mitigate this issue, one can either slow down the measurement process—resulting in increased measurement time—or apply a coincidence correction.

In this thesis, several approaches for the detection and correction of coincidences will be presented. These methods rely on recording the entire passage of particle or cell through the laser beam, generating a *pulse shape*. The pulse shapes are analyzed in a post-processing step using parameters such as standard deviation, skewness, and kurtosis to extract additional information. A requirement to this analysis is that the measurement setup is able to record a temporal intensity profile. This is not standard in todays commercial devices. Conventionally, the maximum scattering intensity in both the forward and sideward directions is measured and visualized in a 2D histogram [15, 17]. By introducing more parameters to characterize the pulse shape, data can be represented in 1D or 2D histograms as needed, enabling individualized and customized analysis.

By modeling the trigger algorithm, the effects of coincident pulses on these parameters can be simulated and identified in experiments. Using standard deviation and skewness, it is even possible to detect coincidences involving two different types of particles, cells or as done here, with erythrocytes and thrombocytes, in polydisperse suspensions. Once a coincident pulse is identified, its pulse shape can be extracted as single event, allowing for a refined and more detailed analysis.

https://doi.org/10.7795/110.20260122

The current state of the art for coincidence correction stipulates a dilution series, as outlined in the German Deutsche Industrie Norm (DIN) standard 58932 – 3 [18, 19, 16]. The International Council for Standardization in Haematology (ICSH) has also established guidelines for coincidence correction based on dilution series, as specified in ISO 15193 and ISO 17511 [20]. The drawback of this method is that at least four series of measurements are required, and a dilution factor spread of four must be achieved. The counting rates for different dilutions are then extrapolated to infinite dilution, yielding the statistically correct number of events.

Although the dilution series method is highly accurate, it can be tedious, as it requires measuring at least four different dilution steps. The alternative approach developed in this work relies on a single measurement and is based on the recorded waiting time between two consecutive events. The requirements for such a new approach remain the same: it should be reproducible, accurate, and allow for an uncertainty analysis. For measurements following Poisson's law, the probability density of the waiting time exhibits a negative exponential correlation [21]. It may seem counterintuitive, but the most probable waiting time for a consecutive event is zero.

There is a shortest recordable waiting time—referred to in this work as dead time—limited by the readout speed of the data recording, the trigger mechanism, and the pulse length. Due to the self-similarity of the exponential function, it is sufficient to determine the mean of all waiting times exceeding a certain cutoff threshold. From this, the true mean—and consequently the true number of events—can be derived.

As mentioned earlier, the very first cytometers, such as flow cytometers and Coulter counters, were a major improvement in cell and particle counting compared to manual microscopy. However, microscopy still had one significant advantage: the ability to capture images of the sample. Throughout the 20th century, all commercial devices were based solely on counting cells or particles, with additional information obtained through staining or gating intensity levels.

Amnis Corp.[1], which developed the first commercial imaging flow cytometer, aptly stated: "Seeing is Believing, but ImageStream® is Proof" [22]. In 2004, they introduced the *Amnis ImageStream®* [23]. By enabling the capture of cell images—similar to traditional microscopy—this technology provided a new level of spatial information. It became possible to visualize and analyze cells based on their cell cycle, morphology, and composition, as well as to virtually sort them in post-processing [24]. By 2015, just ten years later, there were already over 500 peer-reviewed articles on imaging flow cytometry, with rapid advancements driven by improvements in computer hardware [25].

Applications of this technology include distinguishing between live and dead cells (e.g., cell necrobiology) [24, 26], determining the distribution of stained regions such as the nucleus-to-cytoplasm ratio [27], sperm scoring [28], immunocytomorphological characterization of human bone marrow [29], and analyzing extracellular vesicles [30, 31].

To achieve high flow rates while maintaining motion-blur-free images, exposure times must be kept short. The latest generation of the Amnis ImageStream® addresses this challenge using Time Delay Integration (TDI) technology [32]. In this method, the speed of the cells

[1] now Cytek Biosciences

https://doi.org/10.7795/110.20260122

is measured using pre-mixed speed beads, and the CCD readout is synchronized with their movement speed, significantly improving the signal-to-noise ratio.

In the setup used in this work, even the shortest camera exposure time is too long to prevent motion blur. To counter this, the imaging laser illumination is triggered for an extremely short duration, ensuring the illumination time remains brief enough to avoid motion blur. As a result, the camera is exposed to light only for a fraction of its full exposure time.

With the advent of imaging flow cytometry, it also became possible to capture side-scattered light. In the working Group 8.31 at PTB, an intriguing phenomenon was observed when imaging spheres in the sideward direction. Instead of the expected spherical shape, two bright spots appeared. This raised the question of whether these spots were measurement artifacts or had a physical origin. Some publications on side-scattered imaging have reported similar spots, yet no explanation or discussion has been provided [30, 33].

This observation led to the investigations in Chapter 4.3.2 on *Glare Points*. The observed spots are, in fact, Glare Points, a well-known phenomenon in other fields such as spray analysis [34–36]. By developing a rigorous model for imaging in flow cytometry and comparing sideward images with experimental measurements, it becomes evident that the same effect is at play. However, to fully describe the phenomenon, the physical model must be extended for large numerical apertures and particle sizes in the Mie regime.

To date, the author has not found any simulations of aspherical particles or their potential effects on Glare Point formation in the literature. In this work, the effects of particle deformation—such as stretching or compression—on Glare Points will be investigated. When high-refractive-index particles are stretched, additional bright spots appear on the particle surface in the sideward image. It remains to be determined whether these spots are caused by Mie resonances or surface waves.

Technically, particle stretching can be achieved by increasing the flow rate and narrowing the flow cell, thereby applying shear forces to the sample. Depending on the stiffness of the particles and the applied force, they deform into an spheroidal or bullet-like shapes [37]. Commercial devices already exist for measuring rheological properties using this principle, such as those developed by Zellmechanik Dresden [38]. This new technique has paved the way for the emerging field of deformation cytometry [39–41].

Imaging flow cytometry is both expensive and data-intensive compared to traditional counting flow cytometers. To achieve some level of spatial resolution, some form of spatial detector is necessary. Kage et al. approached this by using several spatially distributed fibers in the forward direction (multi-angle pulse shape detection), where the pulse shape was recorded by a photomultiplier tube (PMT) [42, 43]. By comparing signals from different fibers and decomposing the pulse into Fourier coefficients, they successfully sorted Jurkat and HEK293 cells according to their cell cycle stage.

In this work, the theoretical suitability of a quadrant photodetector, as an alternative to the currently used PMT, is examined with regard to its ability to extract information about the shape of particles.

These detectors are relatively inexpensive, commercially available, and widely used for beam positioning in various fields [44–46]. Esper-Chaín et al. even state that quadrant photodetectors

https://doi.org/10.7795/110.20260122

are the best devices for measuring laser beam positions, making them potentially suitable for detecting slight far-field deformations [46].

A perfectly spherical particle produces a spherical far-field pattern, whereas a deformed particle, such as a stretched one, generates an elliptical far-field distribution. By determining the intensity ratio between two opposing quadrants (i.e., a measure of asphericity), it may be possible to infer the aspect ratio of the particle. Assuming a sensitivity of 4% in intensity difference, spherical and aspherical particles can theoretically be distinguished even for sizes smaller than the wavelength.

For some applications, it is sufficient to determine whether a sample contains spherical or aspherical particles. In such cases, a quadrant detector provides a cost-effective and straightforward alternative.

In the first chapter, the used measurement setup will be explained shortly with focus on the trigger mechanism. It is followed by some theoretical background regarding Lorenz-Mie theory and discrete-dipole approximation. The third chapter presents the optimization algorithm for characterizing the optical parameters in the flow cytometer. In the fourth chapter a comparison between measured and simulated images will be shown and afterwards additional investigations on simulated spheroidal particles is done. The fifth chapter deals with the evaluation of pulse shapes. It is structured first in the postprocessing of pulse data, second in the detection of coincidences using the pulses standard deviation and skewness and third the correction of coincidences with a new method based on the waiting time between consecutive pulses. The sixth chapter presents the theoretical model of a quadrant detector and how this can be used to gain information about the shapes of investigated particles. The thesis closes with a summary in the seventh chapter.

https://doi.org/10.7795/110.20260122

https://doi.org/10.7795/110.20260122

2

Measurement Setup and Theoretical Background

2.1 Flow Cytometer Setup

The flow cytometer used in this work combines imaging with detection of conventional scattering and fluorescence intensity. Generally speaking, the larger a particle or cell and the higher the index contrast the stronger the scattering signal. If the flow cytometer is calibrated with test particles, a direct correlation between sample size and scattering intensity can be made for the used sizes. Otherwise, only the counted number of (sub)populations can be acquired from either a 1D or 2D histogram, which is often sufficient. Typically, the forward scattered (FSC) intensity is depicted against the side scattered intensity (SSC). The setup consists of a flow cell, guiding the flow of samples through the imaging and trigger laser beam, which are employed for detection and imaging of the samples. The scattered and fluorescence light is detected and imaged in forward and sideward direction by cameras and photo-multiplier tubes (PMT).

In Figure 2.1 the detailed measurement setup of the used flow cytometer is depicted. The laser with a wavelength of 406 nm is used for imaging particles on the cameras. The trigger laser has a wavelength of 488 nm and its signal is used by the trigger generator for triggering the imaging laser. Its interaction with the particles is located upstream with respect to the imaging laser taking into account the flow direction. The trigger lasers signal is detected by the FSC PMT (H10720-01, Hamamatsu Photonics Deutschland GmbH). If the trigger level is reached, the trigger generator triggers the imaging laser with a certain delay (the time is adjusted such that it is equivalent to the time the particles need to flow from the trigger lasers to the imaging lasers spot.). The details and consequences of the trigger setup will be explained in Section 2.2. In the flowcell the particles[1] are flowing perpendicular to the forward and sideward direction (i.e. perpendicular to the figures plane) . Here hydrodynamic focusing

[1] or cells. For simplification in this thesis the word particles will be used, but it always includes cells if not stated otherwise.

https://doi.org/10.7795/110.20260122

[47, 48] is used[2]. Hydrodynamic focusing makes use of a sheath flow to confine a central flow, driven by a syringe, containing the particles. The sample then moves downward in single file, where they are illuminated by the trigger and imaging laser in the flow cell.

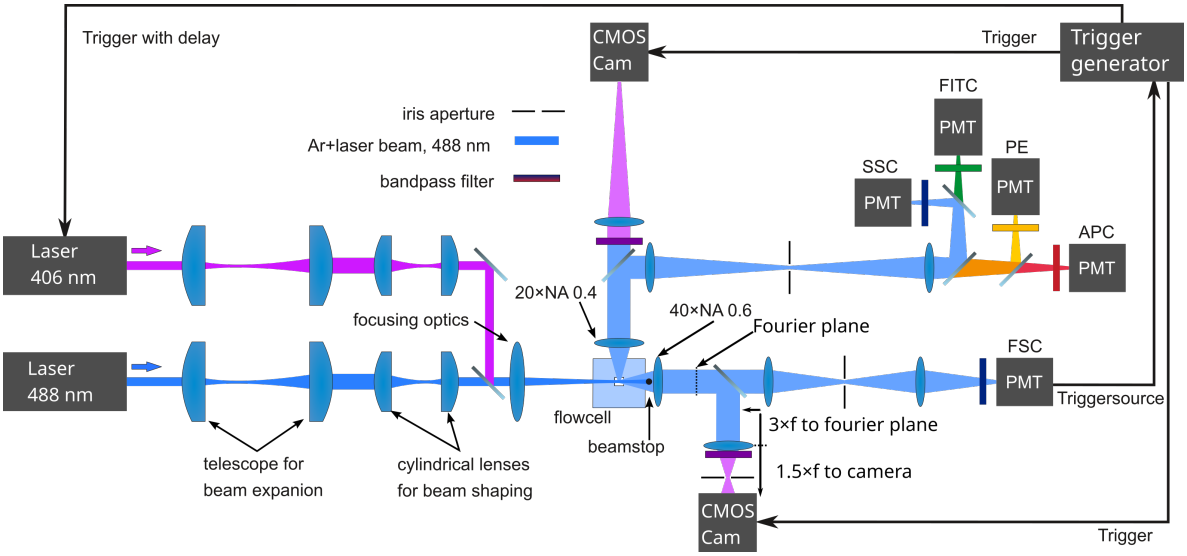

Figure 2.1: Setup of the flow cytometer used in this work. General description: particles or cells are flowing perpendicular to the figures plane through the flow channel of the flowcell. The lasers beam passes through the flow channel and its light is scattered by the particles or cells in all spatial directions. The scattered light is collected in forward and sidward direction by microscope objectives and directed to the camera and/or photomultiplier tubes. Their signal is then processed and analyzed in this work. Figure provided by Martin Hussels.

The imaging laser beam first propagates through beam expansion and shaping lenses, after which it is focused on the flow channel of the flow cell. Here the laser light is scattered in all spatial directions by the particles. The scattering process in this work will be described either by Lorenz-Mie theory or discrete dipole approximation and is described in the Sections 2.4 and 2.5. The scattered light is collimated in forward and sideward direction (90° to forward) by a microscope objective with a numerical aperture (NA) of 0.6 (UCPLFLN40X/0.6, long working distance, Olympus Deutschland GmbH) and 0.4 (PLAN H20×/0.40 ∞ /1.8 Q, Leitz Wetzlar, Germany)) respectively. The intense direct laser beam is blocked by a beamstop in forward direction, which is attached to the collimating lens. The divergent, scattered light passes around the beam stop. Otherwise the camera and PMT would be over-saturated by the laser light and become insensitive to the much lower intensity of the scattered light or might even take damage at high laser powers. A beamsplitter, another imaging lens, bandpass filter and a CMOS (Complementary Metal-Oxide Semiconductor) camera are following in beam propagation direction. CMOS cameras are fast for real world photography, however even the shortest exposure time of 30 µs is too long for a motion blur free image. In fact, a total transit through the laser usually takes about 3 µs to 15 µs. If the imaging laser is triggered, a short laser pulse of 0.1 µs to 1.0 µs is emitted leading to a motion blur free image.

In previous experiments it was found that when positioning the collimating and imaging lens in a distance multiple of the fourier plane of the collimating lens, the image became a lot more stable. If this condition holds true, only changes in the scattering angle of the particle will lead to position changes on the camera. If this condition is not fullfilled, even the

[2] there is also e.g. acoustic focusing with ultrasonic sound waves [49–51].

https://doi.org/10.7795/110.20260122

particles minor movements during laser exposure time led to less sharp and instable images. A bandpass filter is added in front of the camera to suppress the trigger lasers light. Also, an iris aperture is added for a sharper image, which is a common procedure. Towards the PMT also an iris aperture is added and a bandpass filter, to suppress the imaging lasers light and straylight. The light is focused on the PMT in forward direction by the last imaging lens. The PMT collects the temporal scattering signal. This is saved as a pulse-shape in forward direction which is a fundamental component of this work and will be extensively analyzed in Chapter 5.3.4.

In sideward direction, multiples of the Fourier plane could not be realized due to spatial conflicts with other optical elements. After the collimating lens in the sideward direction, the beam passes through a beam splitter, followed by a bandpass filter to isolate the trigger laser light, and then the collimated light is focused onto a camera. With this camera, Glare Points (see chapter Glare Points), for example, can be imaged.

Continuing from the beam splitter, the reflected light is shaped by an iris aperture, split into several channels, and eventually directed to the PMTs of the channels. The SSC PMT (H10720-01, Hamamatsu Photonics Deutschland GmbH) collects the SSC signal analogously to the FSC PMT. In sideward direction, it is possible to measure several fluorescence channels, such as fluorescein isothiocyanate (FITC), phycoerythrin (PE), and allophycocyanin (APC). However, these channels are irrelevant for this work, as no fluorescence measurements are used here.

2.2 Triggered Data Acquisition

To record signals only when indeed a sample passes the trigger beam, a trigger mechanism is needed. This is realized by an additional laser beam with a wavelength of 488 nm, which is passed by the sample before it reaches the imaging beam. A trigger is necessary to significantly reduce the amount of recorded data. Comparing a typical measurement duration of approximately 20 µs with the average waiting time between two pulses of around 500 µs (see, for example, Figure 5.26), it becomes evident that less than 10% of the total measurement time is recorded. The Field Programmable Gate Array (FPGA) (PXIe-7962R, National Instruments Corp.) generates approximately 2 GB of raw data per second during a typical measurement lasting 120 s. By utilizing the trigger mechanism and saving the data in *.tdms* files [3] [52], the total data size of a 120 s measurement is reduced to between 50 MB and 200 MB. The FPGA records the data with 20 MHz sampling rate. The typical measurement duration of 20 µs then yields around 400 datapoints per pulse.

The intensity of the trigger laser is continuously monitored via the FSC and SSC PMTs. Figure 2.2 shows the qualitative intensity signal plotted over time. The recorded pretrigger (depicted in purple in Figure 2.2) and recorded posttrigger (depicted in green) sections are highlighted accordingly. The trigger level is represented as a dotted line. The general principle is as follows: if the signal exceeds the trigger level, data recording begins. Once the signal falls

[3] The TDMS (Technical Data Management Streaming) file format is a structured binary format developed by National Instruments (NI). It is optimized for high-performance streaming, logging, and retrieval of measurement data, making it widely used in scientific, industrial, and engineering applications.

https://doi.org/10.7795/110.20260122

below the trigger level again, data recording ends. The entire triggering process and pulse shape recording are managed by a FPGA.

At the start of each measurement, the pretrigger is filled with data points, following a moving first-in-first-out (FIFO) principle. This ensures that only the most recent elements are retained. When the trigger level is surpassed, the content of the pretrigger is saved, and data recording begins. The trigger activates only if a certain number of pretrigger elements lie below the trigger level. Once the signal drops below the trigger level, the posttrigger is filled and appended to the recorded data. After the posttrigger phase is completed, the pulse is saved, and the pretrigger begins filling again. During the posttrigger and pretrigger filling phase, the trigger mechanism is deactivated, meaning that additional signal surpasses during this time will not be detected.

Pulse 1 in Figure 2.2 represents a typical pulse, which is fully recorded. Such pulses account usually for more than 90% of the data. The pretrigger and posttrigger sections are shown in purple and green, respectively. However, if the temporal distance between two pulses is too short and the trigger level is not undershot between them, the recording continues, resulting in a coincidence, as illustrated by the second example in the figure. In this case, both pulses are recorded and saved as one, leading to an underestimation of the actual number of counted events.

In the third example, the signal falls below the trigger level after pulse 4, but a second, pulse 5, arrives during the posttrigger phase. Since no checks for surpassing or undershooting the trigger level are made during the posttrigger phase, pulse 5 is partially recorded and not included in a subsequent measurement, resulting in data loss.

If the distance between pulse 4 and 5 is increased such, that pulse 5 exceeds the trigger level during the pretrigger phase (which follows after the posttrigger phase is finished), pulse 5 is not even partially recorded and therefore lost since the trigger is not active yet. Pulses can only be recorded if the pretrigger is fully armed. This is the only configuration in which pulses can in fact be lost. This is a disadvantage of the used trigger mechanism, although this case is very rare. Between pulse 5 and a potential pulse 6 (not seen in Figure), the intensity needs to fall below the trigger level and sufficient time must pass to then fill the pretrigger.

If the potential pulse 6 is such far apart that the pretrigger is filled completely, parts of the descending slope of the (not recorded) pulse 5 may be included in the pretrigger for the recording of pulse 6. For this case to occur there is only a narrow range of pulse distances possible. In all other cases, the first arriving pulse will always be recorded completely and the second arriving pulse either completely as well or partially. This results in more coincidences where a secondary pulse is recorded on the right-hand side of the main pulse compared to the left-hand side, even though this should be statistically equivalent.

The time in which no further pulse can be detected is called dead time. The dead time with this particular trigger setup is the sum of the data recording time, the posttrigger time and the pretrigger time of the consecutive pulse. In the third example the dead time is even further extended, since the intensity of the pulse 5 has to drop below the trigger threshold and the pretrigger needs to be filled again. The pretrigger will not start to fill before the intensity is below the trigger level. Therefore the dead time is dynamic and not constant as with many other setups. The benefit of a dynamic pulse length is that the routine does not

https://doi.org/10.7795/110.20260122

need to be adapted for different flow speeds. Potential correction and detection algorithms for coincidences during the dead time are discussed extensively in Chapter 5.3.4.

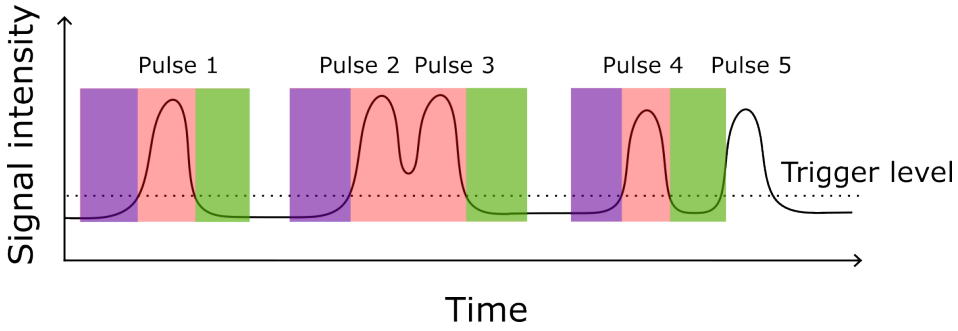

Figure 2.2: Schematic explanation of the trigger mechanism. If the trigger level is uppercut, the data recording starts and if the trigger level is undercut the data recording ends. The pre- and posttrigger data points will be added to the beginning and end of a measurement and are depicted with purple and green boxes, respectively. The measurement window for each pulse is visualized as red boxes. If the temporal distance between two pulses is too short, a coincidence occurs as in the second measurement. In the third measurement, the trigger level is undercut after the first pulse, which means the second pulse is only partially recorded.

2.3 Definitions and Coordinate Systems

Throughout this thesis, several quantities are used that might require clarification regarding their usage. In this thesis, a plane electromagnetic wave propagating in the forward z-direction is defined as follows:

$$\boldsymbol{E}(z,t) = \boldsymbol{E}_0 e^{ikz - i\omega t} \tag{2.1}$$

E_0 represents the electric field amplitude of the wave. The wavenumber k is a scalar, defined as the wavenumber in a medium with refractive index n_{medium}, with $k = n_{\text{medium}} \cdot k_0$, where k_0 is the wavenumber in vacuum. Similar to the wavenumber, the wavelength is denoted as $\lambda = \frac{\lambda_0}{n_{\text{medium}}}$. In flow cytometry, the refractive index of the medium is typically that of water, with $n_{\text{medium}} = 1.3431$ [53]. Additionally, the relative refractive index $m = \frac{n_{\text{particle}}}{n_{\text{medium}}}$ can be defined. When discussing opening angles and the angular size of the beamstop, the term always refers to the half-angle, as defined in the numerical aperture (NA) $NA = n \sin(\theta)$.

In Bohren & Huffmans book "Absorption and Scattering of Light by Small Particles" [1], the coordinate system on which the theory in this work is based, is very well described. Therefore their graphic is used here, as shown in Figure 2.3. A laser beam propagating along the z direction is considered. The origin, with $x = y = z = 0$, lies on the laser beam and is also the origin of the spherical coordinate system (θ, ϕ), which describes the far field of the scattered electromagnetic field. The orientation of all coordinates can be expressed in dependence of the polarization components of the incident laser and its propagation direction z. The vector $\hat{e}_r$ describes the observation direction. For $\phi = 0$ and $\theta = 90°$, the ϕ vector is anti-parallel to the perpendicular component of the incident beam $E_{\perp\text{inc}}$ and parallel to the y-axis. The θ vector then is parallel to the parallel component of the incident beam $E_{\parallel\text{inc}}$ and parallel to the x-axis.

The parallel component of the scattered field $E_{\parallel\text{sca}}$ is parallel to the θ vector and the perpendicular component is antiparallel to the ϕ vector. The are always orthogonal to the observation direction $\hat{e}_r$.

https://doi.org/10.7795/110.20260122

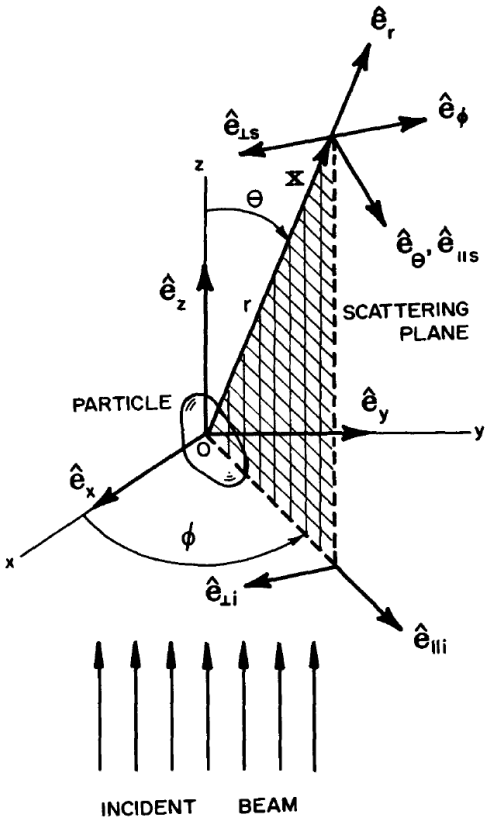

Figure 2.3: Coordinate system used in this book. Graphic taken from the book: Bohren & Huffman "Absorption and Scattering of Light by Small Particles" [1].

If a moving particle is considered, the position is expressed in the cartesian coordinates (x, y, z). The particle can be rotated using Euler angles (α, β, γ). In the lab, the flow direction is parallel to the laser's parallel polarization direction. In the model the particle then moves along the x-axis. A potential detector in the sideward direction would then have the central coordinates $\phi = 90°$ and $\theta = 90°$

The elements of the scattering matrix S in observation direction $\hat{e}_r$ are defined as functions of the spherical coordinates $S(\theta, \phi)$ (see Section 2.4).

2.4 Lorenz-Mie Theory

More than 100 years ago, in 1908, Gustav Mie published a numerically exact solution to the problem of light scattering by spherical particles [54]. However, Ludvig Lorenz had already published his solution to the same problem in 1890 [55]. It is assumed that Gustav Mie published his work without knowledge of Ludvig Lorenz's work. Occasionally, Peter Debye is also mentioned for his contributions [56]. In this thesis, the term Lorenz-Mie theory/scattering (LMT) will be used. Since then, the theory has been applied and described numerous times. Therefore, the concept will only be described qualitatively here. For a more detailed mathematical description, see the following sources: [57, 1, 58–61].

Light scattering by a homogeneous sphere can be described using the scalar Helmholtz equation for the electric field. The Helmholtz equation is written in spherical coordinates and solved by separation of variables. The solutions are scalar spherical wave functions. It can be

https://doi.org/10.7795/110.20260122

shown that if the scalar spherical wave functions are solutions to the Helmholtz equation, then the vector spherical wave functions derived from these scalar solutions are also solutions. The incident plane wave, the scattered, and the internal electric field can all be expressed as infinite sums of the aforementioned spherical wave functions. The spherical wave functions depend on coefficients a, b, c, d (here only qualitatively defined). These coefficients are dependent on the relative refractive index m, the size parameter x, the spherical Bessel function of first and second kind and the spherical Hankel function of first and second kind. The coefficients a, b are needed for the scattered field and the coefficients c, d for the internal field. These solutions can be understood as an expansion into multipoles (i.e., partial waves), with the first being a dipole, the second a quadrupole, and so on. The coefficients a, b, c, d depend on the relative refractive index m and the size parameter $x = \frac{\pi d}{\lambda}$, where d is the particle diameter. They are also needed to calculate the scattering matrix.

The scattering matrix $\mathsf{S}(\theta, \phi)$ describes how an arbitrarily shaped scatterer scatters an incident, polarized electric field $\boldsymbol{E}_{\text{inc}}$, as shown in Equation 2.2.

$$\boldsymbol{E}_{\text{sca}} = \frac{\exp(ik_{\text{sca}}r)}{-ik_{\text{sca}}r} \cdot \mathsf{S} \cdot \boldsymbol{E}_{\text{inc}} \rightarrow \begin{pmatrix} E_{\parallel \text{sca}} \\ E_{\perp \text{sca}} \end{pmatrix} = \frac{\exp(ik_{\text{sca}}r)}{-ik_{\text{sca}}r} \begin{pmatrix} S_2 & S_3 \\ S_4 & S_1 \end{pmatrix} \begin{pmatrix} E_{\parallel \text{inc}} \\ E_{\perp \text{inc}} \end{pmatrix} \tag{2.2}$$

Equation 2.2 provides the complex far-field amplitude of the scattered, polarized electric field $\boldsymbol{E}_{\text{sca}}$. This is valid for r much larger than the wavelength $\lambda_{\text{sca}} = \frac{2\pi}{k_{\text{sca}}} \Leftrightarrow k_{\text{sca}} = \frac{2\pi}{\lambda_{\text{sca}}}$. The elements S_1 to S_4 are dependent on the scatterers optical and geometrical properties.

For spherical particles, the matrix elements S_3 and S_4 are zero. This also means, that a completely parallel or perpendicular polarized incident wave will not change its state of polarization. Due to the usage of lasers in the experiments, only completely parallel polarized incident waves $\boldsymbol{E}_{\text{inc}} = \begin{pmatrix} a \\ 0 \end{pmatrix}$, with a the electric fields amplitude, were used. Using the coefficients a and b, the nonzero (complex) scattering components $S_1(\theta)$ and $S_2(\theta)$ of the scattering matrix S can be calculated.

$$S_1(\theta) = \sum_{\nu=1}^{\infty} \frac{2\nu+1}{\nu(\nu+1)} \left(a_\nu(m,x) \frac{P_\nu^1(\cos\theta)}{\sin\theta} + b_\nu(m,x) \frac{dP_\nu^1(\cos\theta)}{d\theta} \right) \tag{2.3a}$$

$$S_2(\theta) = \sum_{\nu=1}^{\infty} \frac{2\nu+1}{\nu(\nu+1)} \left(a_\nu(m,x) \frac{dP_\nu^1(\cos\theta)}{d\theta} + b_\nu(m,x) \frac{P_\nu^1(\cos\theta)}{\sin\theta} \right) \tag{2.3b}$$

In Equation 2.3 P_ν^1 are the associated Legendre polynomials of first order. $\boldsymbol{E}_{\text{inc}}$ denotes the incident electric field (in case of a parallel linear polarized laser as used in this work $\boldsymbol{E}_{\text{inc}} = \begin{pmatrix} A \\ 0 \end{pmatrix}$ with A the amplitude). The dependency in ϕ can be introduced by simply rotating the laser polarization. Additionally to the scattering matrix and near-field, the scattering C_{sca} and extinction cross section C_{ext} can be obtained.

https://doi.org/10.7795/110.20260122

$$C_{\text{sca}} = \frac{2\pi}{k^2} \sum_{n=1}^{\infty} (2n+1) \left(|a_n|^2 + |b_n|^2 \right) \tag{2.4a}$$

$$C_{\text{ext}} = \frac{2\pi}{k^2} \sum_{n=1}^{\infty} (2n+1) \Re(a_n + b_n) \tag{2.4b}$$

The infinite sum of spherical wave functions or the sum depicted in Equation 2.3 or 2.4 can be implemented numerically, however a reasonable truncation value has to be found. Small particles behave like dipoles and need only few iterations. Contrary, for large particles thousands of iterations can be necessary. In the times where Gustav Mie developed his theory, no computer was available to calculate the sum of infinite wave functions. It is told that he usually calculated the first three waves and was the opinion that from a practical point of view his solution was only useful for particles much smaller than the wavelength. This of course changed with the invention of the computer.

In the 1980s the development of the General Lorenz-Mie theory (GLMT) began. The GLMT is able to consider any incident beam that obeys Maxwell laws. There was a need for other formulations due to the invention of the laser, which opened the field to tightly focused beams in the size of the scattering particle [62, 63]. The main contributors were Lock, Grehan and Gouesbet. The general idea is to introduce beam shape coefficients to the infinite series of spherical wave functions[64]. A major problem that arises for a Gaussian beam is that the Gaussian beam does not solve the Maxwell equations. For this, e.g. Barton developed an expression which approximates a Gaussian beam very well but still solves the Maxwell equations [65].

In this work the Lorenz-Mie implementation by Scott Prahl [66] was used and additional beam shape coefficients added for the on-axis case were introduced by Jonas Gienger.

2.5 Discrete-Dipole Approximation

The discrete-dipole approximation (DDA) is younger than the Lorenz-Mie theory. The foundation was laid by DeVoe in 1964 [67, 68], who used it to investigate the optical properties of molecular aggregates. However, he did not account for retardation effects, which become important for larger structures, such as aggregates. In 1973, Purcell and Pennypacker extended the DDA to study interstellar dust grains, including retardation effects [69]. The DDA is capable of simulating the scattered light by particles with arbitrary shapes. As the name suggests, the scatterer is described by an ensemble of dipoles with sufficient resolution. The scattered electric field of the scatterer is then the sum of the fields scattered by the individual dipoles. Since the dipoles are coupled via their electric fields, the method is sometimes also referred to as the coupled-dipole approximation [70, 71]. The DDA is a finite-volume method. In contrast to the Lorenz-Mie theory, which is based on the separation of variables for the Helmholtz equation, the DDA relies on the evaluation of the Green's function for the corresponding differential operator. There are numerous sources in the literature that explain the mathematics and methodology behind the DDA [72–77, 61]. Kahnert provides a good comparison of different methods for describing electromagnetic scattering in [78]. In

https://doi.org/10.7795/110.20260122

general, the DDA is a rigorous numerically exact solution. However, in practice, it is limited by the number of dipoles the computer can handle. The solution to the scattered field is a $3N_{\text{dipoles}} \times 3N_{\text{dipoles}}$ linear system of equations, where N_{dipoles} is the number of dipoles. If a general solver, such as the Gaussian method, is used, this results in a scaling of $\mathcal{O}(N_{\text{dipoles}}^2)$, which becomes inefficient as N increases cubically with the volume.

For this work, the DDA implementation by Yurkin et al., called ADDA (Amsterdam Discrete Dipole Approximation), is used [77]. The ADDA implementation is written in C and can use MPI (message passing interface) to run the code on multiple cores. It is also capable of running on graphic processing units [79], enabling the calculation of large numbers of dipoles in a reasonable amount of time. For this work, only the Message Passing Interace (MPI) version was used. Any incident electromagnetic field can be chosen as an input file. For all calculations, the formulation by Barton in the fifth order was chosen [65]. The code is inefficient for near-field calculations; however, in this work, only the far-field is of interest. To solve the $3N_{\text{dipoles}} \times 3N_{\text{dipoles}}$ linear system of equations, ADDA uses a Fast Fourier Transform (FFT) implementation. This reduces the scaling from $\mathcal{O}(N_{\text{dipoles}}^2)$ to $\mathcal{O}(N_{\text{dipoles}} \cdot \log N_{\text{dipoles}})$ [73]. Nevertheless, even with this optimization, a particle of 15 µm diameter, with $m \approx 1.2$ and a wavelength of 305 nm in water, can take several days to compute on a server with 128 cores, as experienced by the author. A list of the largest simulations can be found on the ADDA GitHub page [80]. Yurkin et al. state in their manual that they experience an efficiency of around $70 - 90\%$ in multiprocessing. The server used has two AMD EPYC 7702 64-core processors.

For an arbitrary scatterer, the scattering matrix elements S_{1-4} in Equation 2.2 are all nonzero and depend on ϕ and θ. This means that for every combination of ϕ and θ in the defined grid, a different scattering matrix element is obtained in ADDA.

https://doi.org/10.7795/110.20260122

https://doi.org/10.7795/110.20260122

3

Characterizing a Cytometer

Cytometers are widely used for investigating stained cells or particles utilizing either their emitted fluorescent or scattered light. When it comes to separating populations one from another, only the relative signal intensity to other populations is relevant.

In this scenario, it is assumed that the user already knows the relationship between the desired population and other populations. According to Wang [81], "it is not advisable to use scatter for quantitative cell sizing" because "the scattering of particles has strong nonlinear dependence on the angles measured and the refractive index of the particle, as well as particle size, internal structure, and content."

While flow cytometers can be calibrated using beads (standardized test particles) [82], without detailed knowledge of the optical components this approach is limited to the calibrated sizes [83, 84]. In this case, interpolation to other sizes is prone to significant errors due to the mentioned strong nonlinear nature of the scattering signal.

Ost et. al. developed a method to calibrate their flow cytometer regarding differential cross sections using polystyrene beads and were able to determine the differential scattering cross section of sphered erythrocytes [85]. Well characterized polystyrene beads were measured and compared with theoretically expected values from Lorentz-Mie scattering. The experimental results were normalized to the theoretical differential scattering cross section of polystyrene spheres with a diameter of 7 µm for comparison. The optical properties were "[...] obtained by means of ray tracing, considering the flow channel (water) and the quartz glass of the flow cell as well as the optics of the microscope objectives."

Van de Pol et. al. developed a very similar calibration method for sizing extracellular vesicles and (sub-) microparticles [86]. Instead of a normalization they introduced a conversion factor and used diameters and scattering cross sections instead of differential scattering cross sections [87, 88]. This method led to the calibration software *Rosetta* by Exometry [1].

Both methods have in common that the optical properties of the flow cytometer were precisely characterized beforehands. Either by them self via ray tracing or by the manufacturer. As a manufacturer, it is not easy to determine the exact opening angles of a flow cytometer,

[1] `https://www.exometry.com/`

https://doi.org/10.7795/110.20260122

even though the nominal numerical aperture of the used objectives is known as stated by the objectives manufacturer. Usually there are additional optical elements in the scattered lights propagation path: the lasers light is scattered at particles in water, propagates through the glass wall of the cuvette, then propagates through air until it is collected by the objective. Then it usually is collimated and imaged on a photomultiplier tube with a possible iris aperture. Due to all the additional optical elements the numerical aperture of the objective must not match the true opening angle. Although it is possible to measure all distances in glass, water and air to determine the true opening angle in principle, this is very cumbersome and prone to errors in practice.

Since a flow cytometers detector (excluding camera) is only able to measure the intensity of the scattered light, it would be very advantageous to characterize the flow cytometer on the basis of the scattered intensity without needing special equipment, not to mention having to disassemble it. By knowing the optical parameters, interpolation between particle sizes can be significantly improved using Lorenz-Mie theory and enables the usage of e.g. the above mentioned methods. In this work an algorithm is presented to ascertain the opening angle and beamstop angle in forward direction and the opening angle in sideward direction of a flow cytometer.

The experimental data was acquired by the company LUM GmbH [2] on one of their flow cytometers. The functionality of this flow cytometer does not differ from the experimental setup described in Chapter 2.5.

3.1 Optimization Algorithm

The idea behind the algorithm is to measure the scattering intensity of spheres with different diameter and then compare the measured intensities with the simulated intensity of these spheres. The problem is formulated as an ill-posed inverse optimization problem with variable opening angle, beamstop angle, sphere diameters and an additional offset angle in sideward direction. The number of particles and their size difference must be large enough such that the measured intensities then form a unique set with which an optimizer can find the correct opening angles. Too few diameters can lead to ambiguous parameter combinations.

The light scattering is modeled with the Lorentz-Mie theory (see Section 2.4) for every particle diameter d. In forward direction the intensity is integrated within the opening angle θ_{FW} excluding the beamstop angle θ_{BS}. In sideward direction the scattered field is also integrated within the opening angle θ_{SW}. To relate the measurement to the simulation, a linear detector function is defined in Equation 3.1 with the free parameters a, b. The detector function relates the measured intensity to the simulated intensity.

$$I_{\mathrm{sim}}(I_{\mathrm{meas}}) = a \cdot I_{\mathrm{meas}} + b \tag{3.1}$$

Residuum Definition

For an optimization algorithm, a residuum needs to be formed. The simplest residuum would be the least squares $Res = \sum_{n=0}^{N}((I_{\mathrm{sim,n}} - I_{\mathrm{meas,n}})^2 + (d_{\mathrm{sim,n}} - d_{\mathrm{meas,n}})^2)$ with N the

[2] `https://www.lum-gmbh.com/`

https://doi.org/10.7795/110.20260122

number of particle diameters. This formulation has the following problem: the intensity is strongly dependent on the diameter of the particle, which is why the residuum would be totally dominated by the largest particles residuum. Therefore other formulations were designed and introduced in this work, which consider the different particle sizes, shown in Equation 3.2a to 3.2c

$$\mathrm{Res}_1 = \sum_{n=0}^{N} \left(x^2 + y^2\right) \tag{3.2a}$$

$$\mathrm{Res}_2 = \sum_{n=0}^{N} \left((1+|x|)^2 + (1+|y|)^2\right) \tag{3.2b}$$

$$\mathrm{Res}_3 = \sum_{n=0}^{N} \left((1+|x|)^2 + (1+|y|)^2 - 2\right) \tag{3.2c}$$

with $x = 1 - \frac{I_{\mathrm{sim,n}}}{I_{\mathrm{meas,n}}}$ and $y = 1 - \frac{d_{\mathrm{sim,n}}}{d_{\mathrm{meas,n}}}$. These are based on the relative intensity and diameter change. The different formulations vary in properties which shall shortly be explained: On the one hand in Res_1 the gradient is smaller than in Res_2 [3], especially around zero, and the residuum can get very small for small values of x and y, which might lead to errors due to machine precision or rounding errors. On the other hand, the relative change around zero is greater than around one [4]. The residuum formulation Res_2 will reach $2N$ as an optimal result. In case this is a problem for the solver to not reach zero as an optimal result, in formulation Res_3 a subtraction of two makes sure the residuum will reach zero if the exact solution is found. All three formulations will be tested for their suitability in Section 3.2.

As an optimizer the *differential evolution* algorithm [89–91] was chosen, implemented in pythons scipy package (version 1.11.4). The benefit of this statistic optimization algorithm over the conventional gradient based algorithms is that it is highly suitable for nonlinear and high-dimensional problems. Although it is slower and usually needs more function evaluations, it is capable of finding solutions where gradient based algorithms would fail. Further, it is easy to use multiple cores, increasing speed significantly on servers compared to a desktop computer. Especially in sideward direction the intensity fluctuates greatly in dependency of the opening angle, making it a very good algorithm for the problem dealt with.

3.2 Results in Forward and Sideward Direction

For testing the algorithm, a mix of 5 polystyrene spheres was used with diameters shown in Table 3.1. They were manufactured by Dr. Lerche KG[5]. A 2D SSC intensity vs FSC intensity density histogram of that mix is visible in Figure 3.1. In the third column of Table 3.1 the boundaries for the particles sizes are shown. The boundaries of the particles for the solver are chosen wider than the measurement uncertainty. An optimizer usually finds better results if it is allowed to sample a wider interval unless there are any discontinuities (not the case here).

One could argue that the formulation of the residuum in Equation 3.2a to 3.2c does not consider measurement uncertainty. The optimizer could favor a value closer to the mean

[3] i.e. $\frac{d}{dx}x^2 < \frac{d}{dx}(1+x)^2 \quad \text{for} \quad x \geq 0$

[4] i.e. $\frac{d}{dx}\ln(x^2) > \frac{d}{dx}\ln(1+x)^2 \quad \text{for} \quad x > 0$

[5] `https://www.lerche-biotec.com/`

https://doi.org/10.7795/110.20260122

diameter to minimize the residuum, although the true value lies at the edge of the measurement uncertainty. A small change in diameter has a strong influence on the scattered intensity and therefore also on the intensity part of the residuum. Nevertheless, leaving out the diameter part of the residuum calculation led to the optimizer exceeding the maximum amount of iterations with all three residuum formulation. This was the case for forward and sideward direction, as well as the extended formulations (see next subsection for explanation).

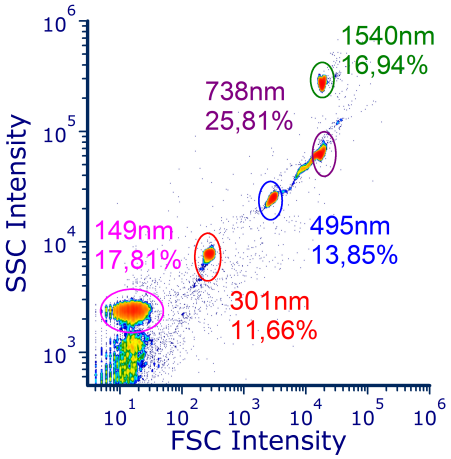

Figure 3.1: 2D density histogram showing the population of the five available polystyrene spheres.

Table 3.1: mean diameters of available polystyrene spheres. Uncertainties are given by the manufacturer Dr Lerche KG as standard deviations.

mean diameter d in nm	uncertainty in nm	solver boundaries in nm
149	7	$[140, 160]$
301	5	$[280, 314]$
494	23	$[460, 520]$
738	14	$[700, 755]$
1540	30	$[1450, 1570]$

Forward Direction

In forward direction the boundaries for the beamstop angle are $\theta_{\mathrm{BS}} = [1°, 5°]$, for the opening angle $\theta_{\mathrm{FW}} = [8°, 17°]$ and for the detector function $a = [3, 1000]$, $b = [1, 5000]$. To get an idea of the value of the detector function, first a run with the boundaries for a, b spanning over many magnitudes were done. Then the boundaries were lowered around the found value to the current value. Unfortunately, the signal in FSC for 149 nm was too low, which is why this size has to be excluded, leaving the algorithm with four sizes remaining.

In Table 3.2 the algorithms results are shown for all three residuum formulations. The calculations were done six times and the uncertainty denotes the standard deviation of the six runs. A full run takes even on the used server with 128 cores several minutes, which is why only six runs were chosen, still giving a good overview of the statistical fluctuations. It is visible that only with formuation Res_2 and Res_3 a result was achieved, formulation Res_1 did not terminate. The reason for this could be that four diameters are not enough to form a unique set of points to identify the flow cytometers parameter, which means additional

https://doi.org/10.7795/110.20260122

particles need to be introduced. Unfortunately there were no further particle sizes available, which is why an improvised solution was found. In Figure 3.1 it can be seen that between 495 nm and 738 nm there is a continuous connection of events due to particles being in size somewhere in between the two sizes. A point in the middle of that line was picked and declared as a new particle, extending the set of available particles with 611.5 nm. The boundaries of the particle are chosen with the diameter of the smaller and bigger neighboring particle. This is designated as the extended formulation in Table 3.2.

Among the extended formulations, Res_1 performed the best with stable results and a very small residuum. In contrast, the uncertainties of Res_2 and Res_3 are quite high compared to Res_1 and far above acceptable values. An uncertainty of about 0.2° is desired. LUM GmbH assumes that the beamstop angle is around 3.5° and the opening angle around 12° to 13°. The true opening angles are, as written in the introduction, hard to determine and therefore it is hard to estimate an accuracy of the algorithm. The given uncertainties are only statistical. Nevertheless, the average results of all formulations are in good agreement with the assumed values. The results for $\text{Res}_{1,ext}$ are also numerically stable, and therefore it may very well be that these angles correspond to the correct angles of that device.

Table 3.2: Results in forward direction for three different residuum formulations and extended (ext) formulation with interpolated particle diameter. Six runs were performed. Displayed is the average and standard deviation of the six runs.

	Res_1	Res_2	Res_3
residuum	-	8.062 ± 0.007	6.03 ± 0.011
θ_{BS} in	-	4.20 ± 0.22	4.21 ± 0.34
θ_{FW} in	-	13.1 ± 1.7	13.3 ± 1.6

	$\text{Res}_{1,ext}$	$\text{Res}_{2,ext}$	$\text{Res}_{3,ext}$
residuum	$2.30329 \cdot 10^{-4} \pm 0.00065 \cdot 10^{-4}$	10.13 ± 0.05	0.045 ± 0.005
θ_{BS} in	3.7104 ± 0.0031	4.07 ± 0.31	4.07 ± 0.33
θ_{FW} in	13.340 ± 0.021	13.1 ± 1.9	13.2 ± 1.5

Sideward Direction

The sideward direction can be analyzed separately to the forward direction, since the intensity in the two directions are independent of each other. Different from the forward direction is, that there is no beamstop and an offset angle α_{offset} was introduced. The offset angle gives respect to possible deviations from the targeted 90° in sideward direction, but only in the plane perpendicular to the flow direction. LUM GmbH assumes the sideward opening angle to be $\theta_{\text{SW}} = 24°$. The boundary for the opening angle in sideward direction is $\theta_{\text{SW}} = [19°, 29°]$ and for the offset angle $\alpha_{\text{offset}} = [-2°, 2°]$. The values for the detector function a, b were estimated in the same way as in forward direction. The boundaries for the detector values are $a = [80000, 250000]$, $b = [1, 15000]$.

The results of the optimization in sideward direction are shown in Table 3.3. Contrary to the forward direction, all residuum formulations terminated properly. Although all formulations match $\theta_{\text{SW}} = 24°$, their uncertainty spreads over a few degree (except Res_2), which is too much and therefore useless for the analysis. Also, the offset angle varies by ca. ±1°. The fit in

https://doi.org/10.7795/110.20260122

sideward direction seems to be more complicated than in forward direction. It is easy to see why this is the case when looking at the far-field distribution in sideward direction compared to forward direction.

Since the farfield of spheres in sideward direction is striped (see Figure 4.2 as an example), small changes in the parameters can lead to bright stripes being either inside or outside the field of view. This will drastically change the intensity. Also, changes in the size of particles in the Mie-Regime ($\lambda \approx d$) have a strong influence on the pattern in sideward direction and therefore the intensity. This is less pronounced in forward direction where the farfield is ring shaped (see Figure 6.1 as an example). In forward direction the transition is smoother and follows much more the radial progression of the farfield. Such a behavior is easier to solve by an optimizer.

Table 3.3: Results in sideward direction with optimization algorithm for three different residuum formulations and extended formulation with interpolated particle diameter.Six runs were performed. Displayed is the average and standard deviation of the six runs.

	Res_1	Res_2	Res_3
residuum	3.1 ± 3.6	20.30 ± 0.02	10.340 ± 0.006
α_{offset} in	-0.69 ± 0.94	0.62 ± 0.90	0.71 ± 0.80
θ_{FW} in	24.3 ± 2.6	23.02 ± 0.95	23.6 ± 2.7

	$\text{Res}_{1,ext}$	$\text{Res}_{2,ext}$	$\text{Res}_{3,ext}$
residuum	3.9 ± 6.0	25.11 ± 0.02	13.12 ± 0.03
α_{offset} in	0.33 ± 0.8	0.27 ± 0.78	-0.11 ± 0.81
θ_{SW} in	23.1 ± 1.8	25.7 ± 1.3	24.0 ± 3.0

3.3 Discussion and Outlook

As already touched in the introduction, it is not easy to characterize a flow cytometer. The algorithm seems to work well with the $\text{Res}_{2,ext}$ in forward direction. The algorithm will be tested by LUM GmbH in future for the forward direction. If the algorithm is applicable, this gives the opportunity to characterize a flow cytometer with simple means and without having to disassemble it. In comparison to the method of van de Pol and Ost the presented algorithm is based on an optimization problem, which can handle inaccurate particle sizes and potentially also inaccurate refractive indices. This is a benefit since even standardized particles have a certain spread in their size and could otherwise contribute to errors. Further, the conversion factor used by van de Pol was extended in this work with a linear detection function, covering potential offset currents/intensities. Also, the tedious characterization of the flow cytometers optical properties is no longer necessary.

In sideward direction the solvers could find a reasonable solution, but the spread of about ± 3 degree is too large. Further attempts were made to improve the results in sideward direction, which did not work out and were therefore not presented. One approach was to couple the residuum in forward and sideward direction. The residuum in forward and sideward direction were simply added up. This way the size of the particle has to be such that the scattered intensity in forward and sideward direction match. Not only did this increase the computation time, but the results in both direction did also not change. Further, additional particle

https://doi.org/10.7795/110.20260122

sizes and their corresponding intensity were estimated in Figure 3.1. This also increased the computation time but did not give better correctness. An additional particle size in between of 495 nm and 738 nm was relatively easy to predict, but further particles are a lot more difficult to predict since no path between the other particles is visible. In future experiments a mix of more particles will be useful.

Another topic is measurement inaccuracies. Inaccuracies regarding the particle diameter and the offset perpendicular to the flow direction can be compensated to a certain degree. Inaccuracies like detector noise, offset in flow direction, straylight or nonlinearities of the detector are not included. The question, how stable the optimizer is depending on the severity of the errors stays unsolved.

https://doi.org/10.7795/110.20260122

https://doi.org/10.7795/110.20260122

4

Glare Points in Flow Cytometry

The following sections "Simulating a Scattering Image", "Glare Points for Spherical Particles" are already published as: A. Putz, M. Hussels, J. Gienger; Glare Points in Laser Flow Cytometry; 2023 Photonics & Electromagnetics Research Symposium (PIERS), Prague; DOI:[10.1109/PIERS59004.2023.10221566]

Traditionally, flow cytometry has predominantly focused on the measurement of scattered light intensity as a primary metric for analysis. However, with recent advancements in camera technology, it has now become feasible to also capture images of the scattered light for every single event. This offers completely new possibilities in analyzing the scatterer in detail.

To take advantage of this technique, a transition from using a simple detector to incorporating a camera is required. This necessitates the imaging of light onto the camera sensor, especially in scenarios where previously the light was merely collimated. As elucidated in Section 2.1 the trigger and exposure algorithm has to be adapted since the shortest exposure time of the camera is still too long to avoid motion blur with the usually used flow speeds.

In this chapter, first the model for simulating the scattering image in a flow cytometer will be presented. Then a comparison between measured side scattering images of polystyrene spheres and simulated images will be elucidated. When imaging particles or cells with bright-field microscopy in forward direction, the diffraction-limited geometric shape of the object is visible. In contrast to that, when imaging spheres in the sideward direction, two or more bright spots, known as Glare Points, are visible rather than the spherical outline of the particle. The distance between the outer spots correlates well with the diameter of the particle, which may lead to the conclusion that these are the entry and exit points of the laser beam. This means that, for this explanation to hold, there would need to be the excitation of fluorescent emission or a scattering process that leads to the bright spots appearing in the image. However, this is only valid if light is scattered towards the observered, which is not true for the transition of a beam from one medium into another for plane surfaces. Therefore, other explanations must be pursued. The general effect and the occurrence of the bright spots is a well known effect in the field of aerosol analysis. The spots are called *Glare Points* or *Glare Spots*. In some respects, such as the appearance of Glare Points, these findings are directly relevant to flow cytometry.

https://doi.org/10.7795/110.20260122

Possibly the first theoretical explanation of Glare Points was by Lock in 1987 [92]. He concluded "that the experimental observations on a single water droplet can be understood by Fourier transforming the Mie fields". There were further works on that topic by van de Hulst and Wang in 1991 [93] and more in the 1990s [94, 34, 95, 36]. Although the occurence of Glare Points can be related to flow cytometry, the parameters previously used are in a different range. For example, van de Hulst and Wang chose a particle size parameter of $x \geq 10000$ because "a satisfactory Glare Point experiment can only be performed if x is large. Otherwise it is impossible to measure both the scattering angle and the position of the Glare Point with precision." They chose a small aperture angle to accurately distinguish between different observation directions. Consequently, this small aperture permits sufficient resolution only for observing large particles, due to diffraction limitations. The settings in a flow cytometer are quite different with size parameters well below 100. Also the microscope objectives have a high numerical aperture to capture as much light as possible ranging easily from NA = 0.4 to 0.8. This emphasizes the need for a more robust model, which will be presented in the Section 4.1.

Finally, the model will be extended to the simulation of Glare Points of aspherical particles. For this, Lorenz-Mie theory is not sufficient, which is why the scattering model will be replaced by an discrete dipole approximation. Effects such as surface waves and Mie-resonances will be discussed. To best knowledge, the author did not find any source reporting Glare Points for aspherical particles to date. The author found two sources where measured side-scattering images are shown from e.g. cells using the Cytek Amnis Imagestream flow cytometer, however no explanation, experimentally or theoretically, of the shown bright spots is given [30, 96].

4.1 Simulating a Scattering Image

From here we start with the scattering matrix S and the scattered electric field $\boldsymbol{E}_{\text{sca}}$ as depicted in Equation 2.2. If the scattered electric field on a lens in forward direction is wanted, it is easy to transform them into polar coordinates since the origin is the same and only the θ coordinate has to be transformed to a radial coordinate. In sideward direction this is a lot trickier as can be seen in Figure 4.1, since its central coordinates are at $\theta = 90°$ and $\phi = 90°$. A mapping of spherical to polar or Cartesian coordinates is difficult and lavish, since the center of the lens in sideward direction falls on the equator. For small angles around the origin, the two coordinate systems are approximately parallel to each other, however this changes for larger angles. Therefore, an interpolation on a Cartesian grid is done. This simplifies the further analysis dramatically.

The imaging optics is modeled as one, ideal lens. It was found that simulated intensity patterns for an image formed by a single (objective) lens at a finite distance are virtually identical with patterns simulated for a two-lens system (infinity-corrected objective and tube lens).

Previous theoretical works on Glare Points have conventionally employed paraxial approximations in two distinct aspects: firstly, concerning the spherical-wave envelope of the scattered far-field, and secondly, in the application to the phase function of a thin lens [94, 35, 36]. This methodology is valid for optics with relatively small apertures, leading to notable simplifications within the equations. In this work, which engages optics with opening

https://doi.org/10.7795/110.20260122

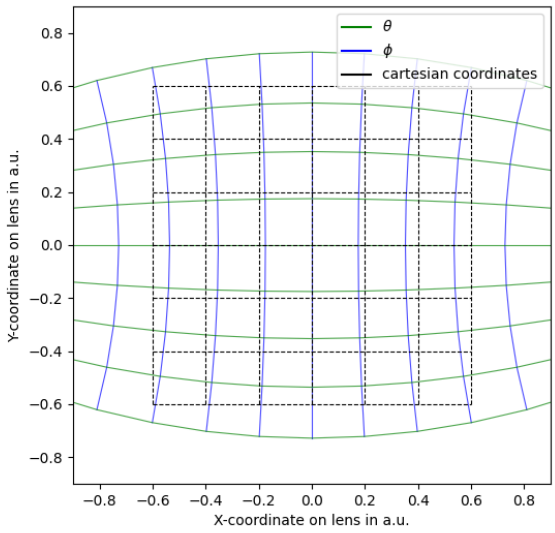

Figure 4.1: Spherical coordinate system at the equator (i.e. in the sideward direction) shown in green and blue. The central coordinate in sideward direction is located at $\phi = 90°$ and $\theta = 90°$. The poles are outside the image on the left and right sides. A Cartesian coordinate system representing a possible lens is overlaid in black. For small angles around the origin, the Cartesian and spherical coordinates are approximately parallel, but this changes for larger angles. Therefore, an interpolation is required to transform between spherical and Cartesian coordinates.

angles exceeding 20°, the spherical-wave envelope and paraxial approximation is not used. In previous tests, which are not shown here, it was found that the paraxial approximation led to poor image quality. Thus, a more accurate model representing an ideal thin lens with phase shift $\Phi(\boldsymbol{r}_{\text{lens}})$ as depicted in Equation 4.1 is used. $\Phi(\boldsymbol{r}_{\text{lens}})$ describes the two dimensional position vector in the lens plane.

$$\Phi(\boldsymbol{r}_{\text{lens}}) = -k_{\text{sca}} \cdot s \left(\sqrt{\left(\frac{\boldsymbol{r}_{\text{lens}}}{s} \right)^2 + 1} - 1 \right) - k_{\text{sca}} \cdot s' \left(\sqrt{\left(\frac{\boldsymbol{r}_{\text{lens}}}{s'} \right)^2 + 1} - 1 \right). \tag{4.1}$$

In Equation 4.1 s denotes the distance from the particle to the lens and the distance s', the distance from the lens to the camera. Note that this equation does not use paraxial approximation, but it is still a thin lens model.

The imaging itself is modeled with the rigorous Rayleigh-Sommerfeld diffraction integral in Equation 4.2, which is more general than the commonly-used Fresnel integral with $\rho = \|\boldsymbol{r}_{\text{image}} - \boldsymbol{r}_{\text{lens}}\|$.

$$\boldsymbol{E}_{\text{image}}(\boldsymbol{r}_{\text{image}}) = -\frac{1}{2\pi} \int_{\Omega} \left(\frac{ik_{\text{sca}} s'}{\rho^2} - \frac{s'}{\rho^3} \right) \boldsymbol{E}_{\text{lens}}(\boldsymbol{r}_{\text{lens}}) \exp(ik\rho)\, d\boldsymbol{r}_{\text{lens}} \tag{4.2}$$

Often, the term $\frac{s'}{\rho^3}$ is omitted because $|ik_{\text{sca}}| \gg 1/\rho$ can be assumed for most practical cases. Since the term does not influence the numerical speed noticeably, it is kept. For the numerical implementation of the Rayleigh-Sommerfeld diffraction integral, a Fourier transform was employed and the 2D convolution integral in Equation 4.2 evaluated in Fourier space. In combination with FFT, this reduces the complexity significantly compared to a direct implementation of the convolution. The intensity on the camera is calculated

https://doi.org/10.7795/110.20260122

via $I_{\text{image}}(\boldsymbol{r}_{\text{image}}) = |\boldsymbol{E}_{\text{image}}(\boldsymbol{r}_{\text{image}})|^2$. The here presented imaging process is sketched and summarized in Figure 4.2.

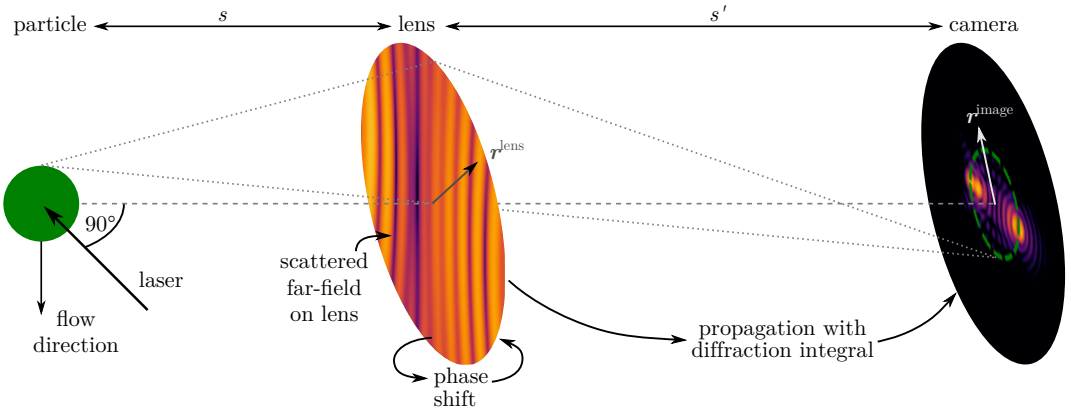

Figure 4.2: Illustration of the simulated image formation process. The steps are as follows: 1) compute the scattered far-field in the lens plane with LMT or ADDA, 2) apply a phase shift $e^{i\Phi(\boldsymbol{r}_{\text{lens}})}$, 3) propragate to the image plane (camera) with the Rayleigh-Sommerfeld diffraction integral. The pseudocolor images show the log-intensity of the field for a 3 µm polystyrene particle (phase not shown). Sizes and distances are not to scale.

https://doi.org/10.7795/110.20260122

4.2 Glare Points for Spherical Particles

4.2.1 Explanation and Comparison with Experiment [1]

The origin of the Glare Points is the rippled far-field structure of the scattered light. In the geometrical optics picture, this can be interpreted as different orders of internal reflections in the particle [93]. Glare points can be divided into three categories: diffraction, reflection and first order transmission [35]. In the case of sideward scattering at $\theta = 90°$, the reflection part dominates and the transmission part is negligible. For larger numerical apertures and particle size d, the reflection Glare Point is clearly distinguishable from the other Glare Points. The reflection Glare Point is the point which is reflected on the surface in an 45° angle. In the geometrical optics picture (which does not strictly apply to the small particle sizes discussed here), this means that the point is visible at a distance $d_{\mathrm{gp}} = \frac{1-1/\sqrt{2}}{2}\, d \approx 0.15 \cdot d$ from the edge of the particle on the illuminated side.

In Fig. 4.3 in the upper row, measured sideward images are shown for 3 µm, 5 µm and 10 µm polystyrene spherical particles. The spheres geometrical cross sections are indicated by bright translucent disks to illustrate the positions at which the Glare Points are observed. The laser beam propagation is from left to right. The medium around the particle is water with a refractive index of $n_{\mathrm{medium}} = 1.3431$ [53] and a laser wavelength $\lambda_{0,\mathrm{laser}}$ of 405 nm (301.5 nm in water). The particle consists of polystyrene with a refractive index of $n = 1.6263$ [97] [98]. The NA of the sideward objective is 0.4.

The distance d_{gp} between the reflected and diffracted Glare Point predicted by geometrical optics fits very well to the actual distance in the (wave optical) simulation and experiment. This is remarkable, because geometrical optics can not in general be used to quantitatively describe the scattering properties of such small particles. In the simulation, the distance d_{gp} is directly shown on the left side. It should be noted that for a particle diameter of 3 µm the resolution of the optical system is not enough to distinguish the two Glare Points (at least in the measurement), but it is visible that the left Glare Point is broader than a single one should be, indicating it is in fact two points too close together. The occurrence of the reflection Glare Point on the entry side of the laser is independent of particle size but only depended on the imaging systems resolution, i. e., numerical aperture.

Comparing the features of the simulation with the experiment in Fig. 4.3 shows that the agreement is very good. Especially for $d = 5$ µm the sharp separation between the diffraction and reflection Glare Point and its flattening towards the opposite point is equally visible in both, simulation and experiment. Likewise, we observe diffraction patterns around the three Glare Points on experiment and simulation. For $d = 3$ µm there are slight deviations in the center of the sphere. In the simulated image, two additional lines are observed between the points which are not visible in the experiment. However, the lines are very low in intensity and it is challenging to take sideward images of 3 µm at all.

[1] The measurements presented in this section were done by Martin Hussels (PTB)

https://doi.org/10.7795/110.20260122

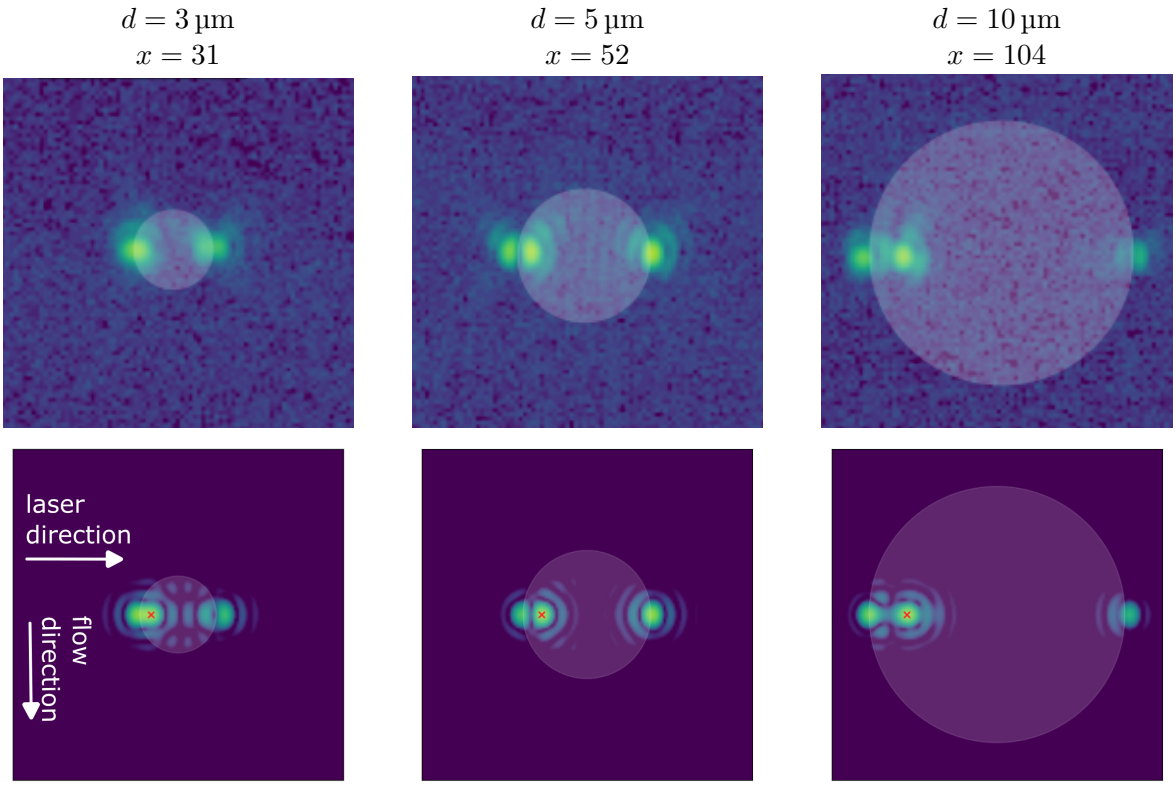

Figure 4.3: Glare point images of polystyrene spheres of different diameters d and size parameters $x = \frac{\pi}{\lambda} d$. $\lambda_{0,\text{laser}} = 405\,\text{nm}$, $n_{\text{particle}} = 1.6263$, $n_{\text{medium}} = 1.3431$, NA=0.4. **Upper Row:** Measured. **Lower row:** Simulated.
Both, measurements and simulations are shown in logarithmic scale with 3.5 decades. The overlaid bright disks indicate the cross section of the respective spheres, based on the magnification and scale. The red cross in the simulated images indicates the position of the reflection Glare Point, predicted by geometrical optics at a distance $d_{gp} = \frac{1-1/\sqrt{2}}{2}\, d \approx 0.15 \cdot d$ from the left edge of the disk.

Glare Points Outside of the Particle

When comparing the overlayed cross sections of the spheres in the measured and simulated images in Fig. 4.3, one recognizes that, especially for 3 µm and 5 µm, the disks seem too small for the Glare Points to fit. The points appear a bit too far outside of the sphere. This was already observed by van de Hulst and Wang in 1991 [93]. They could not give a proper explanation of this phenomenon and suspected that it could be "spillover beyond the angle of the edge rays" or an accumulation of high order rainbows in the extreme edge regions. According to Ref. [35], the distance L between the two outermost Glare Points is

$$L = M \cdot \left(d + \frac{\lambda}{\pi} \right) \tag{4.3}$$

(for mathematical derivation see Refs. [35] and [99]). For water droplets in the range of 30 µm to 100 µm this effect is experimentally irrelevant and not measurable in most cases. In the regime of flow cytometry with particles in the range from sub-micrometer to a bit more than ten micrometer, however, this effect can become relevant and measurable. For a 3 µm particle, according to Equation (4.3), the Glare Points are predicted to lie 4.3% or 130 nm further outside on both sides. One could argue that this distance is lower than the Abbe

https://doi.org/10.7795/110.20260122

limit, which is $\frac{\lambda_0}{2\,\mathrm{NA}} \approx 500\,\mathrm{nm}$ with a numerical aperture of 0.4, and can therefore not be resolved. The Abbe limit describes the smallest distance in which two point-spread functions can still be distinguished. However, the center of a single point-spread function can still be measured/estimated considerably more accurately. Therefore the outer Glare Points are not part of measurement inaccuracy or errors.

Table 4.1 shows the measured distances from the center of the outermost Glare Points to the particle surface.

Table 4.1: Measured distances (based on camera pixels and known magnification) between the outermost Glare Points (left and right) and the particle surface. All quantities are in nanometers.

diameter	Sim. left	Sim. right	Meas. left	Meas. right
3000	150	360	-	140
5000	70	120	30	180
10000	50	230	180	170

The observed distances are close to the expected ones. Nevertheless, one has to keep in mind that it is hard to measure distances in images with limited resolution, noise and other experimental flaws. Moreover, the positions (but not the diameter) of the particles in the experimental images (bright disks in Fig. 4.3) were determined by an "educated guess" with aid of the simulation results. Furthermore, it should be mentioned that Equation (4.3) is derived with the premise of geometrical optics and Fourier-transformation as a lens. The size parameter of, e. g., a 3 µm particle is $x = 31$ which is definitely not in the regime of geometrical optics any more. Some of the effects discussed and described in the geometrical optics framework can apparently still be applied to regimes below $x < 100$ but the quantitative analysis based on it is likely prone to errors.

4.2.2 Influence of Mie-Resonances on Glare Points

Mie-resonances or Mie-Ripples are an already known effect in absorption spectroscopy. James Lock described it as "This type of resonance is called structural since it arises from a matching of the geometry of a single transverse electric or transverse magnetic multipole wave to the size and geometry of the particle, rather than resulting from atomic or molecular excitation of the particle material." in 1990 [100]. Glare points are described as internal reflections in the geometrical optics picture, whereas Mie-resonances are explained by resonant surface waves. In general, surface waves are created when light hits the particle at a grazing angle [94] and a beam that is going through the particle is in resonance with a beam going around the particle.

Van de Hulst describes the occurance geometrically in his book in Chapter 17.52 [57]. A ray of light hits a spherical particle at an grazing angle. There are two possible ways a beam of light can go from point A to B with both on the surface of the particle. It can either go directly through the particle or go around the particle in way as it would be reflected once by an imaginary point P lying on the tangents of A and B, which a geometrically longer way. If the optical path length differs by multiples of the wavelength, a resonance occurs. In the resonant case the surface waves amplitude increases strongly. The lower the index contrast, the longer the necessary geometrical path length APB and the longer the geometrical path APB, the lower in contrast the resonance gets.

https://doi.org/10.7795/110.20260122

From the mathematical point of view, the resonances occur in the real part of the partial wave-scattering amplitudes a_n and b_n [101]. Although these are all ways of separating the creation of Glare Points and Mie-resonances, both effects emerge from the same incident electromagnetic field and can both be described and explained by Lorenz-Mie theory.

In Figure 4.4 the effect of the Mie-Resonances on the extinction efficiency $Q_{\text{ext}} = \frac{C_{\text{ext}}}{2\pi r}$ (with r particle radius) for a particle with a diameter d of 5 µm is displayed. A laser wavelength of 301.5 nm in water corresponds to a size parameter of $x = \frac{\pi d}{\lambda} = 52$. Sharp lines are visible at certain values of the relative refractive index m. In contrast to that in Figure 4.5 the extinction cross section is plotted against a variable size parameter x. Generally one can say that the lines get sharper and stronger for greater values of m and x [101]. In [101] it is reported in order to resolve also the finest resonant lines, a resolution of $\Delta x = 10^{-7}$ is needed. The resolution of the zoom in Figure 4.5 is the same, although they used a larger size parameter x, which means sharper and narrower resonant lines. The existence of those fine lines has also been proven experimentally by A. Ashkin in 1977, which shows it is not only a mathematical construct [102]. An application for Mie-resonances is for example optical trapping with optical tweezers [103] .

If an imaginary part is added to the refractive index, the resonance lines get broader and shallower as reported in [104]. In this work no imaginary part will be added. Only the images of varying relative refractive index will be shown. Although it is mathematically not the same to a varying size parameter, the resonance effect is the same.

In Figure 4.6 selected sideward scattering images with varying relative refractive index m are shown. The wavelength and numerical aperture stay unchanged to Section 4.2.1. From $m = 1.227$ to $m = 1.229$ drastic changes, compared to changes at other positions, happen to the Glare Point images. This is exactly the range in which a resonance occurs in the extinction efficiency. Before and after the resonance the image looks similar, although for $m = 1.235$ the central stripes are more prominent. The reflection Glare Point (compare to Figure 4.3) however does not change position or size. This is expected, since a reflection is independent of the underlying material.

This demonstrates and shows that Mie-resonances do not only have an influence on the extinction efficiency, but also on the appearance of Glare Points. Resonant lines are a very interesting effect, since small changes in the refractive index or size of a particle can have a dramatic effect on the extinction efficiency or the appearance of the Glare Points. The temperature dependency of the refractive index for e.g. fused silica is $8.5 \cdot 10^{-6}/K$ [105]. If the temperature changes by some Kelvin, this will affect the strength of the resonance. Also, the refractive index of material mixtures changes slightly with varying fractions of mixture. The analysis of the extinction efficiency Q_{ext} and the changing of the Glare Points could be an indicator for changing particle parameters. A change of $\Delta x = 0.1$ is equal to ≈ 9.6 nm, which is roughly the width of a resonant peak. This means that changes in the diameter by a few nanometer can also have a strong impact on the Glare Points. In the authors opinion this effect is only partially suitable for particle characterization. Commercial, high quality reference material usually has a coefficient of variation of about $2 - 5\%$ in size. For 5 µm this is already ≈ 250 nm. This makes it impossible to know which exact resonance line corresponds to the particle size. Due to the inaccuracy in size, it is also not possible to use the Mie-resonances

https://doi.org/10.7795/110.20260122

in dependency of the refractive index. Further, in flow cytometry it is not intended to reuse particles and check for changes. If particle technology is evolving further in the future and reduces the uncertainty of size significantly, the Mie-resonances can be a suitable effect for detecting minor changes in particles size and refractive index.

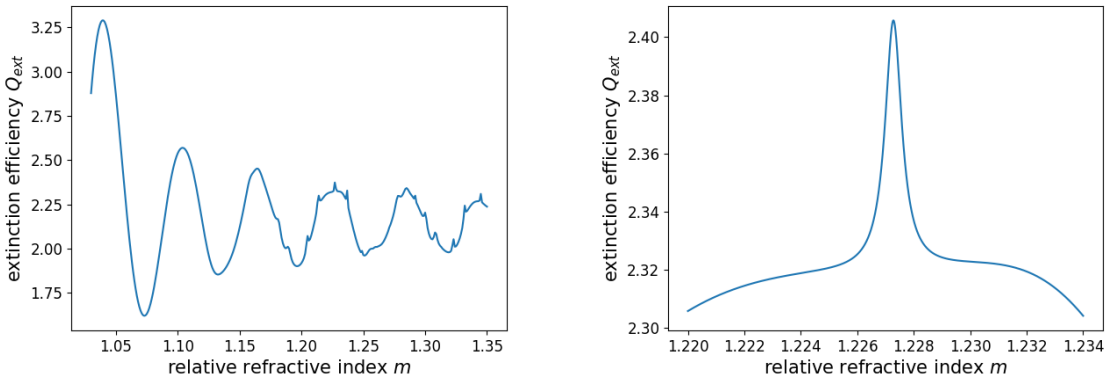

Figure 4.4: Simulation of the extinction efficiency Q_{ext} plotted against the relative refractive index m for a 5 µm large spherical particle. Left as an overview and right as a zoom with a resolution of $\Delta m = 10^{-7}$.

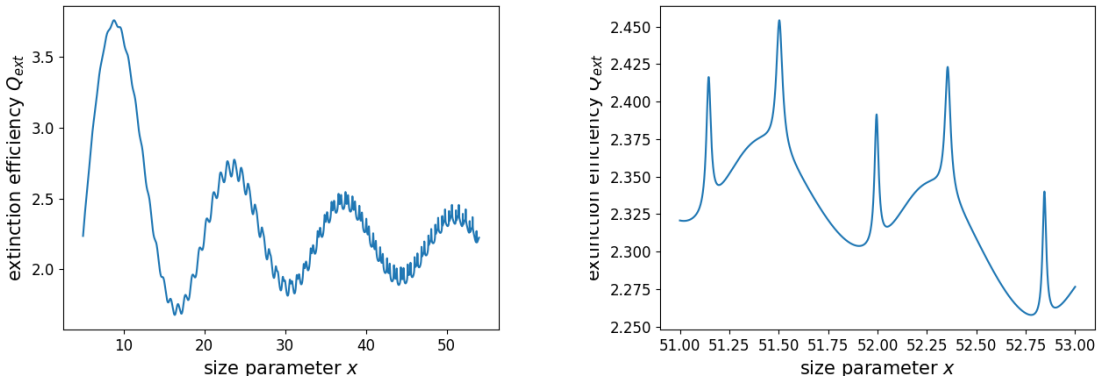

Figure 4.5: Simulation of the extinction efficiency Q_{ext} plotted against the size parameter x for a polystyrene sphere with $n_{\text{PS}} = 1.6263$. Left as an overview and right as a zoom with a resolution of $\Delta x = 10^{-7}$

https://doi.org/10.7795/110.20260122

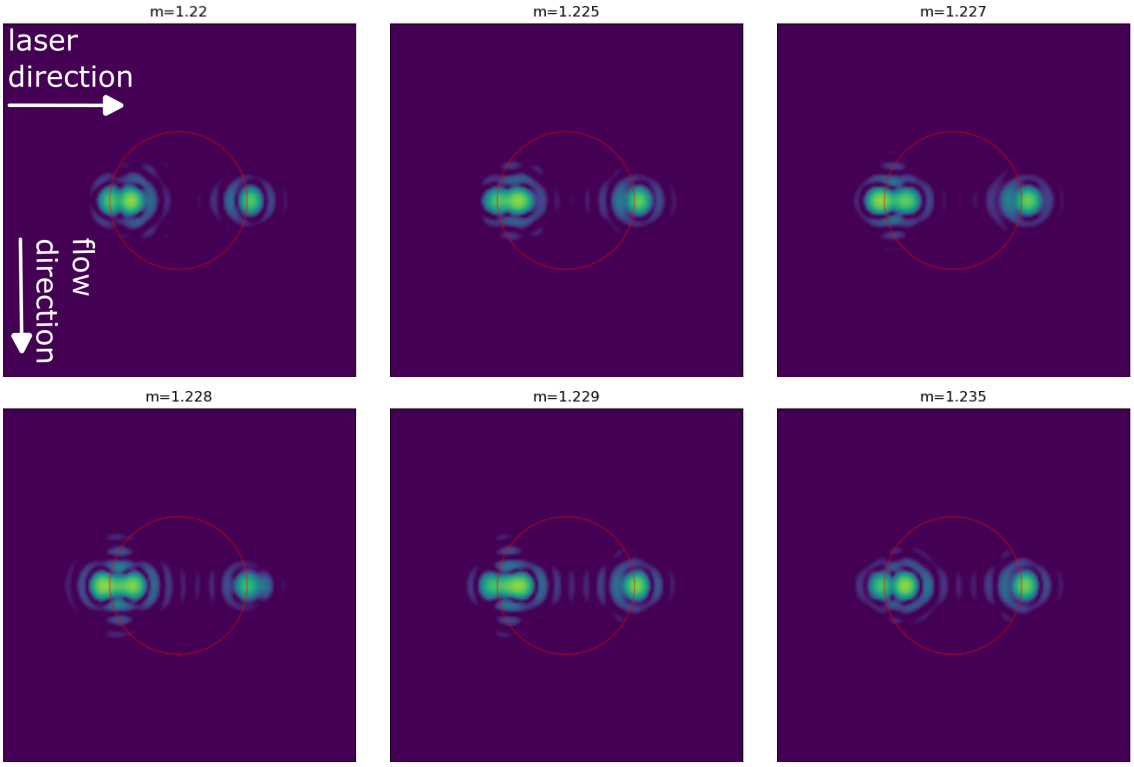

Figure 4.6: Simulated Glare Point images for different relative refractive indices m. The red circle has a diameter of 5 µm. The spatial axes in the images are in micrometer with a magnification of 20. In red the outline of the sphere is depicted.

4.3 Glare Points for Aspherical Particles

4.3.1 Stretched Spheroidal Particles

Spherical particles are relatively easy to describe and characterize compared to aspherical ones. However, in many practical applications, particles deviate significantly from a spherical shape or are deformed. Soft particles or cells, for instance, already deform into an spheroidal shape under moderate stress and can adopt a bullet-like shape under higher stress [37].

Deformation can be induced optically [39] or through fluid shear forces [40, 41]. Commercial devices already exist for measuring the rheological properties of cells subjected to shear forces in narrow flow channels [38], a technique known as *deformation cytometry*.

In this section, the influence of deformation on Glare Points will be discussed as first approximation using an spheroidal model. To the best of the authors knowledge, no sources have reported Glare Points for aspherical particles simulated using a rigorous model to date.

S. Dehaeck studied stretched bubbles with diameters larger than 500 µm using geometrical optics and ray tracing in his thesis [106]. Similarly, J. Lock presented results on Glare Points for spheroidal bubbles in air with diameters of several centimeters [107]. Both works relied on geometrical optics and investigated particle sizes where a rigorous light scattering model was not required.

To simulate the scattered light of an spheroidal, the ADDA code by Hoekstra and Yurkin was used [77] (see also Section 2.5). The spheroid is chosen with different aspect ratios r of its major to minor axis from 0.5 to 2.0. The volume is maintained by adjusting the diameter, as

https://doi.org/10.7795/110.20260122

it would be the case for the deformation of a sphere. The spheroids are prolate for $r < 1$ and oblate for $r > 1$. In the simulation 15 dipoles per wavelength were taken.

The volume is chosen equivalent to a sphere with a diameter of d_{sphere} =5 µm. If not stated differently the other parameters stay the same compared to Section 4.2.1. The case of $r = 1$ relates to a sphere and the image for 5 µm in Figure 4.3. If this sphere is stretched in flow direction, which corresponds to $r < 1$, the Glare Points follow the stretch, but new spots on the surface of the particle emerge as seen in Figure 4.7. The distribution of these spots seems to be equidistant and can be measured with about 650 nm for $r < 1$, which is approximately two times the wavelength in the surrounding medium. Also, the spots are brighter towards the origin of the laser. These spots might be the cause of surface waves. When squeezing [2] the particle along the flow direction, stripes inside of the particle like in Section 4.2.2 occur. The spots on the surface are much less prominent and only around the reflection Glare Point of the laser. However the stripes inside the particle occur for both the stretched and squeezed case.

As already written in the beginning of this chapter, additionally to particles, also biological cells are analyzed in a flow cytometers. Biological tissue has a much smaller refractive index than polystyrene. Depending on the type of cell their refractive index ranges from 1.346 to 1.478 [108]. To see whether Glare Points also appear for such low refractive index and how they behave under stretching or squeezing, the model is run again for a relative refractive index of $m = 1.04$ (i.e. refractive index of $n \approx 1.397$ in water). In all considered ratios, no spots on the surface of the particle emerge. For a ratio of $r = 0.5$ there is some structure emerging at the points where the surface normal is parallel to the laser beam propagation direction, however the structure looks different than with polystyrene particles. For all other ratios there are also stripes inside of the particle. As expected, the reflection glare point follows the deformation of the particle as well.

A final discussion on the stripes and surface waves can be found in the last subsection of this section.

[2] in a flow cytometer the case of squeezing along the flow direction can not be realized, but since the simulation is easy this case is treated as well for better understanding.

https://doi.org/10.7795/110.20260122

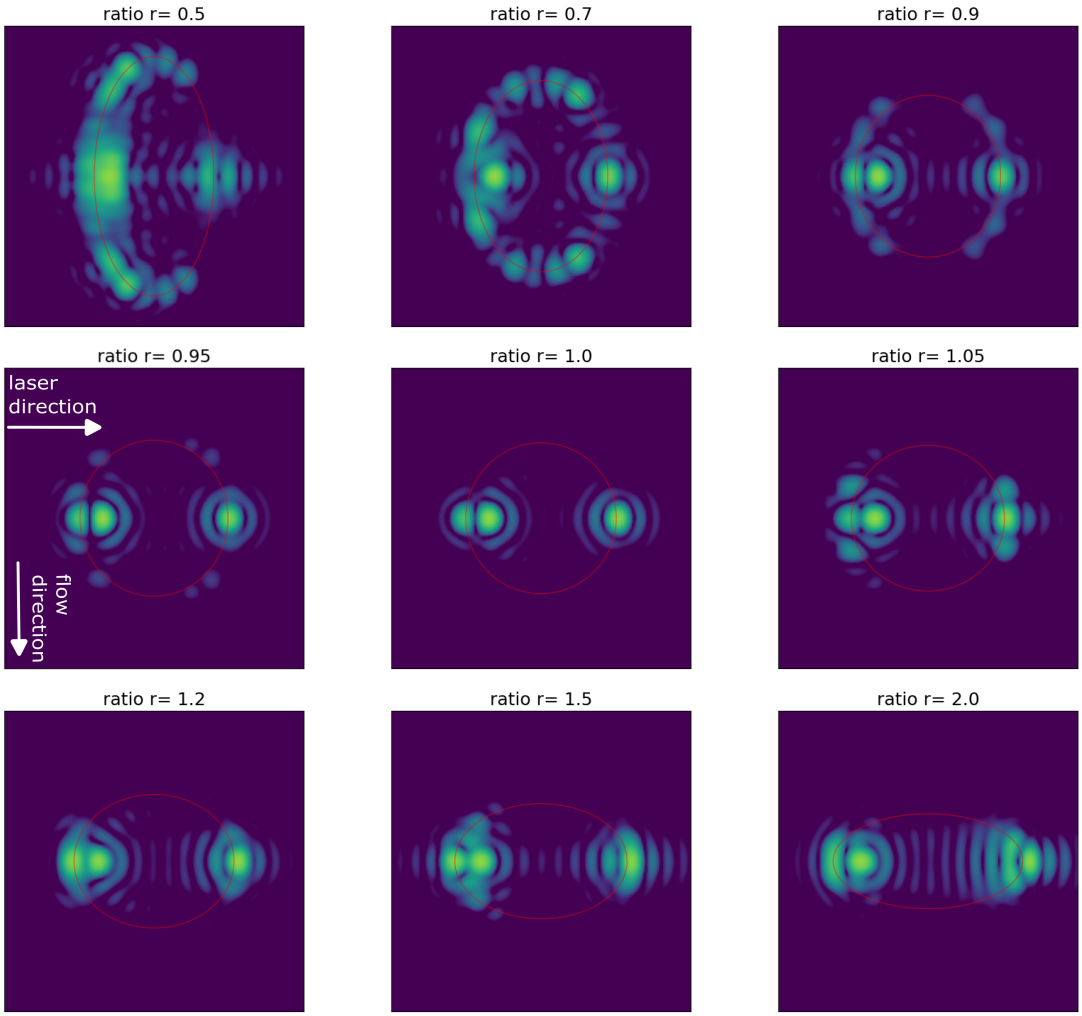

Figure 4.7: Simulated Glare Point images for a polystyrene spheroid with different aspect ratios r. In red the outline of the spheroid is depicted. The spheroid are prolate for $r < 1$ and oblate for $r > 1$. The size is chosen volume equivalent to a sphere with 5 µm in diameter (case of $r = 1$). All images are the same scale.

https://doi.org/10.7795/110.20260122

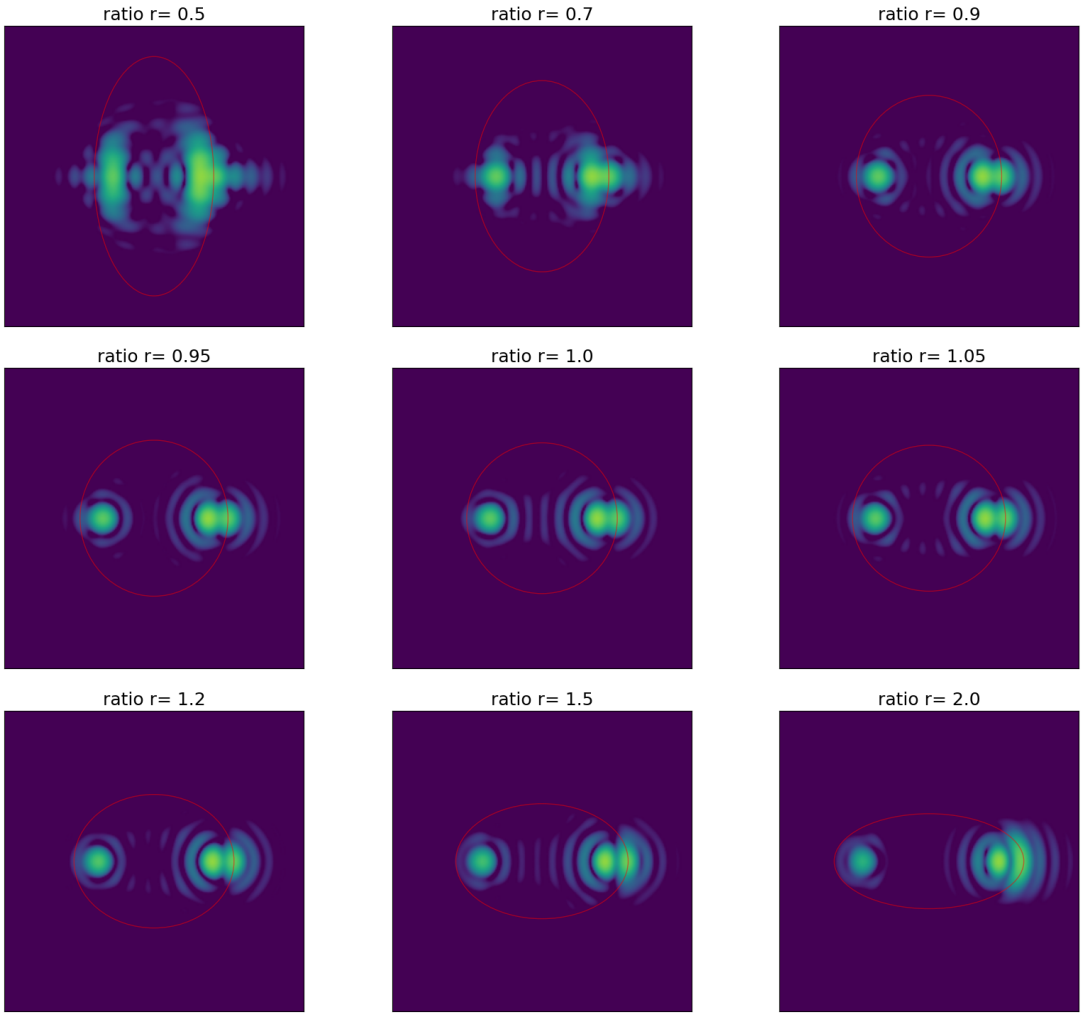

Figure 4.8: Simulated Glare Point images for a spheroid with different aspect ratios r and a relative refractive index m=1.04. In red the outline of the spheroid is depicted. The spheroids are prolate for $r < 1$ and oblate for $r > 1$. The size is chosen volume equivalent to a sphere with 5 µm in diameter (case of $r = 1$). All images are the same scale.

https://doi.org/10.7795/110.20260122

4.3.2 Rotated Spheroidal Particles

For the rotation of particles, a fixed ratio of $r = 0.7$ is chosen. The particles are prolate with a volume-equivalent diameter of 5 µm. This translates to a size of 6.34 µm for the long axis. All shown cases beforehand had a rotation symmetry around the flow direction, which is now broken by rotation around the observing axis. This leads to interesting behaviors and patterns as shown in the results in Figure 4.9. When rotating the particle around the observation axis, the spots on the surface of the particle vanish. It seems that the bright spots on the surface only appear in the configuration of a prolate spheroid aligned along the flow direction. Contrary to the case of an oblate spheroid for a rotation of 90°, the spots on the surface close to the reflection Glare Point vanish completely. The Glare Points seen, rather more resemble these of a sphere. The stripes inside are not visible, however they are probably too faint to see in this specific configuration of size d and ratio r. As seen in Section 4.2.2, the stripes are very sensitive to changes of the size or refractive index. Additionally it is visible that the position of the main Glare Point becomes elongated perpendicular to the laser axis during rotation. A maximum elongation from the laser axis is reached between 30° and 60°. The prominent Glare Point (brightest spot inside the particle on the left side) is the reflection Glare Point, marking the surface which is 45° tilted towards the observation axis (see Section 4.2.1 for reference).

As in the previous subsection, the simulation is repeated for a low relative refractive index of $m = 1.04$, matching that of biological tissue. The results are visible in Figure 4.10. The overall picture is similar to the rotation of polystyrene particles. The most noticeable feature is again the missing of the spots on the particles surface. The Glare Point on the right side is much brighter and seems to consist of two points. This is not unusual, such behavior was e.g. observed for a 3 µm polystyrene particle in Figure 4.3 or when varying the refractive index.

https://doi.org/10.7795/110.20260122

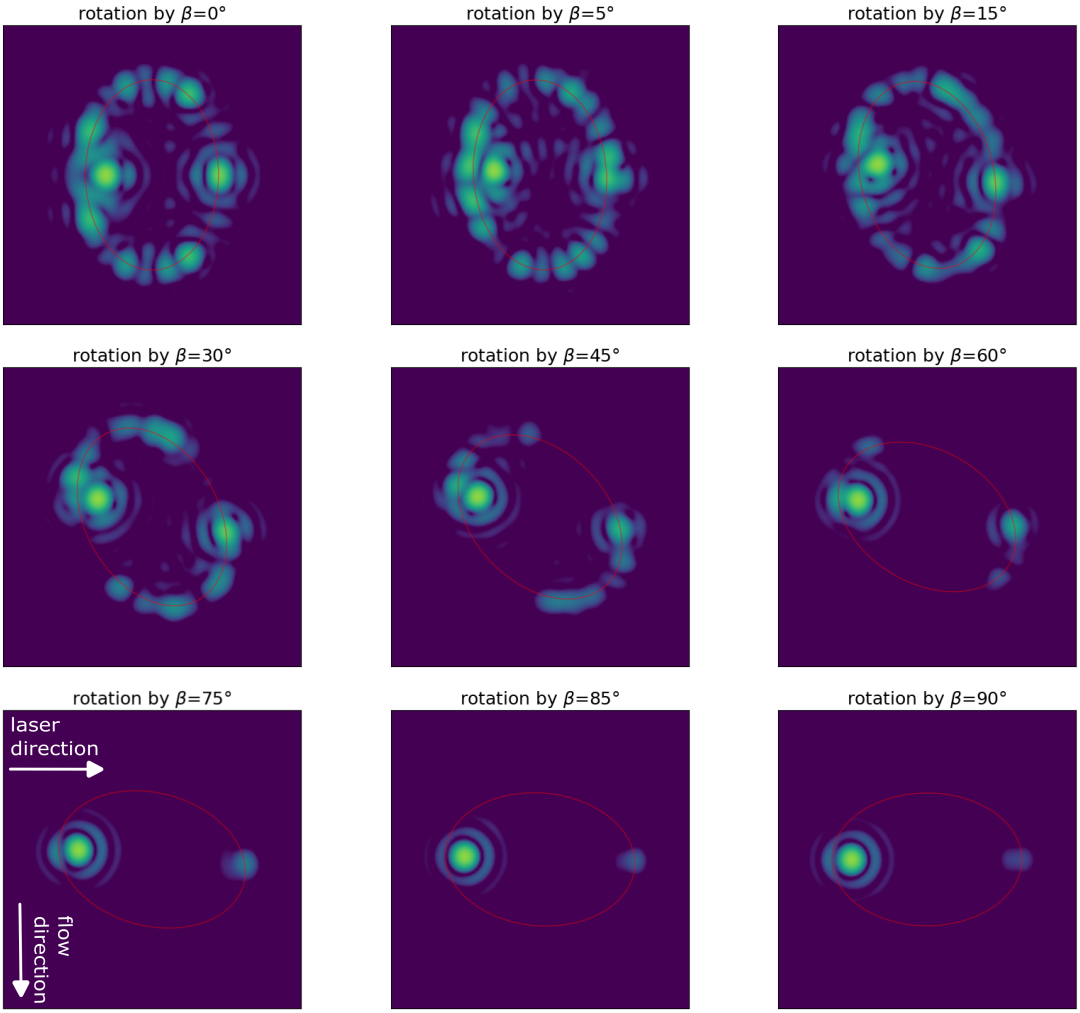

Figure 4.9: Rotation of a prolate polystyrene spheroid with fixed ratio $r = 0.7$. The longest axis is 6.34 µm long.

https://doi.org/10.7795/110.20260122

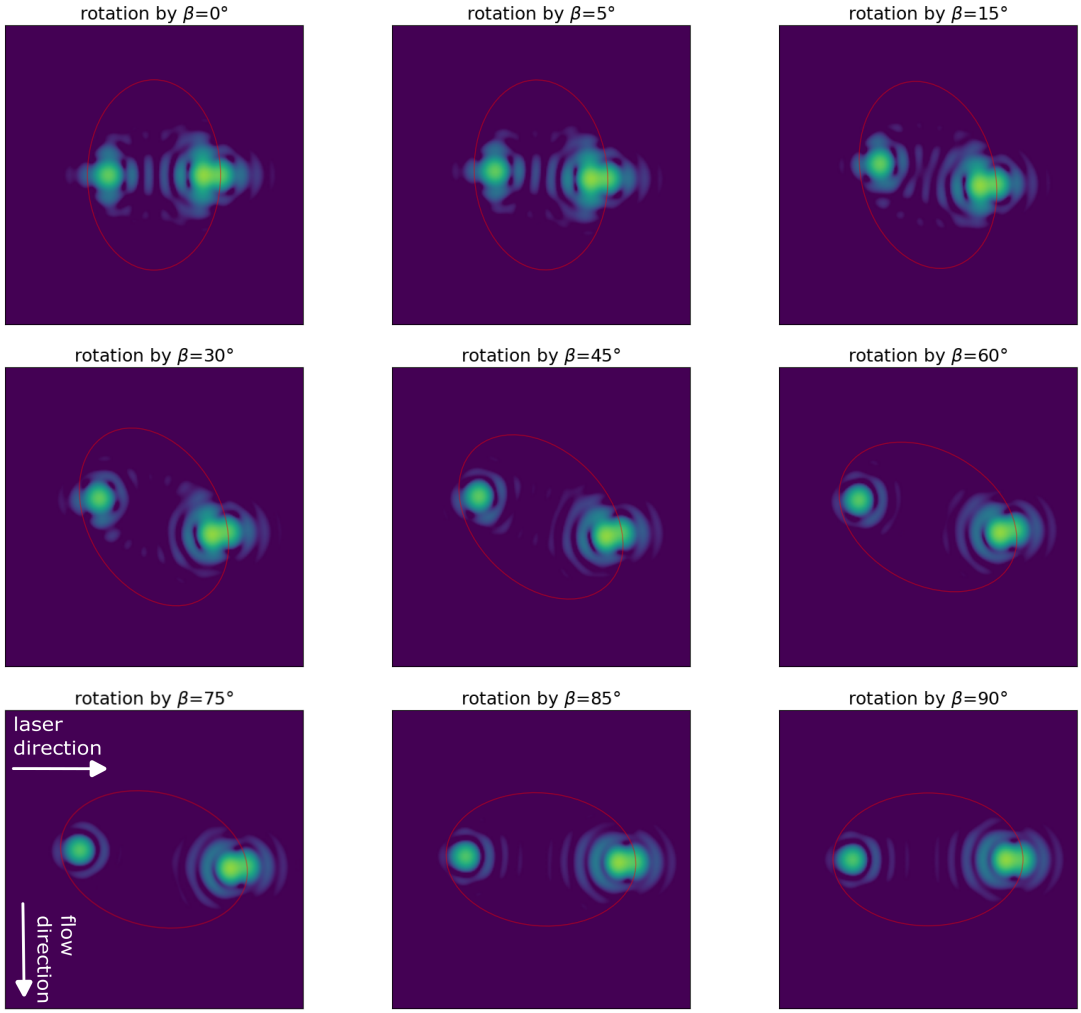

Figure 4.10: Rotation of a prolate spheroid with $m = 1.04$ and fixed ratio $r = 0.7$. The longest axis is 6.34 µm long.

https://doi.org/10.7795/110.20260122

Overall Picture on Glare Points and Surface Waves

There are some aspects that favor and some that are against the thesis that the bright spots on the surface are in fact surface waves. These shall be considered in this subsection.

When stretching particles with a diameter of 5 µm, the bright spots on the surface were observed for a relative refractive index of $m = 1.2109$ and not for $m = 1.04$. The observation fits well with Figure 4.4, in which the first visible resonances occur at a relative refractive index of $m = 1.18$. The distance between the centers of the spots on the surface is roughly two times the wavelength, which favors an interference effect.

When stretching the particles, surface spots appear only for stretching along the flow direction. A first thought could be that this is due to the long, flat side being exposed to the laser, which results in a beam incident rather vertical than grazing. According to Snellius law, this means the beam is propagating rather straight through the particle than being deflected. In the case of an oblate spheroid, there is also a long side exposed to the laser, rotated by 90° compared to the prolate spheroid, however the curvature is greater than the curvature of the prolate spheroid along the stretched axis. It might be that only in this configuration surface waves emerge which are radiating towards the observation direction. The occurrence in dependence of the relative refractive index for rotated particles, also fits to the observations made with stretched and squeezed particles. For further insight, different observation directions will be helpful in possible future works.

Overall the geometrical description of surface waves is just an approximation of the rigorous electromagnetic model. Regardless of whether the spots on the surface emerge from surface waves or not, the effect is fully covered by the discrete dipole approximation.

https://doi.org/10.7795/110.20260122

https://doi.org/10.7795/110.20260122

5

Pulse Shape Analysis

The Section "Detection of Coincidences" is handed in for publication in "Cytometry Part A (ISAC)" with the title "Coincidence Detection in Flow Cytometry using Pulse-Shape Analysis in Polydisperse Suspensions".

While fluorescence staining is widely used and generally unproblematic, fluorescent dyes can sometimes exhibit cytotoxic effects, which may influence the measurement results [109, 110]. The algorithms developed and presented here were designed in a way that they work both on fluorescence signal and scattering signal to overcome possible arising problems with staining.

Usually, in commercial devices, only a single value, like the maximum intensitiy or area, of a particle or cell detection event is registered. This 0D information contains only little information. One idea, which is pursued in this chapter, is to save the whole transit of a particle or cell through the laser, generating 1D intensity versus time data. A whole curve gives much more options for refined analysis and more information about the size, refractive index and shape. With the current technical limitations it is not yet possible to do a real-time analysis of the gathered pulses for high-throughput flow cytometry. Therefore the data is saved as *.tdms* files and post-processed.

For small particles the signal-to-noise ratio (SNR) is very low, which results in the maximum intensity being prone to fluctuations by noise. Due to recording of the whole transit, a fitting algorithm can be employed to increase the populations maximum intensity precision, as presented in Section 5.1.1. This is applicable even for event numbers in the range of millions.

A measurement setup inherently has a dead time in which a new event cannot be recorded. If the time between two consecutive events is shorter than the dead time, a coincidence occurs, reducing the measured number of events. With a higher event rate, the probability of consecutive events undercutting the dead time increases. This incrases the coincidence rate, making the correction of coincidences mandatory in high-speed flow-cytometry, otherwise the counting rate and number of events would be systematically underestimated. Throughputs in flow can easily reach 10 000 events per seconds in commercial devices and beyond, which inevitably leads to a non-negligible number of coincidences [14, 13]. To overcome this, one can either slow down the measurement process, which increases the measurement time, or perform

https://doi.org/10.7795/110.20260122

a coincidence correction. The current state of the art (as layed down in the german Deutsche Industrie Norm (DIN) $58932-3$) stipulates that a dilution series has to be used for coincidence correction [18, 19, 16]. The International Council for Standardization in Haematology (ICSH) has established guidelines for the correction of coincidences which are based on dilution series as well in ISO 15193 and ISO 17511 [20]. The drawback of this method is that at least four measurements are mandatory and a dilution factor spread of four has to be achieved. The counting rates for different dilutions are then extrapolated to infinite dilution, which then yields the statistically correct number of events. This approach assumes that the measurement is Poisson distributed. Another method is the dead-time correction, especially useful if only a small volume of samples is available [16, 111]. However the dead-time correction is only valid for low concentrations and it also requires the dead time of each event to be constant, which is not given in general.

Both, dilution series and dead-time correction have inherent drawbacks, which is why a new method of correcting coincidences by calculating the mean value of the waiting time distribution is presented in Section 5.3. In principle, the waiting-time correction proposed here requires only a single measurement and eliminates the need for dead-time recording. Moreover, it can simultaneously correct coincidences for multiple populations through gating (hierarchical correction). To do this, the time between two consecutive pulses needs to be recorded.

The first attempts on a pulse shape analysis were performed already in 1975 by slit scan cytometers with particles larger than the laser focus [112]. The particle was then scanned by moving through the laser beam, creating a 1D profile [113], on the basis of which the particles can be e.g. further sorted [114]. The first digital pulse shape analysis using the pulse's skewness and kurtosis, as will be employed in this work, was done by Zilmer et. al in 1995 [115, 116], however the data acquisition capabilities were limited compared to today's state of the art. Using the pulse area and kurtosis, they were able to distinguish singlets from doublets and between pecan pollen and lycopodium spores. With the help of the pulses area most coincidences can already be corrected for mono-disperse particles [117], however to correct them more accurate further quantities derived from pulse shapes are needed.

Another recently developed approach is to measure pulse shapes in multiple angles in forward direction by Kage et. al. [42]. Here, the pulse was dismantled in Fourier coefficients by which they were able to asign Jurkat and HEK293 cells to their different cell stages.

In Section 5.2 a modern, high throughput analysis of whole pulse shapes (also referred to as pulse waveform) utilizing their area and moments can yield more information to reliably correct for coincidences. Further, it will be presented on how to identify coincidences of two particle types with very different dynamics at a high throughput range using the standard deviation, pulse area and skewness. It will be shown that the algorithm can identify individual coincidence events, is independent of whether the measurement follows a Poisson distribution (arbitrary particle distribution in flow is possible), and can even be used to check whether a measurement obeys Poisson's law.

The quantities derived in Section 5.1.2 help to improve the measurements by increasing the intensities precision or coincidence detection, but to resolve any shape, a spatial detector is needed.

https://doi.org/10.7795/110.20260122

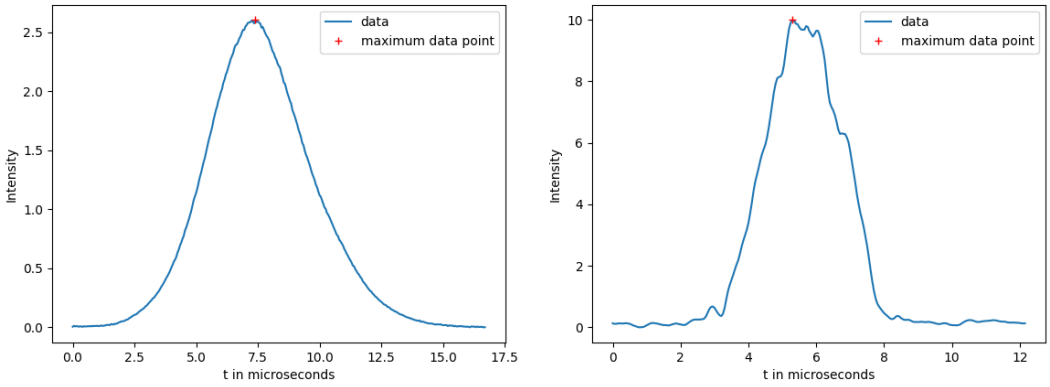

Figure 5.1: Pulse of a spherical particle with left: 1 µm diameter and right: 0.3 µm diameter. The intensity is measured as a ratio of voltages and is therefore unitless.

5.1 Post-Processing of Measured Pulse Data [1]

5.1.1 Pulse Fitting

The acquisition of the scattering intensity involves the Field Programmable Gate Array (FPGA) capturing the temporal scattering signal. Upon receiving the trigger signal, the FPGA initiates the recording of the particle's entire transit through the laser beam. The resulting signal generally mirrors the profile of the laser, if the particle is small compared to the laser beam diameter. The measured signal can be understood[2] as a convolution of the particles geometry along the flow axis with the laser beam profile. If the particle is very small, the result is the convolution of the beam profile with a delta function, which is again the beam profile.

All pulses shown here were captured using the experimental setup described in Section 2.1. For the recording of laser pulses the trigger laser was used, which means the laser wavelength in vacuum for all pulses in this chapter is 488 nm. All polystyrene particles used have a refractive index of $n = 1.6263$.

When looking at robust signals from large particles, the determination of the maximum intensity is no challenge, but when looking at weaker signals from small particles this can lead to inaccuracies or even errors. In Figure 5.1, a comparison between weak (left) and strong (right) signal pulses is shown. The red cross indicates the (temporal) position of the maximum intensity. The strong signals progression is as expected. In contrast, the weak signal shows some oscillations. One explanation for this modulation is: due to the higher gain of the PMT needed to detect weak signals, the noise is equally amplified. The pulse of the strong signal also contains oscillations, they are just too small to be noticed.

After the FPGA has recorded the entire transit of the particle, usually the maximum intensity is determined, saved to a file and the rest of the pulse is discarded. As written above, this can lead to inaccuracies for weak signals. The maximum intensity is higher than it

[1] The measurements presented in this section were done by Alexander Hoppe (PTB)

[2] The convolution is by no means the true model behind the pulse shape. It is just an approximation to understand the behavior. The author did some tests with reproducing shapes of objects in the same size as the laser by using deconvolution on the simulated pulses. The shape was barely reproducable. The information loss of a convolution is too big. Also, in the range of 10 µm there are far superior methods like microscopy and imaging flow cytometry.

https://doi.org/10.7795/110.20260122

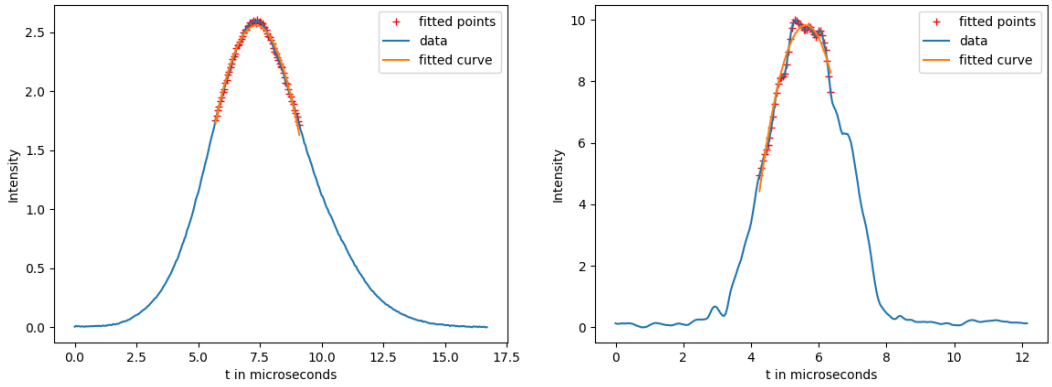

Figure 5.2: Fit algorithm illustrated for a spherical particle with left:1 µm diameter and right: 0.3 µm diameter. The intensity is measured as a ratio of voltages and is therefore unit less.

originally was due to the oscillation errors. In terms of a histogram this means the spread of the maximum intensity increases (i.e. the variance gets bigger) and it is shifted to higher intensities. It is crucial that the populations variance is as small as possible. The smaller it is, the better two close populations can be separated.

To overcome these problems, a fit of the pulse can be employed and instead the maximum of the fit is taken. This was done as follows: The simple maximum is taken as a starting point. From the starting point a "certain amount" (see below) of points to the left and right side is saved. With these points a second order polynomial fit ($f(x) = -a(x-b)^2 + c(x-b) + d$) is done and the maximum of the fit is saved instead of the simple maximum. The benefit of fitting only a polynomial to the top of the pulse is that noise and coincidences at the edges will not affect the result. The fitting algorithm used is the least square algorithm from scipy in python. Note that before the data can be postprocessed, an offset correction is done. This simply consists of searching the lowest value and subtracting all values of the pulse by this value.

It is useful to define the "certain amount" of points in fractions of the standard deviation (see Section 5.1.2) to account for different pulse widths and sampling rates. The points should cover the whole top of the pulse and should not go further than the inflection point of the pulse. The fit is illustrated in Figure 5.2 for 1 µm and 300 nm. In the images an interval of 0.8 times the standard deviation was chosen. Although this method is robust against different pulse widths and sampling rates, one should not blindly trust the value of 0.8 times the standard deviation but check if the fit is reasonable.

After refining the data with a fit, the results for the maximum intensity are depicted in Figure 5.3 and for the maximum intensities position in Figure 5.4 for 100 nm and 300 nm. For both particle sizes, the spread of the maximum intensity has decreased in terms of the standard deviation. As already written, the sharper the population, the better the localization. At 300 nm a shift by a value of around 1 in maximum intensity can be observed, whereas there is no shift visible at 100 nm.

Interesting is, that the (temporal) maximums position of the pulse of 300 nm particle diameter shrank by about 30% but it did not at 100 nm particle size. 30% is remarkably high. By recording the maximums position it is possible to e.g. tune the trigger delay. Also, a

https://doi.org/10.7795/110.20260122

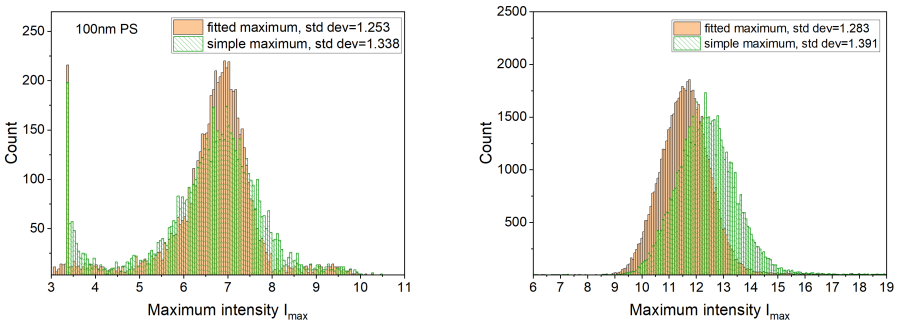

Figure 5.3: Maximum intensity for 100 nm (left) and 300 nm (right) particle diameter. Green: Data with simple maximum. Orange: Refined data received via a fit.

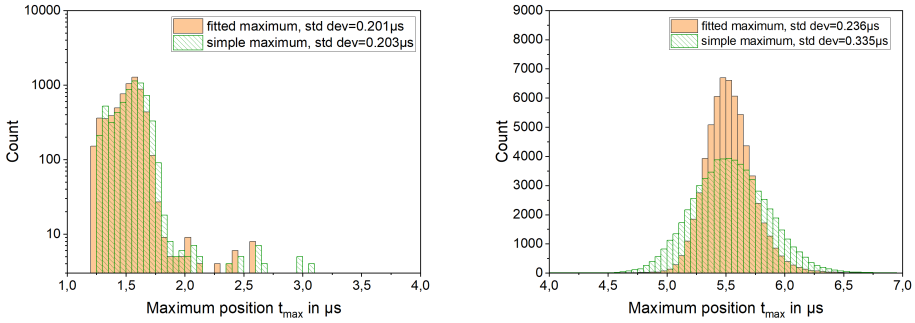

Figure 5.4: Position of maximum intensity in µs for 100 nm (left) and 300 nm (right) particle diameter. Green: Data with simple maximum. Orange: Refined data received via a fit.

very high spread of the maximums position would indicate a fluctuating flow speed and in Section 5.2 it will be used to perform a coincidence correction.

With the help of a fit to the recorded pulse, the localization of low pulses could be improved, as well as the maximums position better determined.

https://doi.org/10.7795/110.20260122

5.1.2 Explanation of Describing Quantities

In the previous section the maximum intensity and its temporal position were determined more precisely. However, additional parameters can further characterize a Gaussian-like pulse, helping to better analyze individual pulses and the overall particle ensemble. The quantities are:

- **maximum intensity**: see Section 5.1.1
- **pulse area** A: The area A is calculated with the integral $A = \int_{t=0}^{t_{\max}} I(t')dt'$
- **maximum position**: temporal position of the maximum determined either by fit or simple maximum
- **95% pulse width**: Determined by excluding the outermost 2.5% from both sides, defining the 95% width of the pulse.
- **noise average** ϵ: average value of the first and last 20 points, defining an offset. These points should only cover noise, no pulse signal.
- **signal-to-noise ratio (SNR)**: $SNR = \frac{I_{\mathbf{max}} - \epsilon}{\rho}$ where ρ is the standard deviation of the same points used for the noise average.
- **slope difference**: $m_{\text{diff}} := m_{\text{end}} - m_{\text{beginning}}$ The difference in slope of the last and first 20 points. This can be used to detect pulses on the edge of the measurement window.
- **pulse validity**: dependent on the average noise, signal to noise ratio and standard deviation, a pulse can be classified as "not OK". It is possible to define other criterea as well. The boolean variable "is pulse OK" will then be set to *False*. This can be used to filter out false or unwanted pulses.

Further statistical quantities are the mean, standard deviation, skewness and kurtosis. The mean value is equal to the first moment and calculated as follows:

$$t_{\text{mean}} = \int_{t=0}^{t_{\max}} I_{\text{norm}}(t') \cdot t' dt' \tag{5.1}$$

Using the mean value, higher centralized moments ($n \geq 2$) can be calculated:

$$\mu_n = \int_{t=0}^{t_{\max}} I_{\text{norm}}(t') \cdot (t' - t_{\text{mean}})^n dt' \qquad \text{with} \qquad n \in \mathbb{N}, n \geq 2 \tag{5.2}$$

With the help of the centralized moments the sought quantities standard deviation, skewness and kurtosis can be defined

- **standard deviation** σ: $\sigma = \sqrt{\mu_2}$
- **skewness** τ: $\tau = \frac{\mu_3}{\sigma^3}$
- **kurtosis** κ: $\kappa = \frac{\mu_4}{\sigma^4}$

Additionally the coefficient of variation can be defined

https://doi.org/10.7795/110.20260122

- **coefficient of variation (CV)**: $CV = \frac{\sigma}{t_{\text{mean}}}$

Since the central moments are integral-based quantities, they can be efficiently optimized numerically. This is particularly relevant when analyzing datasets containing millions of pulses. Furthermore, most parameters can be computed independently, making them easy to parallelize on multi-core computing systems.

5.2 Detection of Coincidences [3]

5.2.1 Modeling of Coincidences

Before looking at measurement data, the influence of coincidences on the mean value, standard deviation, skewness and kurtosis is discussed and to better understand the measurement data.

For that, two pulses, represented by a simple Gaussian function were super-positioned. Some examples are plotted in Figure 5.5 for different (temporal) offsets Δx. Both pulses have an intensity of 1 and a $\frac{1}{e}$ width of 3. From the first to last image (left to right) the time between the first pulse (at $x = 0$) and the second pulse is reduced. Note that the measurement window is fixed to simulate the trigger mechanisms behavior. If the trigger threshold is undercut after the first pulse, the measurement will finish after a certain amount of time, independent whether a second arriving pulse is exceeding the trigger threshold again. In case the trigger threshold is not undercut between the two pulses, they are recorded as one pulse and the measurement is prolonged until the intensity falls finally below the trigger threshold. Whether the limits of the X-axis are prolonged or not should not make a difference in the qualitative result of the simulation.

In the first image there is only one pulse visible with the total intensity and area of one pulse. The second pulse is too far away to influence the pulse in any way. In the second image with an offset of 17.5 the second pulse is slightly inside of the measurement window. The area of the pulse is already increasing. In the third image there is the situation that the trigger level is barely undercut, meaning the second pulse is partly recorded. Nevertheless the area of the pulse is increased drastically and is nearly equal to the area of two pulses. In the fourth image with an offset of 7.5 the trigger is not undercut and the second pulse is recorded completely. The area of the pulse is double the area of a single pulse, however the intensity is still not influenced yet. In the fifth image with an offset of 2.5 it is visually very difficult to distinguish whether the pulse consists of one or two pulses. Although they can not be separated visually, the intensity is still 15% below the intensity of both pulses. In the last image, the offset between the two pulses is zero. The pulse does not differ from a single pulse with the double intensity.

[3] The measurements presented in this section were done by Martin Hussels (PTB) and Susanne Engel (PTB)

https://doi.org/10.7795/110.20260122

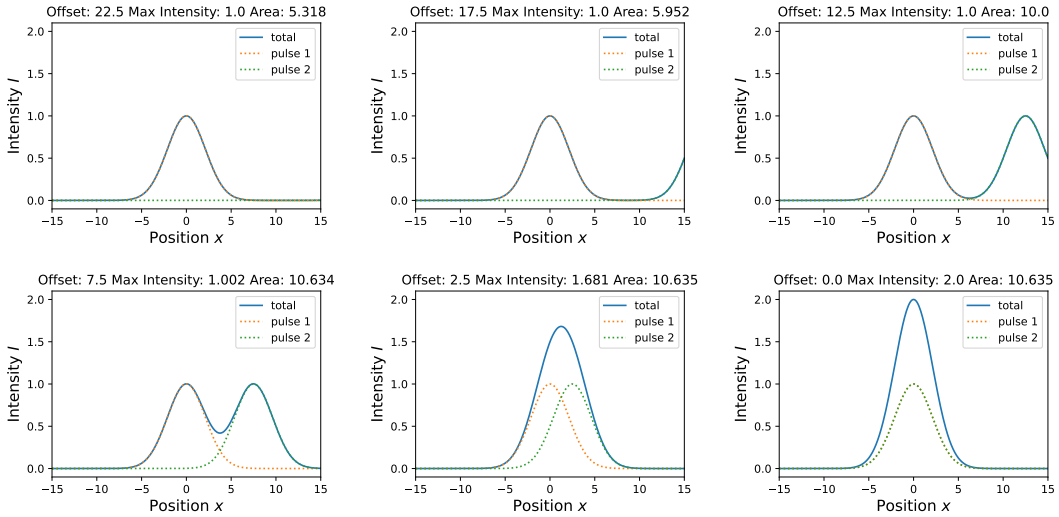

Figure 5.5: Simulation of coincidences with two pulses of the same intensity. The pulses have an amplitude of 1 and a $\frac{1}{e}$ width (i.e. w_0 for a gaussian beam) of 3. The position x can be identified as time to compare the simulation with measurements qualitatively.

The simulation already shows that the pulses have to be very close to see a change in intensity. Even though particle size standard is used, the scattering intensity within a population can fluctuated by 20% to 30% due to e.g. the strong dependence of the scattering signal on the particle size, alignment in the laser, detector noise, etc. . This means that the distance between the pulses has to be very small to identify the coincidences by intensity. The area of the pulse seems more sensitive to coincidences. The area increases in the simulation already at an offset of 17.5. By combining area and intensity, coincidences which double the area but do not influence the intensity can already be identified.

In Figure 5.6 the mean, standard deviation, skewness and kurtosis are plotted for different intensity ratios of the two pulses against their offset/distance. One can see, that the larger the second pulse, the higher the influence on the mean value of the total pulse. The mean value changes quite drastically for an intensity ratio of 1. The mean value is no centralized moment, which implies that the timing of the measurements starting point and ending point have to be precise, otherwise the spread of the mean will increase. This can be seen for example in Figure 5.4. Centralized moments as the standard deviation, skewness or kurtosis are better suited if the precise timing can not be guaranteed. Otherwise it can not be distinguished between bad timing and a coincidence. The standard deviation varies similar to the mean value, with the difference that it is axisymmetric and independent of the timing of the pulse (under the premise that the whole primary pulse is detected). In Figure 5.7 the moments are plotted against the relative area of the consecutive pulse within the measurement window, since the pulse area is the quantity used in the measurement. The offset Δx was varied as in Figure 5.6 and the fraction of the area of the second pulse within the measurement window calculated. A relative area was chosen such that the different graph's courses remain comparable, even though this is not the correct representation in the histogram. An interesting feature of the skewness is that the maximum value of the skewness at an offset close to 0 (i.e. area of the second pulse close to 100%) is achieved by intensity ratios of 0.02 to 0.1 and a skewness of 0 for a ratio of 1. This is also very well visible in the progression of the skewness in Figure 5.6.

https://doi.org/10.7795/110.20260122

Up to an offset of about 12 the skewness remains zero for an intensity ratio of 1 whereas it increases significantly for ratios not equal to 1.

The latter one is not surprising since the asymmetry (i.e. skewness) of two identical pulses around the mean value is zero until parts of one are cut off. The former feature is interesting in the sense that two pulses that differ largely in intensity might be distinguishable by the total pulses skewness. Contrary to that, even if the two pulses occur at the exact same time, a difference of 10% to 25% in intensity or area might not be visible in the intensity or area histogram due to the populations nonzero width. A feature the mean value and skewness share is that based on the sign of the quantity it could be distinguished whether the smaller pulse occurred before or after the primary pulse. In the here used measurement setup the vast majority of the coincidences are in a way that the secondary pulse comes after the primary pulse, due to the way the trigger is implemented. This must not always be the case for different trigger mechanisms. The kurtosis goes either up or down depending on the intensity ratios in Figure 5.7. Recap that the kurtosis is a measure of "tailedness". The larger the value, the "steeper" the curve is. If the pulses are similar in intensity the kurtosis decreases and if they are very different as for 0.01 and 0.02 the kurtosis rises. One disadvantage of the kurtosis is that it has an additional "base line" (i.e. the kurtosis of a single pulse) crossing compared to all other three quantities, very well visible in Figure 5.6. E.g. an offset Δx of about 16 for an intensity ratio of 0.5 has the same kurtosis as if there is only a single pulse. Also, for an intensity ratio of 0.25 the kurtosis seems not to change until an offset of about 12. For this ratio, the kurtosis would be unusable.

According to the modeling, it can be concluded that each quantity has its own range of intensity ratio in which they are suitable. They are evaluated for an offset of $|x| < 7$, since this is the range where both particles are completely recorded. The standard deviation is very suitable for similar intensity ratios like ≈ 0.5 to 1. The skewness performs very well in the region smaller than ca. 0.25 and the kurtosis very well in the region smaller than ca. 0.1. Unfortunately, but also not surprising, is that all quantities can not distinguish coincidences with no offset.

https://doi.org/10.7795/110.20260122

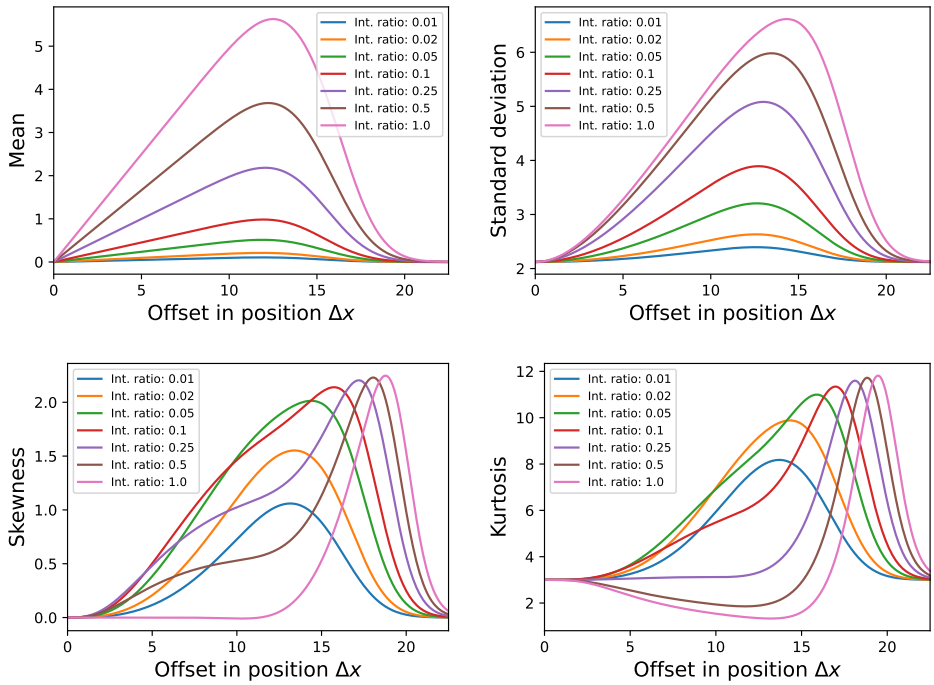

Figure 5.6: Simulation of coincidences with two pulses of different intensity ratios and its influence on the value, standard deviation, skewness and kurtosis in dependence of the two pulses offset. The mean and skewness are point symmetrical and the standard deviation and kurtosis are axisymmetric.

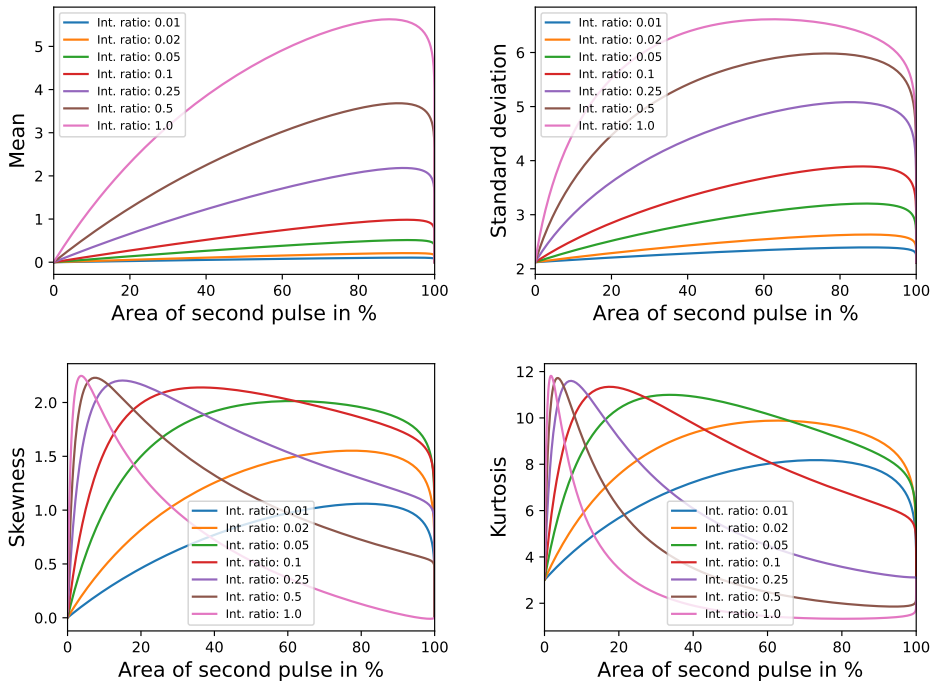

Figure 5.7: Simulation of coincidences with two pulses of different intensity ratios and its influence on the mean, standard deviation, skewness and kurtosis of the total pulse. The first pulse has an intensity of 1 and the second the corresponding intensity. The offset Δx was varied as in Figure 5.6 and the fraction of the area of the second pulse within the measurement window calculated. An area of e.g. 50% means that one half of the second pulse is recorded and 100% that the complete pulse is recorded. Values close to 100% correspond to very low offsets Δx. For the calculation of the area only positive offsets Δx were considered.

https://doi.org/10.7795/110.20260122

Description of Software to Simulate Number of Coincidences

To simulate the number of coincidences that a population A (main population) has with population B (side population) or itself we implemented the following algorithm: A given number of events is distributed uniformly and randomly over the interval $[0, 1)$ and then scaled to the total measurement time t_{total}. The number of events is determined by the average event rate and the total measurement time. In the case of polydisperse suspensions separate intervals are filled for each population individually. During the deadtime t_{dead}, no other particle can be detected. If a second particle arrives during this time, a coincidence will occur.

If the temporal distances between two consecutive particles is shorter than the deadtime t_{dead}, a coincidence occurs. In monodisperse suspensions, for every event in A is checked whether the temporal distance to the subsequent event is shorter than the deadtime ($|t_{\text{A},i+1} - t_{\text{A},i}| \leq t_{\text{dead}}$). If this is the case, a counter for coincidences increases by one. In polydisperse supensions, two separate populations A, B are compared. For every event in A is checked whether the temporal distance to any event in B is shorter than the deadtime ($|t_{\text{A}} - t_{\text{B}}| \leq t_{\text{dead}}$). If the condition is true, the number of coincidences is increased by one. The condition is only checked for the population A because for e.g. 1 µm and 5 µm particles, coincidences of 1 µm with itself or 5 µm with 5 µm can be corrected differently and much easier. The population A would represent 5 µm large particles in this example. The presented algorithm is specifically for the case of a 1 µm particle occuring in the measurement window of a 5 µm particle, since these are the sought coincidences.

5.2.2 Mono-disperse Particles

Now that the behavior of the quantities for coincidences was evaluated, it is compared with measurements. For this, 1.54 µm large spherical polystyrene particles ($n_{\text{particle}} = 1.6263$) were measured. Since this is a mono-disperse suspension, coincidences will have the intensity ratio of 1. The corresponding density histogram is shown in Figure 5.8. Usually the pulses maximum intensity is plotted instead of the area. However, the area is more sensitive, if available in the measurement, in detecting coincidences as described e.g. in [117]. According to the results of the simulation the standard deviation works best for this case. In Figure 5.10 to Figure 5.12 the standard deviation, skewness and kurtosis are visible in a dot plot histogram.The pulses in sideward direction have very similar shape to the forward scatter pulses and add no further information. Hence they were omitted for the pulse shape analysis. Also, the signal-to-noise ratio in forward direction is better for the here used particle size.

The simulations in Figure 5.7 for an intensity ratio of 1 fit very well to the measurements in Figure 5.10 to Figure 5.12. For better visibility the different sections of the visible path of coincidences are gated with different colors. From Gate 1 to Gate 4 the offset between the two pulses is decreasing. Additionally to Gate 4, Gate 5 was introduced since these events show significantly smaller FSC pulse areas than Gate 4 and 3. When comparing the Gates with Figure 5.5 the following correlation can be made. The single events in black can be correlated to an offset of 22.5, Gate 1 (purple) to an offset of 17.5, Gate 2 (light green) to 12.5 to 7.5, Gate 3 (red) to an offset of 2.5 and Gate 4 (dark green) and Gate 5 (blue) with zero offset.

https://doi.org/10.7795/110.20260122

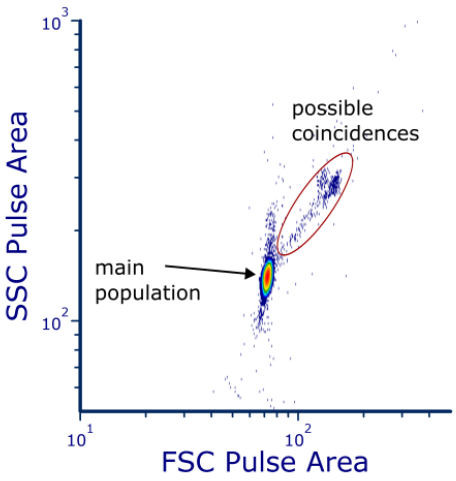

Figure 5.8: Pulse area histogram of 1.54 µm large spherical polystyrene particles.

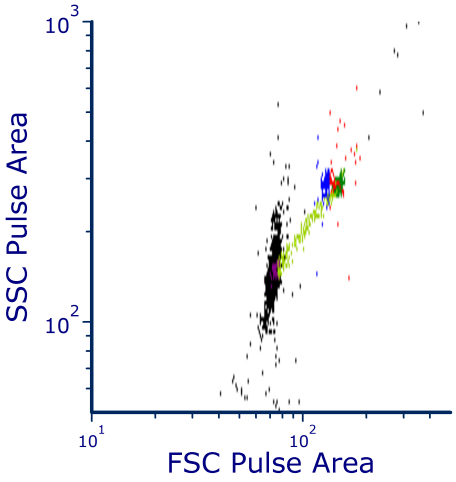

Figure 5.9: The original pulse area histogram with visible Gates. One can see that the purple Gate and parts of the light green Gate would be counted as single events and therefore not correctly recognized.

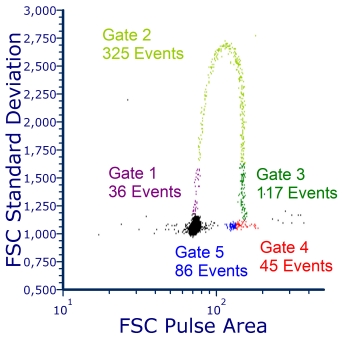

Figure 5.10: FSC standard deviation plotted against the FSC pulse area. The different sections of the visible path of coincidences have been gated with Gate 1 to 5.

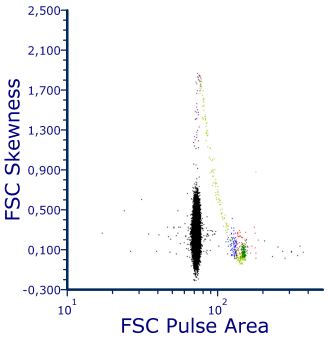

Figure 5.11: FSC skewness plotted against the FSC pulse area.

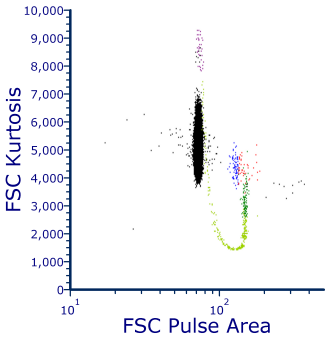

Figure 5.12: FSC kurtosis plotted against the FSC pulse area.

https://doi.org/10.7795/110.20260122

Coincidences vs. Agglomerates

The events in Gate 4 and 5 represent coincidences that are so close together that the offset between the pulses is not distinguishable using the standard deviation. This raises an important question: How can one determine whether a coincidence with zero offset is a true coincidence (independent particles detected at the same time) or an agglomerate (particles stuck together)?

To address this question, pulse shape simulations of particles passing a round laser beam (model barton5) in the flow cytometer were performed using the software ADDA To address this question, pulse shape simulations of particles passing a round laser beam were performed using the software ADDA (see Section 2.5) for two polystyrene spheres ("bisphere" shape model) with variable distances/offsets. By utilizing ADDA for the simulation of two spheres, it is ensured that interference and other possible coupling effects are included in the simulation which is particularly relevant at small inter-particle distances. In contrast, the calculations in Figure 5.5 were a simple addition of generic intensity pulses without any of these effects. Each data point in Figure 5.13 represents a full ADDA simulation at a different position $\tilde{x}$ in the beam, with a sampling resolution of 1 µm. The laser beam width was set to 9 µm, the wavelength to $\lambda_{\text{medium}} = 363\,\text{nm}$, the particle diameter to $d = 1.54\,\mu\text{m}$ and a beamstop angle of 3° and an opening angle of 26.54° (i.e. a NA of 0.6 in water). All simulation parameters were set as close as possible to the real values in the measurement. One deviation from the measurement is that, in this case, an elliptical beam is used with a beam waist of 9 µm along its shortest axis. It has an aspect ratio of approximately 5 : 1 with the long side perpendicular to the flow direction. The particles were aligned along the flow direction (perpendicular to the laser beam), meaning they pass through the laser at different time points.

In Figure 5.13, a comparison is presented between a single sphere, an agglomerate (offset $\Delta\tilde{x} = 0\,\mu\text{m}$), and coincidences at varying distances. Figure 5.14 further illustrates the variations in intensity and pulse area relative to a single sphere for different offsets $\Delta\tilde{x}$.

As expected, for coincidences with large offsets ($\Delta\tilde{x} \geq 12\,\mu\text{m}$), the pulse area is twice that of a single sphere, while the maximum intensity remains unchanged. However, for coincidences at smaller distances ($\Delta\tilde{x} < 3\,\mu\text{m}$), both intensity and pulse area exceed those of an agglomerate (i.e. $\Delta\tilde{x} = 0\,\mu\text{m}$). Although the intensity is only slightly larger ($< 5\%$), the pulse area of coincidences is approximately 12% larger. Notably, at an offset between $\Delta\tilde{x} = 3\,\mu\text{m}$ and $\Delta\tilde{x} = 6\,\mu\text{m}$, the pulse area surpasses even the expected factor of two (i.e. "overshooting").

https://doi.org/10.7795/110.20260122

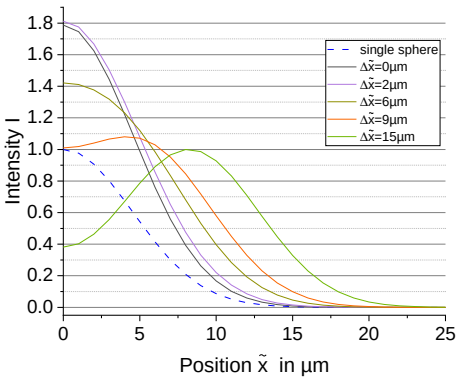

Figure 5.13: Simulated pulse shapes for two spheres with different distances $\Delta\tilde{x}$ between them using ADDA. The intensity is scaled to the maximum intensity of a single sphere. Shown is only one half of the pulses, since they are axisymmetric. The parameters are chosen equivalent to the experiment; with an opening angle of 26.54° and a beamstop angle of 3°. The laser beam width was set to 9 µm, the wavelength to $\lambda_0 = 405\,\text{nm}$, and the particle diameter to $d = 1.54\,\mu\text{m}$

.

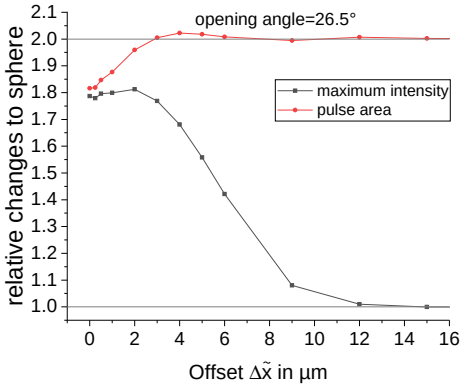

Figure 5.14: Relative changes of pulse area and maximum intensity compared to a sphere for different offsets $\Delta\tilde{x}$ taken from Figure 5.13. Indicated are baselines for the area in red (2) and the maximum intensity in dark grey (1).

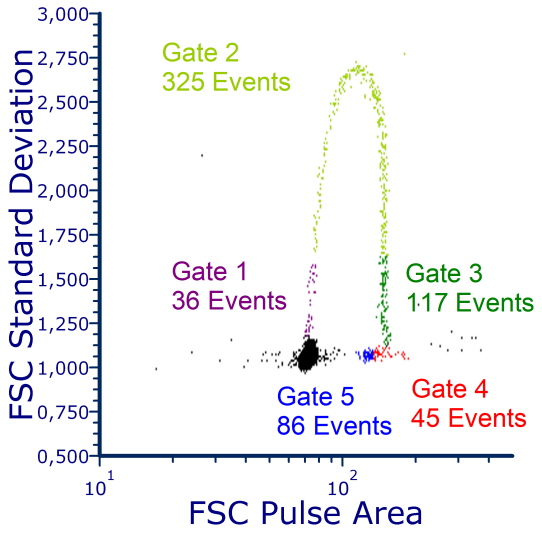

Figure 5.15: FSC standard deviation plotted against the FSC pulse area. The different sections of the visible path of coincidences have been gated with Gate 1 to 5. (shown here again for better comparison.)

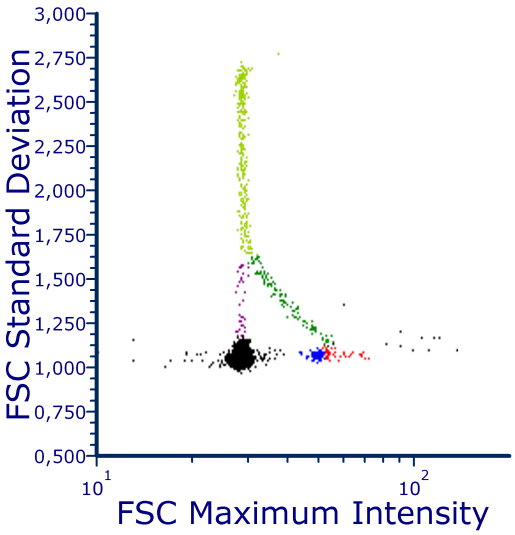

Figure 5.16: FSC standard deviation plotted against the FSC maximum intensity. The different sections of the visible path of coincidences have been gated with Gates 1 to 5.

https://doi.org/10.7795/110.20260122

This raises the question of why the pulse area and maximum intensity deviate from expectations at small offsets and whether the observed overshooting can be explained. The underlying reason is as follows: At $\Delta\tilde{x} = 0\,\mu\text{m}$ (agglomerate condition), the two spheres are within each other's near field range, leading to coupling and interference effects that reduce both intensity and area. At $\Delta\tilde{x} = 4\,\mu\text{m}$, the transition from near-field to far-field interaction occurs, yet the spheres remain close enough that side-scattered light within an approximately 11° half-opening angle can still interact with the adjacent sphere. This secondary scattering redirects previously side-scattered light into the forward direction, increasing the total detected intensity in that direction. Consequently, for $\Delta x = 4\,\mu\text{m}$, the measured area exceeds twice that of two isolated spheres. At offsets of $\Delta\tilde{x} = 6\,\mu\text{m}$ and beyond, the spheres are sufficiently separated to eliminate significant interactions.

For larger particles, simulations indicate that the overshooting effect becomes more pronounced due to increased side-scattered light collection (data not shown). Additionally, the dip in pulse area at small offsets exhibits slight variations. However, the transition between near-field and far-field interactions remains consistent, as it is primarily governed by the wavelength.

In the literature, several studies discuss the differing behaviors of coincidences and agglomerates, particularly in colloid chemistry [118–121]. However, no prior sources were found addressing the cause of varying FSC or SSC intensities for agglomerates in flow cytometry.

Comparing Gate 5 with Gate 4 in Figure 5.15, events in Gate 5 exhibit an FSC area approximately 10% to 20% lower than those in Gate 4. Based on the above considerations, it can be inferred that events in Gate 5 correspond to agglomerates or closely spaced coincidences. Gate 5 was deliberately chosen to have a lower threshold in pulse area than Gate 3 to reduce the presence of very close coincidences. The overshooting of the pulse area of a factor of two in Gate 4 can be attributed to secondary scattering, combined with the increased intensity of possible slightly larger particles at extreme values.

Another noteworthy observation is that, theoretically, the maximum intensity for coincidences or agglomerates should be about 80% higher than that of a single sphere, rather than the naively expected 100%. However, in the measurement in Figure 5.16, the expected 100% increase and even higher values are indeed observed. This discrepancy can be explained by the laser focus shape, which in the experiment is elliptical rather than the used circular shape used in the simulations. When coincidences with large separations are aligned perpendicular to both the flow and the laser beam (i.e., arriving simultaneously in the beam and oriented parallel to the side-scatter direction), both particles are illuminated simultaneously without interference, resulting in a doubling of intensity. Events in Gate 4 can thus also be attributed to this alignment effect.

For small distances, the same principles apply as for particles aligned in flow direction. Simulations further show that coincidences at distances of approximately 10 times the wavelength exhibit an increased FSC area due to secondary scattering, which corresponds to the right-hand region of Gate 4 in Figure 5.15.

Overall, the distinct behavior of closely spaced coincidences observed in simulations provides a compelling explanation for the abrupt changes in FSC pulse area and maximum intensity distributions between Gates 3, 4, and 5.

https://doi.org/10.7795/110.20260122

Gate 5 accounts for 86 events out of a total of 124 015 events. Using Gate 5, an upper limit for the number of agglomerates can be estimated. Since there is no strict boundary between Gates 5 and 4, the transition is gradual, making Gate 5 an approximation.

Detecting Debris and Unwanted by Smaller Particles

However, in the case of more complex samples—such as debris ($\lesssim 0.2$ times the main particle diameter)—simple counting based on scattering standard deviation versus pulse area is insufficient. In such cases, coincidences involving contaminants and the main population can be misclassified as events similar to those in Gate 1, where only the flank of a second pulse falls within the measurement window.

Contrary to the events in Gate 1, the pulse of a small particle must be completely inside the measurement window, but at the edges, to have a perceptible influence on the standard deviation. If the small particle's pulse is only partially inside the measurement window or overlaps with the main pulse, the change in standard deviation is too low to stand out from the noise. In this case, the pulse will not be registered as coincidence and therefore no correction is necessary.

One way to distinguish the two events is by looking at the slope difference as defined in Section 5.1.2. A positive m_{diff} means that either the end of the pulse has a positive slope or the beginning a negative slope. In the case of Gate 1, m_{diff} is always positive for two equally large particles and in case the second is a small particle always negative or zero. By gating all events with a negative or zero m_{diff}, debris can be effectively filtered out.

Conclusion

Summing up Gate 1 through 4 a total of 524 coincidences could be found. Additionally 86 close-distance coincidences or agglomerates were found in Gate 5. Gate 1 through 5 then sum up to 610 coincidence events which is 0.49% of the total 124015 events. By using the software described in the beginning, there are statistically 626 ± 32 coincidences to be expected. This is still in good agreement with the measurement and supports the applicability of the algorithm. A dead time of 25 µs was estimated in the measurements and put into the simulation, however the dead time varies from event to event and there is one type of coincidences that can not be recorded (see Section 2.2). Further, unwanted, much smaller particles can be effectively filtered by using the slope difference m_{diff}. Using the standard deviation and pulses area, coincidences can be found much more reliably than with the area alone, not to mention the intensity. Also an estimation of agglomerates can be done with only one measurement, rather than a dilution series. When using only the area, the distance between the two pulses has to be small enough that a major part of the second pulse is detected. In Figure 5.9 the original SSC area vs FSC area is plotted. The purple Gate (equivalent to an offset of $x = 17.5.$ in Figure 5.5) and parts of the light green Gate would not be recognized as coincidences since the area has only changed by around 10%.

https://doi.org/10.7795/110.20260122

5.2.3 Poly-disperse Particles

Coincidences of mono disperse particles are comparably easy to detect. Next, the coincidence of two different particle sizes will be investigated. Here, four different types of coincidences are possible instead of two. The final goal is to measure the coincidence of erythrocytes and thrombocytes. Although these events are rare, especially with low flow rate, it can be crucial to measure the exact number of thrombocytes e.g. in the case of a thrombocytopenia [122, 123].

Two highly differently sized particles exhibit a highly different maximum intensity. In case of a coincidence of these two particles, the smaller particle can not be resolved, if its maximum intensity is smaller than the spread in the maximum intensity distribution of the larger particle. The same holds for the pulse area. For example in whole blood, the thrombocyte reaches about 10% of the erythrocytes maximum intensity. Prerequisite for the algorithm is, that the two populations are distinguishable from another, which is still the case for whole blood.

To mimic the coincidence of the two most abundant formed elements[4] in whole blood, particles with sizes of 1 µm and 5 µm were mixed with a ratio of 1 : 3 by number concentration, respectively. Their intensity ratio is similar to that of erythrocytes (5 µm particle) and thrombocytes (1 µm particle). Two types of coincidences can be distinguished. Type 1 corresponds to a particle of 5 µm and 1 µm (i.e. erythrocytes and thrombocytes) and type 2 to two particles of 5 µm (i.e. two erythrocytes). Under physiological conditions, the typical ratio of erythrocytes to thrombocytes ranges from 10 : 1 to 30 : 1. To effectively test the algorithm, a higher frequency of type 1 coincidences is desirable, which is why a ratio of 3 : 1 was chosen. When applying the algorithm to real blood samples, no modifications will be made to the blood itself.

In Figure 5.17, the results of the mixed particle measurement are shown. The number ratio between 1 µm and 5 µm particles is approximately 1 : 3, with the remaining 15% consisting of debris.

The ratio in area and intensity for type 1 is about $\approx 10\%$. Looking back at Figure 5.6 and 5.7, it becomes clear that for the sought coincidences of type 1, the standard deviation is less sensitive than the skewness. With that knowledge the majority of type 2 coincidences can be filtered out, since the maximum standard deviation of type 1 is about $\frac{1}{3}$ of the maximum standard deviation of type 2 events. Further, type 1 events will not change the intensity or area noticeably compared to the noise. Using this information, the Gates can be set as visible in Figure 5.18 as an excluding Gate. The remaining type 2 coincidences are the cases where only the flank of the second pulse are within the measurement window (see Figure 5.5 with an offset of 17.5).

For highly unequal intensity ratios, as observed in type 1 coincidences, the skewness exhibits a high sensitivity to changes in offset. Consequently, gating all events with absolute skewness above the noise threshold effectively captures the desired coincidences—except in cases where type 1 events occur with pulses in very close proximity. The skewness can be positive and negative, depending from which side the second pulse is coming, which is why both sides have

[4]Thrombocytes and erythrocytes are actually no cells since they contain no nucleus and supporting DNA [124], therefore the term "formed elements" is more correct. However, whenever the text states that the algorithm is suited for cells, it is also suitable for thrombocytes and erythrocytes. It is irrelevant for the applicability of the algorithm whether these are classified as cell or not.

https://doi.org/10.7795/110.20260122

to be included, although the majority of pulses is positive (coming from the right side) due to the trigger design (see Section 2.2).

To exclude type 2 events where only the flank of the second pulse falls within the measurement window, one can analyze the slope difference m_{diff} defined in Section 5.1.2. A negative slope indicates that the majority of the pulse is within the measurement window, ensuring that the detected slope corresponds to the smaller 1 µm particles. Otherwise, the event would have been excluded due to at least 50% higher pulse area and a significantly increased standard deviation. The lowest negative slope's absolute value must also be the highest positive slope allowed for gating. Events within this range are classified as "True Coincidences," while those with higher slopes are labeled as "False Coincidences."

Some type 2 events may still fall within the "True Coincidence" Gate if the second pulse is only slightly inside the measurement window. However, visual inspection suggests these cases are rare. Despite being a potential source of error, their impact on results is minimal.

In Table 5.1, measured and simulated type 1 coincidences are compared for three different flow and event rates, excluding triple coincidences. At a flow rate of 1.027 µl/s, an estimated 4 to 5 triple coincidences were expected, which is negligible.

The results for flow rates of 0.177 µl/s and 4.425 µl/s show good agreement with experimental data. However, at the highest flow rate of 1.027 µl/s, the expected coincidences are approximately 35% lower than the measured ones. Recall that around 15% of the particles consist of debris. Coincidences involving these, rather than 1 µm particles, are mistakenly classified as type 1 coincidences. Visual inspection confirmed some detected coincidences involving debris, yet these misclassified events alone do not account for the full 35% discrepancy. It also appears that the assumption of a constant dead time in the simulation may lead to deviations between model and measurement with increasing count rate. The trigger algorithm in the measurement does not have a constant dead time, as described in the "measurement and setup" section. Furthermore, the smallest distinguishable temporal distance between two events is only an estimate with 4 µm.

Despite some errors at 1.027 µl/s, the algorithm successfully detects the majority of type 1 coincidences using relatively simple methods.

From a practical perspective, type 1 coincidences constitute approximately 0.067%, 0.154%, and 0.376% of events at 0.177 µl/s, 4.425 µl/s, and 1.027 µl/s, respectively. As the event rate increases, so does the coincidence rate. For an event rate of 5500 1/s, the coincidence rate reaches 1.57%, which becomes significant for precision measurements. While the algorithm was demonstrated for moderate flow rates, there is no inherent limitation preventing its application at higher flow rates.

https://doi.org/10.7795/110.20260122

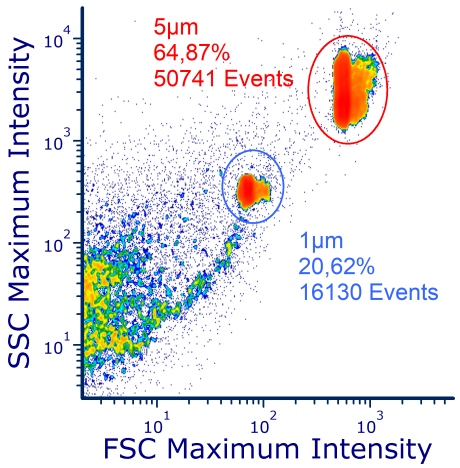

Figure 5.17: Conventional histogram (SSC vs FSC intensity) of a mix of 1 µm and 5 µm large spherical polystyrene particles.

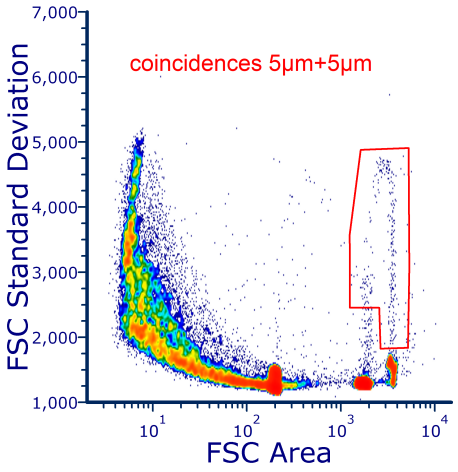

Figure 5.18: FSC standard deviation plotted against the FSC area. The possible coincidences of two 5 µm particles are gated.

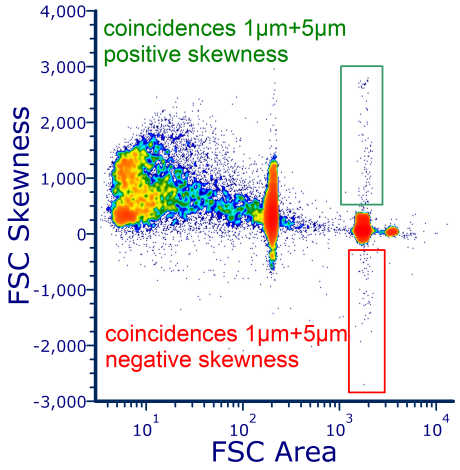

Figure 5.19: FSC skewness plotted against the FSC area. The gated area from Figure 5.18 were excluded. Using the skewness coincidences of 1 µm and 5 µm can be identified and gated. Coincidences of particles with different intensity are sensitive to the skewness.

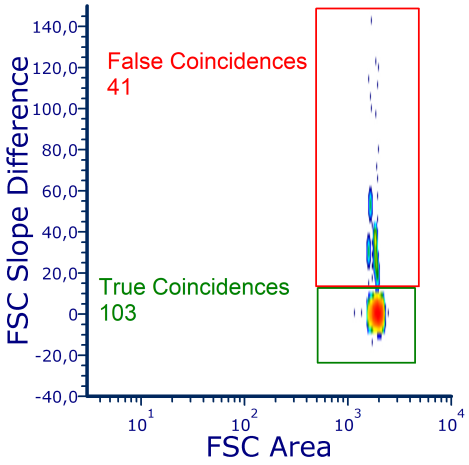

Figure 5.20: FSC slope difference plotted against the FSC area including only the marked gates in Figure 5.19. The absolute value of the lowest negative slope also has to be highest positive slope to gate.

https://doi.org/10.7795/110.20260122

Table 5.1: Comparison of measured and simulated amount of coincidences of type 1 for different event rates. In the simulation the deadtime after each event was estimated with 12 µs and the smallest temporal distance between a 1 µm and 5 µm particle enough to be separated from noise was estimated as 4 µs. The total measurement time was 120 s for all measurements. The specified measurement uncertainty was calculated using the standard deviation of twenty runs.

Flow rate in µl/s	0.177	4.425	1.027
Measured event rate in 1/s	216	557	1274
Measured number of coincidences	22	102	858
Simulated number of total coincidences	25.2 ± 3.2	158 ± 13	839 ± 32
Simulated number of nondetectable coincidences	7.6 ± 2.4	55 ± 5.4	277 ± 20
By simulation expected number of coincidences	17.4 ± 5.6	103 ± 18.4	562 ± 52

5.2.4 Finding Thrombocyte-Erythrocyte Coincidences

The blood sample used in this section was prepared during a round-robin test for external quality assurance.

The algorithm developed for coincidences of 1 µm particles and 5 µm particles is now applied for thrombocytes and erythrocytes in full blood. Their intensity ratio is approximately 5%. The simulation results for this intensity ratio can be seen in Figure 5.7. The measured results are shown in Figure 5.21 to Figure 5.24, similar to the previous results of particles. The measured eventrate for blood is 509 1/s. In comparison to the previous measurement, the quantity ratio is shifted towards the erythrocytes with 90.52%. In total 30 coincidences of thrombocytes with erythrocytes have been found with the algorithm presented beforehand. This is in good agreement with 32 ± 8 coincidences expected by simulation. 28 out of the 30 pulses can be inspected in Figure 5.25. One can see on the basis of the maximum intensity of the two different pulses that the algorithm reliably detected coincidences between erythrocytes and thrombocytes. Even pulses that are skewed due to the two pulses being very close together got detected. Interesting is that there is even one triple coincidence detected. The maximum intensity of the middle pulse does not fit to the intensity ranges of the two populations. This event is probably a rare event between a thrombocyte, an erythrocyte and a debris particle.

https://doi.org/10.7795/110.20260122

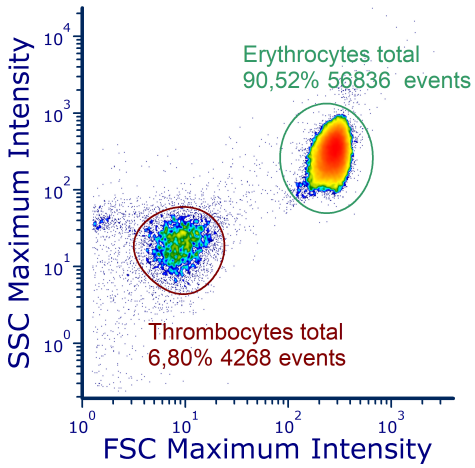

Figure 5.21: Conventional histogram (SSC vs FSC intensity) of a blood sample showing erytrocytes and thrombocytes. The measurement was done with a flow rate of 4.425 µl/s. Other parts of the blood are too low in concentration to be relevant here.

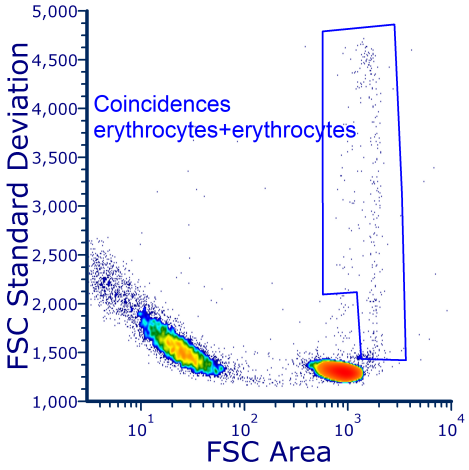

Figure 5.22: FSC standard deviation plotted against the FSC area similar to Figure 5.18 but for blood

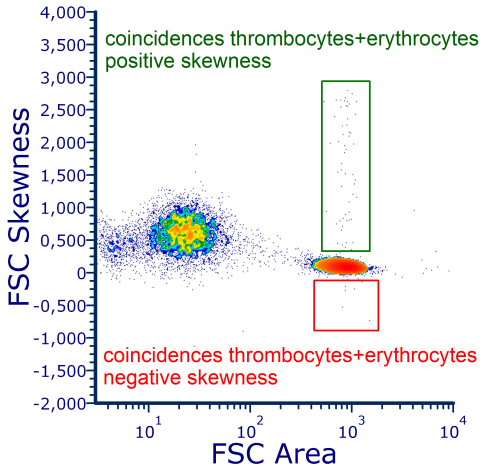

Figure 5.23: FSC skewness plotted against the FSC skewness similar to Figure 5.19 but for blood

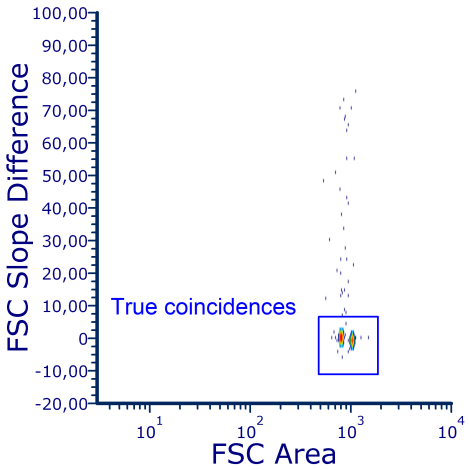

Figure 5.24: FSC slope difference plotted against the FSC area similar to Figure 5.20 but for blood

https://doi.org/10.7795/110.20260122

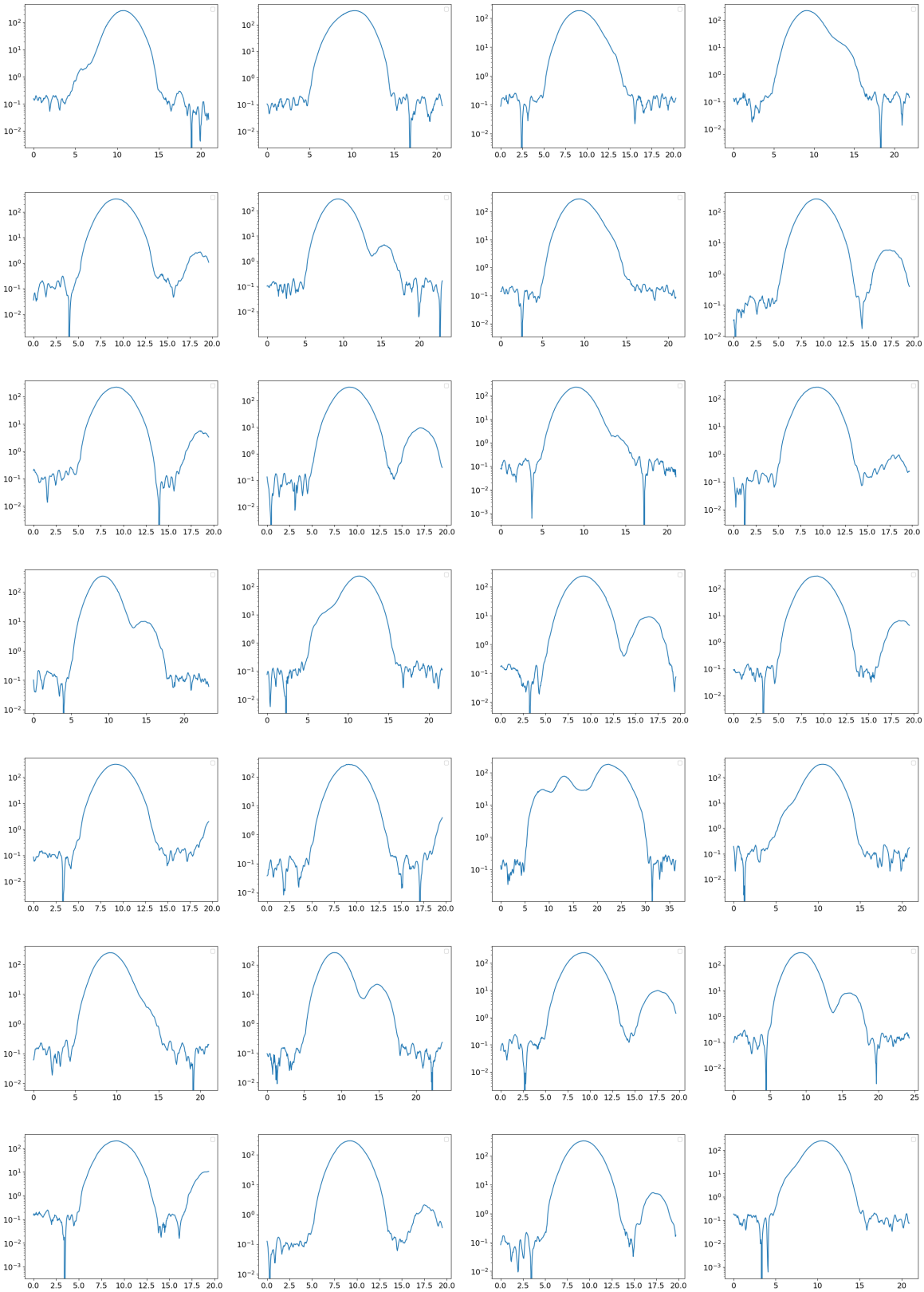

Figure 5.25: X-Axis: time in µs. Y-Axis: Intensity (unitless). Plotted are coincident pulses of type one detected by the algorithm in log scale for whole blood. Shown are 28 of the total 30 pulses. As visible, nearly all coincidences occur between an erythrocyte and a thrombocyte. Some pulses show a broadening, meaning that the two pulses are very close. The intensity is measured as a ratio of voltages and is therefore unitless.

https://doi.org/10.7795/110.20260122

5.2.5 Conclusion and Outlook

In this section, an algorithm capable of detecting coincidences using relatively simple methods was presented. This was presented for monodisperse particles, polydisperse particles and even whole blood as a biological sample. With the help of the standard deviation, coincidences of monodisperese particles can be much better detected compared to using the pulse area or maximum intensity as it is done in conventional devices. Comparing this with simulations it was shown that most coincidences can be found with that algorithm. Even if there is debris involved, given the size is small compared to the main population, coincidences of debris and particles can be distinguished from coincidences between particles and particles.

Also, an upper limit of agglomerates can be estimated by exploiting that agglomerates scatter less light than close distance coincidences of two particles. This is very helpful to refine the dilution steps of the probe and the statistic evaluation of the measurement. The agglomerates seem to be separable by their higher SSC area as seen in Figure 5.9, but by far not as clear as using the standard deviation versus area. Further, by using the standard deviation versus area, only one channel, the FSC pulse is needed, which reduces the costs and complexity of the flow cytometer. If at some point it becomes possible to calculate the standard deviation, maximum intensity and pulse area in real-time, one can sort out potential agglomerates by a subsequent (cell)sorter.

Using the pulses standard deviation and skewness, coincidences of different sized particles could be found and distinguished from coincidences of same sized particles in polydisperse suspensions. Due to impurities in the solution the number of measured coincidences might be prone to errors. The algorithm finds most of the coincidences, however it is much harder to detect coincidences where both particles are very close in time since the influence on the moments decreases with decreasing distance. In contrast to that, it is not possible to distinguish any coincidences of particles different in size only using the intensity or area, if the intensity of the smaller particles is smaller than the intensity spread of the larger particles.

By being able to distinguish coincidences of small and large particles it is possible to determine the absolute number of each particle type more accurate. This enables higher flow speeds without loosing events due to coincidences and saves time if many probes have to be analyzed. The algorithm was also tested on whole fresh blood. It was able to detect coincidences of unlabeled thrombocytes with erythrocytes. Again, this is impossible using only the intensity or area of pulses.

Another major benefit with this algorithm is that the absolute number of particles can be determined in this particular measurement, rather than a statistical value compared to dilution series or the software used. Also, it is possible to filter the coincidences and access these for an individual, enhanced analysis.

Further, the algorithm does not rely on a constant flow rate or non-interacting particles/cells (i.e. obey Poisson distributed). The requirements to the measurement are therefore reduced. Conversely, one can check if a measurement is Poisson distributed by comparing the found coincidences with the statistically expected number. If they deviate too strongly, this is a hint for a non Poisson distributed measurement.

If there are agglomerates in the probe, these will be detected as coincidences by the presented algorithm. Although the number of particles stays correct, since they are detected

https://doi.org/10.7795/110.20260122

as two or multiples instead of one particle, agglomerates are statistically not the same as coincidences. If a potential user is interested in the number of coincidences and not the number of total particles, further measurements with different dilutions have to be done. If the number of coincidences deviate from the statistically expected number of coincidences this is a hint for e.g. agglomerates. The distinction between agglomerate and coincidence is important if a statistical evaluation is used (which is not the case in this section). This problem has been discussed by Hussels et. al in 2019 [117]

The presented algorithm can also be applied to other counting measurement principles where a temporal, gaussian like signal can be acquired (except the upper limit definition for agglomerates which is based on light scattering effects). This can for example be single photon counting [125, 126], where pulses of photons with a defined width are detected. The number of recorded photons can also be such low, that Poisson statistics can no longer be applied, which would not be a problem for the algorithm presented. In a potential biological application the algorithm is very useful if a rare cell type, of which only limited sample volume is available or which might interact, has to be counted. This is a huge benefit over e.g. a dilution series where at least 4 different dilutions have to be prepared and which is based on a statistical evaluation.

https://doi.org/10.7795/110.20260122

5.3 Coincidence Correction [5]

This section has been filed for a patent with the "Deutsches Patent und Markenamt" (german patent and trademark office) under the filenumber "10 2025 109 813.1".

In the last sections, algorithms were presented for the individual detection of coincidences. Here a new algorithm shall be presented which has the potential of replacing dilution series as a statistical coincidence correction. It is based on the statistical evaluation of the waiting times between two consecutive particles. For counting processes in flow cytometry it applies that if the flow conditions are constant during a measurement, the particles are randomly uniformly distributed over time. This means that the measurement obeys Poissons law and the waiting times between pulses are exponentially distributed.

The presented algorithm exploits this behavior for correcting coincidences with the help of the mean value in first and higher order. The algorithm will be presented for the case of particle detection in flow cytometry, but can also be used for all other type of counting measurements, which are able to record the temporal distances between pulses and obey Poissons law.

5.3.1 Waiting Time Distribution in Poisson Regime

If a measurement based on counting entities or events follows Poissons law, the probability $P(k)$ of detecting k number of events after the time t, given the mean event rate a, can be determined using the Poisson equation as follows

$$P(t,k) = \frac{(a \cdot t)^k}{k!} \mathrm{e}^{-a \cdot t} \tag{5.3}$$

The probability that after the time t an event has already occurred is $Q(t, k > 0) = 1 - P(t, k = 0)$ and its probability density $F(t)$ therefore

$$p(t) = \frac{d}{dt} Q = a \cdot \mathrm{e}^{-a \cdot t} \tag{5.4}$$

The probability density p describes the probability that after an event has occurred, another event will occur after a waiting time of t [21]. The averaged waiting time for N measured events is

$$\langle t \rangle \equiv \frac{1}{a} = \frac{1}{N} \sum_{i=1}^{N} t_i \tag{5.5}$$

For a sufficient N, $\langle t \rangle$ converges to its true value $\frac{1}{a}$. The reciprocate value of a equals to the mean waiting time. t_i is the waiting time corresponding to each i^{th} event [6].

If the dead time is larger than zero, there will be counting losses due to coincidences, meaning the counted events N' will be smaller than the true number of events N. As depicted

[5] The measurements presented in this section were done by Susanne Engel (PTB)

[6] t_1 here means, this is the waiting time between the start of the measurement and the first event, denoted as $t_{0,1}$ in Figure 5.28

https://doi.org/10.7795/110.20260122

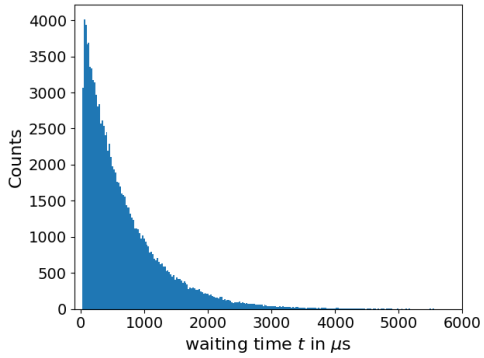

Figure 5.26: Counts versus waiting time for the blood measurement shown in Figure 5.21 with a flow rate of 1.027 µl/s as an example. The counts increase exponential for shorter waiting times according to Equation 5.4 until the waiting time is close to the dead time of the detector.

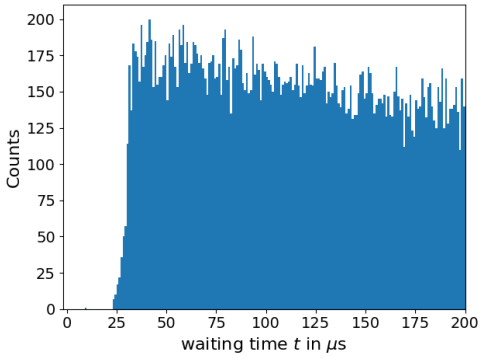

Figure 5.27: A zoom of Figure 5.26 to shorter waiting times. The drop in counts is well visible for waiting times shorter than about 40 µs. Events with shorter waiting times are within the measurement window of another measurement and therefore a coincidence.

in Figure 5.28, the third pulse will be coincident with the second, meaning the waiting time between the true second and true fourth pulse will falsely be recorded as waiting time between the second and third pulse and with the recorded waiting time $t_{2,4}$ instead of the true $t_{3,4}$. The waiting times will therefore be overestimated.

If the number of events are plotted against the waiting times, an exponential decay can be seen for example in Figure 5.26 as predicted by the probability density in Equation 5.4. This is valid until the waiting time reaches about 40 µs where the number of counts decreases and a gap becomes visible. The measurement window for the shown probe is about 25 µs long (this varies of course from measurement to measurement), which is the approximate dead time of the measurement. This is also the time where no shorter events are recorded. All events shorter than this time will be recorded as coincidences in other measurements.

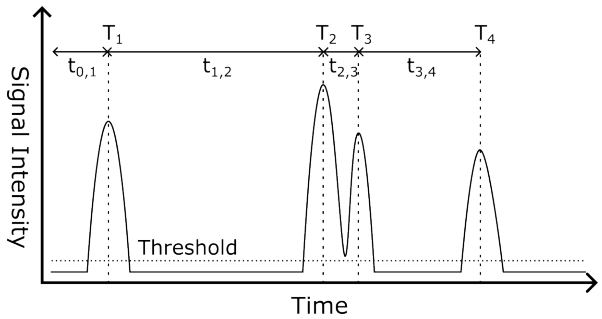

Figure 5.28: Distribution of waiting times t between different counting events at timepoints T. If the waiting time $t_{2,3}$ is too short to be recorded, the waiting time between event number 4 and its predecessor will be overestimated with the value of $t_{2,4}$ (the correct value would be $t_{3,4}$). In flow cytometry, the timepoints of the events can be determined with the maximums temporal position presented in Section 5.1.2. Figure created by Martin Hussels.

https://doi.org/10.7795/110.20260122

5.3.2 Correction Algorithm

Coincidence Correction in 1^{st} Order

To determine the mean value of the probability density p in Figure 5.26, it is sufficient to determine the mean value of a subsection $t > t_0$ of the graph, which is valid due to the self-similarity of the exponential function. The measured average value $\langle t \rangle$ of the waiting time on the interval $t = [t_0, \infty)$ for a subsection then is equal to the mean value on the interval $[t_0, \infty)$ for a sufficiently large N. The integral is dependent on the mean value $\frac{1}{a}$ of the waiting time for the whole interval, for which the equation can be rearranged:

$$\langle t \rangle = \frac{\int_{t_0}^{\infty} tp(t)\,dt}{\int_{t_0}^{\infty} p(t')\,dt'} \tag{5.6}$$

$$\frac{\int_{t_0}^{\infty} tp(t)\,dt}{\int_{t_0}^{\infty} p(t')\,dt'} = \frac{\int_{t_0}^{\infty} tae^{-at}\,dt}{\int_{t_0}^{\infty} ae^{-at'}\,dt'} = t_0 + \tfrac{1}{a} \tag{5.7}$$

$\frac{1}{a}$ then can be calculated as follows from $\langle t \rangle$ on the interval $t = [t_0, \infty)$:

$$\frac{1}{a} = \langle t \rangle - t_0 \tag{5.8}$$

For a measurement with waiting times $t_i > t_0$ and N' events, this yields

$$\frac{1}{a} = \frac{1}{N'} \sum_{t_i > t_0} t_i - t_0 \tag{5.9}$$

The value t_0 has to be chosen such, that it is larger than the dead time or gap for short waiting times. One way to choose a proper value for t_0 is to plot the mean value of the waiting time $\frac{1}{a}$, calculated from the measured average waiting time, versus a variable cut off time t_0 as depicted in Figure 5.29. $\frac{1}{a}$ decreases for very short times t_0 until it becomes a constant value. If t_0 reaches a value at which no coincidences occur, Equation 5.6 (more precise, the analytic calculation of the first moment/mean value) becomes true. The formulation is only true if the waiting time distribution behaves like an exponential function for $t > t_0$. One possible way of finding a suitable value for t_0 is to find the first local minimum of $\frac{1}{a}$. Other ways could include a condition: if the slope in the constant section exceeds a certain level, go back a certain distance and define this value as t_0. With the now determined mean value $\frac{1}{a}$ and the measured number of events N', the correct number of events N can be determined using Equation 5.10.

$$\frac{N}{\int_0^{\infty} ae^{-at}\,dt} = \frac{N'}{\int_{t_0}^{\infty} ae^{-at}\,dt} \rightarrow N = N' \cdot e^{at_0} = N' \exp\left(\frac{N' t_0}{\sum_{t_i > t_0}(t_i - t_0)}\right) \tag{5.10}$$

Coincidence Correction in 2^{nd} Order

In case of a coincidence, the determination of the waiting time undergoes a systematic error. As previously described on the basis of Figure 5.28, the waiting time $t_{3,4}$ will falsely be recorded as $t_{2,4}$ due to a coincidence and therefore overestimated. The correct waiting time for $t_{3,4}$ is $t_{3,4} = t_{2,4} - t_{2,3}$. The coincidence correction in 2^{nd} Order aims to exclude the waiting time

https://doi.org/10.7795/110.20260122

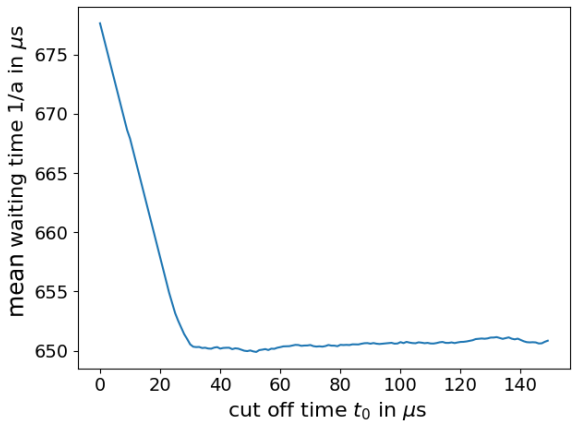

Figure 5.29: Measured mean waiting time $\frac{1}{a}$, calculated from the average waiting time $\langle t \rangle$ as in Equation 5.9, shown for a variable cut off time t_0.

for all events that are shorter than t_0. From the true and corrected waiting times for events longer than $t > t_0$ the mean value for the same intervall is calculated. Due to the self similarity of the exponential function, the true and corrected mean for the whole interval can then be inferred from the true, corrected mean for $t > t_0$. With the help of the corrected mean the sought true number of events N can then be determined. The sum of all recorded waiting times $T = \sum_{i=1}^{N'} t_i$ has to be replaced with the corrected T' with $T' = \sum_{i=1}^{N'} t_i - \sum_{t_i, i=1, t_i<t_0}^{t_{N'}} t_i^\star$. This means that the true sum of waiting times of the recorded events is smaller than the recorded waiting time of the recorded events. This is no contradiction, since in the recorded waiting time, waiting times are overestimated by coincidences. The recorded waiting time is equivalent to the sum of the true waiting times of the true number of events. Note that besides the corrected waiting times ($T' < T$), also the recorded number of events N' is smaller than the true number of events N.

This means, the corrected calculation of the average is

$$\langle t \rangle = \frac{T'}{N'} = \frac{1}{N'} \left(T - \sum_{t_i, i=1, t_i<t_0}^{t_{N'}} t_i^\star \right) = \frac{T}{N'} \left(1 - \frac{\sum_{t_i, i=1, t_i<t_0} t_i^\star}{T} \right) \tag{5.11}$$

To determine the fraction $\frac{\sum_{t_1, t_i<t_0}^{t_{N'}} t_i^\star}{T}$, the self-similarity of the exponential function and its mean value can be exploited again as follows

$$\frac{\sum_{t_1, t_i<t_0}^{t_{N'}}}{T} = \frac{\int_0^{t_0} tp(t)\, dt}{\int_0^\infty t' p(t') dt'} = \frac{\int_0^{t_0} tae^{-at} dt}{\int_0^\infty t' ae^{-at'}\, dt'} = \frac{\frac{1}{a} - \left(t_0 + \frac{1}{a} \right) e^{-at_0}}{\frac{1}{a}} = 1 - (at_0 + 1)e^{-at_0} \tag{5.12}$$

Inserting Equation 5.11 into 5.8 yields a corrected mean value a'

$$\frac{1}{a'} = \langle t \rangle - t_0 = \frac{1}{N'} T \left(1 - (1 - (at_0 + 1)e^{-at_0}) \right) - t_0 = \frac{T}{N'} (at_0 + 1)e^{-at_0} - t_0 \tag{5.13}$$

$$a_{j+1} = \left(\frac{T}{N'} (a_j t_0 + 1)e^{-a_j t_0} - t_0 \right)^{-1} \tag{5.14}$$

https://doi.org/10.7795/110.20260122

Equation 5.13 can be written in an iterative form, as Equation 5.14, since the refined $\frac{1}{a'}$ is only dependent on the unrefined $\frac{1}{a}$. As an initial value, a from the correction of first order in Equation 5.9 can be taken. When a_{j+1} has converged to a sufficient value a', the refined a' can finally be inserted into Equation 5.10.

$$N = N' e^{a' t_0} \tag{5.15}$$

The number N is the corrected, true number of events. Note that this is only valid, if a sharp limit t_0 can be defined for all waiting times. This is valid for most use cases.

5.3.3 Comparison with Dilution Series and Dead-Time Correction for Whole Blood

To test the waiting time correction, we can compare the results obtained with the current state of the art, a dilution series, and the dead-time correction. As described in the introduction of this chapter briefly, a dilution series with at least four different dilutions is extrapolated to infinite dilution. A dilution series can be seen as the "gold standard" in correcting coincidences for blood measurements. The number of measured events N' for a volume V_{sample} with dilution $\Phi = \frac{V_{\text{sample}}}{V_{\text{sample}}+V_{\text{dilution}}}$ is given as [16, 127]

$$N' = (N\Phi) \cdot \exp\left(\frac{-N\tau}{t}\Phi\right) \tag{5.16}$$

N is again the sought true number of events, t the measurement time and τ the cumulative dead time of the measurement setup. The cumulative dead time has to be measured and is unique for each measurement. The cumulative dead time is the summed up dead time after each event. This equation can only numerically be solved for N. To overcome this problem, Equation 5.16 can be written in the form:

$$\ln\frac{N'}{\Phi} = \ln N - \frac{N\tau}{t}\Phi \tag{5.17}$$

For infinite dilution ($\Phi \to 0$), it follows from Equation 5.16, that $\ln\frac{N'}{\Phi} \to \ln N$. When extrapolating different dilutions to zero, the term $\ln N$ can be determined. This also implies that the cumulative dead time is irrelevant for this method, since the last term in Equation 5.17 approaches zero at $\Phi \to 0$.

The dead-time correction tries to estimate the number of coincidences by the ratio of $\frac{\tau}{t}$. N' in Equation 5.16 is approximated by the first two terms of the Taylor series for the exponential function. Further, the term $\frac{N\tau}{t}$ is approximated by $\frac{N'\tau}{t}$. This means the dead-time correction is only accurate for high dilutions and low number of coincidences. Further, the equation assumes that the dead time after each measurement is constant. This is not the case anymore for the trigger mechanism used in this measurement setup. Here, the dead time is dependent on the pre and posttrigger length, which can vary from event to event. The variations are not significant, but it increases the approximation errors.

The benefit of the dead-time correction is that only a single measurement has to be done. This can be handy if only a small portion of the sample is available or the counting rates

https://doi.org/10.7795/110.20260122

are such low, that a further dilution would dramatically increase the measurement time for a dilution series. The number N of events then is given by

$$N \approx \frac{N'}{\Phi} \frac{1}{1 - \left(\frac{N'\tau}{t}\right)} \tag{5.18}$$

In Figure 5.30 the comparison of the three methods is depicted for whole blood. The measurement was done with a coulter counter[7]. The measurement principle is a little different, however the coulter counter (which is in fact also a cytometer) owes the same trigger mechanism as the used flow cytometer and the evaluation of the data does not differ from the evaluation of flow cytometry data.

Although for the dead-time correction and the waiting time correction only one measurement would suffice, all four measurements were evaluated with the respective methods. In theory all four measurements should yield the same value for the true number of events N. Every measurement was repeated $4-6$ times. The error bars visible for linear regression (i.e. dilution series) and dead time correction are according to the weighted (uncertainties in volume and counting rate are included) standard deviation in Equation 5.17 and Equation 5.18 respectively. For the waiting time correction only the unweighted standard deviation of the repeated measurements were taken, since a proper formulation of the error for the calculation of the corrected counting rate still has to be done. However the error is expected to be small.

The intersection at $\Phi = 0$ in Figure 5.30 and the corresponding counting rates are presented in Table 5.2. The counting rates obtained from the waiting-time correction and the dilution series agree very well. In contrast, the dead-time correction falls outside the uncertainty range of the waiting-time correction.

As previously mentioned, the dead-time correction is particularly susceptible to errors due to the non-constant dead time during the measurement process. The dilution series exhibits a larger uncertainty, as it requires fitting two parameters to a linear equation, whereas the waiting-time correction and dead-time correction involve fitting only a single constant parameter.

In practice, it was observed that a first-order correction is sufficient for the waiting-time correction in most cases. The second-order correction for the presented data amounted to approximately one digit in comparison to a total count of two million.

Table 5.2: measured counting rates as their interception with the ordinate including uncertainties. The uncertainty is given as the standard error of the linear fit process in Origin.

	waiting-time corr.	dead-time corr.	dilution series
interception with $\Phi = 0$	$14.50949 \pm 9.5 \cdot 10^{-4}$	$14.5124 \pm 1.5 \cdot 10^{-3}$	$14.5102 \pm 4.5 \cdot 10^{-3}$
counting rate	2001665 ± 1890	2007438 ± 2920	2003146 ± 8980

[7] In practice it is very difficult to acquire blood samples that can be used for publication. There were no suitable dilution series measurements available measured at the flow cytometer used in this thesis. Acquiring a new sample is a tedious process, including the consultation of an ethics council, which can take many months.

https://doi.org/10.7795/110.20260122

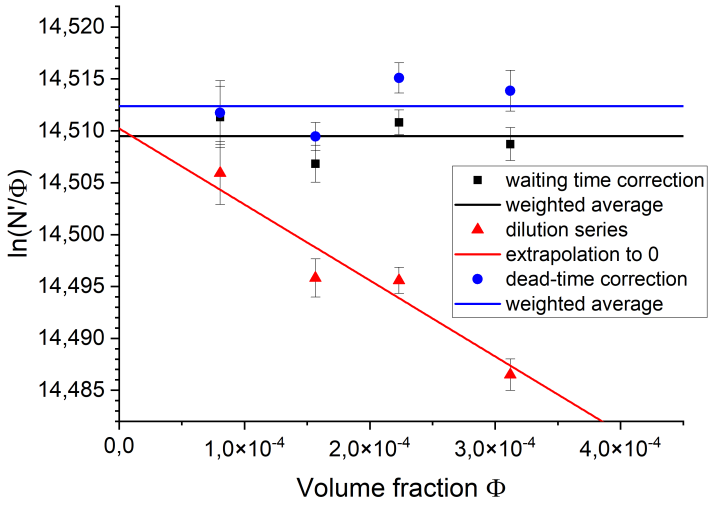

Figure 5.30: Comparison of the three coincidene correction methods: dead-time correction, dilution series and waiting-time correction.

5.3.4 Conclusion and Outlook

A novel algorithm for correcting measured counting rates with regard to coincidences has been presented. Unlike conventional methods, this algorithm neither relies on measuring the cumulative dead time nor requires a multi-step dilution series. In this work it has been proven that the algorithm is functional, however in future further comparison measurements should be carried out.

When comparing the waiting-time correction to the current state-of-the-art method — the dilution series — the measurement process is accelerated by at least a factor of four. This improvement arises because the dilution series requires a minimum of four different dilutions (not including preparation time). Consequently, the throughput of sample measurements, such as blood samples, is significantly enhanced, particularly in laboratories that depend on high-throughput analysis. In practice, waiting-time correction measurements are repeated to verify the results; however, for the dilution series, also several measurements are performed at each dilution and then averaged.

Although the dead-time correction method, in principle, requires only a single measurement, it has several disadvantages. These include the necessity to record the cumulative dead time and its inherent limitation to low counting rates. The dilution series and waiting time correction are able to correct coincidences hierarchical, meaning for several populations at once, which is of great benefit in hematology where there are always multiple components in the sample. For the dead-time correction this is not so clear. The populations can indeed be gated as well, however the corresponding dead times might not be correlated correctly. If coincidences between two populations occur, it is not obvious to which population the dead time has to be ascribed. To distinguish between two different coincidences a pulse shape analysis and temporal recording would be needed. Depending on the algorithm this might be a problem. These errors are usually small, but the general idea about coincidence correction is about being as correct as possible, which is why the errors should also be kept as small as possible.

https://doi.org/10.7795/110.20260122

The dilution series does not have this problem, since a change in dead-time only changes the slope of the graph in Figure 5.30, but not the intersection with the ordinate.

Another approach to coincidence correction is based on the mean waiting time between two consecutive events and the mean flight time [128]. Here, the waiting time is defined as the duration between the threshold crossing at the end of one pulse and the threshold crossing at the beginning of the next pulse. The mean waiting time and flight time are obtained by dividing their cumulative values by the number of recorded events. With instrument-specific parameters determined beforehand, a corrected event count and pulse height distribution can be calculated. However, this method does not allow for hierarchical coincidence correction, as the recorded flight and waiting times cannot be assigned to individual populations.

Importantly, the waiting-time correction algorithm is not limited to flow cytometry but can be applied to any measurement system that counts events following Poisson statistics e.g. in single photon counting. Interestingly Yu et. al. [129] reported on dead time and coincidences in single photon counting and concluded that if a dead time exists the statistic of the measurement does not obey Poissons law anymore, because there are events with short waiting times that can not be recorded. However, they relativized their statement in the end saying that "[...]statistical image reconstruction based on Poisson models, while certainly not optimal, should be adequate in practice even under fairly large deadtime losses [...]". They also concluded that the waiting time between two photons is distributed as in Figure 5.26 and that depending on the dead time there is a gap for short waiting times. Their correction model however is based on calculating the probability of a second event during the dead time. These are then included in the integral formulation of the first and second factorial moments yielding a correction formula.

The primary drawback of the waiting-time correction is that the measurement setup must be capable of determining the temporal distance between consecutive pulses. Currently, many commercial flow cytometers lack the capability to record event timestamps. Nevertheless, numerous laboratory setups have demonstrated that implementing such temporal recording is feasible if pursued by manufacturers. Additionally, concentration-dependent counting effects can only be recognized and addressed when measurements at different concentrations are performed.

If commercial devices become capable of recording the temporal distances between events, the author sees the potential that the presented algorithm could replace the current state-of-the-art for samples that have been proven to show no concentration-dependent effects. This will significantly accelerate and simplify laboratory routines.

https://doi.org/10.7795/110.20260122

6

Theoretical Implementation of a Quadrant Detector

In this chapter the concept of a quadrant detector in flow cytometry, with the ability to theoretically determine the asphericity of sub-wavelength sized particles will be explored by replacing the current PMT tubes in the forward scattering direction. Particles of sub-wavelength size can not be resolved with microscope objectives making it very difficult to measure any shape, especially with high throughput. However many application require such size and shape distributions, including wastewater sludge treatment [130, 131], nanoparticles in cosmetics [132, 133], aerosols in atmoshperic research [134–136] or in a broader sense even in interstellar clouds in astrophysics [137–139].

A similar, but more complex configuration to measure particle shapes has already been used by Moteki [140, 141] for single particle extinction and scattering (SPES) measurements [142–144]. They used a much smaller opening angle to detect the interference between forward scattered and incident laser light.

The previous chapter extracted more information about coincidences by analyzing the entire particle transit. However, to obtain shape information, a certain degree of spatial resolution is required. A quadrant detector is ideally suited for this application due to its widespread commercial availability, practicality [44, 45, 145] and routine use in applications such as electron microscopy and beam position monitoring. Esper-Chaín et. al. states that quadrant photo detectors are the best devices to measure laser beam positions, making them potentially suitable to measure slight far field deformations [46].

While alternative spatial detector orientations are possible, they would require bespoke design solutions. The basic concept, monitoring the full passage of the particle through the laser beam, remains the same, but with the introduction of a significant advancement: rather than registering a single temporal intensity progression for the entire detector, now individual intensity readings for each quadrant are obtained.

The design of the detector is illustrated in Figure 6.1. It features a circular detector, tilted by 45° in ϕ direction with an opening angle of θ_o (right quadrant spanning 315° to 45°, upper

https://doi.org/10.7795/110.20260122

quadrant from 45° to 135°, left quadrant between 135° and 225°, and the lower quadrant ranging from 225° to 315°). The far field shown belongs to a sphere (left) and an ellipsoid (right). It is clearly visible that for the ellipsoid, the vertical quadrants (up+down) contain a greater intensity than the horizontal (left+right) quadrants. A ratio of vertical/horizontal would be greater than one. Tilting the quadrants by 45° in ϕ direction is a key element, otherwise all quadrants would measure the same intensity (if the particles are aligned in flow direction, which goes right to left in Figure 6.1). Tilting the detector disrupts the symmetry for aspherical particles with axial symmetry (e.g. bisphere, rod, capsule, ellipsoid) that align with the direction of flow. From a practical point of view this also gives the ability to align the detector, laser and flow position by comparing the up and down intensity. The center of the detector shall be at $\theta = 0°$. The feasibility of the alignment is proven by the sources stated above.

The setup exploits the fact that aspherical particles posses an aspherical far field. For better understanding, the case of light diffraction on a slit with two axes can be considered. The smaller one axis, the wider the spread of the far field in this axis. The quadrant detector measures the ratio of the two farfield axes, which can serve as a measure of the aspect ratio of the slit i.e. particle.

The smaller the particle, the less aspheric the far field gets. The question now becomes, how small can the particles get until the ratio is nearly one and what relations can be utilized to characterize the asphericity of the particles.

To simulate the transit through the laser beam, at every relative beam-particle position x, a simulation of the scattered light is performed.

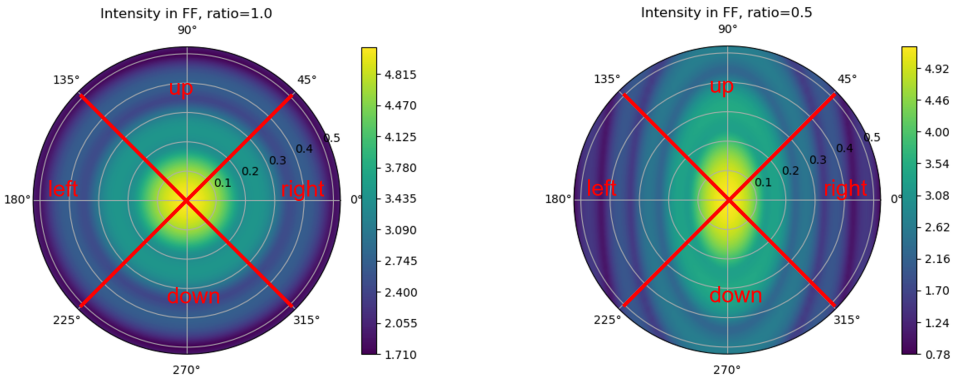

Figure 6.1: Quadrants sketched with far field scattering pattern of a sphere (left) and an ellipsoid (right) as example in the center of the laser beam. It is obvious to see that the vertical (up+down) quadrants contain more intensity than the horizontal (left+right). Angle ϕ shown in spherical direction. Arbitrary unit of opening angle θ_o in radial direction. The particles flow direction is from right to left.

Summation of the intensity of all quadrants, provides the scattering intensity scattered in the opening angle θ_o that is usually used in flow cytometry measurements. The total scattering intensity can be plotted against the beam position x, yielding a pulse shape. For particles of any shape and small in size compared to the beam diameter, the pulse shape of the total intensity usually has the same form as the beam profile. In contrast, by comparing the scattering intensity of the four quadrants with each other, different particle shapes give rise to distinct combined pulse shapes, making them distinguishable.

https://doi.org/10.7795/110.20260122

6.1 Simulation of Pulse Shapes for Aspherical Particles

All scattering simulations in this section were done with the ADDA code [77], using the amplitude scattering matrix S.The amplitude scattering matrix is read with Python and the scattered field calculated regarding a linearly polarized laser parallel to the flow direction. The scattered field is then integrated in the desired quadrants to receive the scattering intensity. At every beam position x, a full ADDA simulation must be done. Beneficial is, that the simulations for different positions are independent of each other and can therefore be parallelized trivially. Nevertheless, the total computation time can increase drastically with the size parameter, since a range of about 25 points in x direction is needed for a well-resolved pulse shape.

To describe the laser beam, the fifth-order Gaussian beam model by Barton et al. [65] is employed with waist radius $\omega_0 = 9\,\mu\text{m}$ and vacuo wavelength $\lambda_0 = 405\,\text{nm}$. An opening angle of 12° is chosen since this is also approximately the opening angle of the previously utilized device. The surrounding medium is water with a refractive index of $n_{\text{medium}} = 1.3431$ and the particles are assigned a refractive index of $n_{\text{particle}} = 1.6236$ (equal to that of polystyrene). The particles are sampled with 10 dipoles per wavelength. Compared to the Glare Point simulations the dipoles per wavelength were reduced, since here only the total intensity is of interest and not fine structures as with Glare Points. In their ADDA manual Yurkin et. al. state that even 10 dipoles per wavelength are sufficient for calculating images.

In an experiment it is challenging to handle the different dynamic range of the laser and the scattered intensity. In the context of flow cytometry this issue is overcome by introducing a beam-stop that blocks the direct laser beam in forward direction. To mimic this in the simulation, a spherical aperture with a radius of 3° was applied (i.e., θ starts at 3° in the simulation). This is also roughly the beamstop angle of the device.

In Figure 6.2 pulse shapes for four different particle shapes and three volumes (i.e. particle sizes) are shown. In each case, two opposite quadrants are added to obtain the vertical (up+down) and horizontal (left+right) intensity (see Figure 6.1). The particles are represented by predefined shapes in ADDA (sphere with diameter d, bisphere $R_{cc} = 1$, capsule $h = d$, rod as box with $\frac{y}{x} = 1$ and $\frac{z}{x} = 8$. Euler angles are set to $\alpha = 0°$, $\beta = 90°$, $\gamma = 0°$)[1].

The particles are oriented with their longest side towards the flow direction, as they tend to align in this manner within the flow, and this orientation is expected to produce the strongest changes in the signal. The four shapes have the following aspect ratios r [2]: sphere 1:1, bisphere 2:1, capsule 2:1, rod 8:1. The scatterer's volume and its geometrical cross-section usually have a strong influence on the scattered intensity. Hence, the size is expressed in terms of volume equivalent to a sphere with diameter d_{sphere} to better compare the different shapes. This is analogous to deforming a sphere to the respective shapes. This definition will continue throughout the whole chapter.

[1] A bisphere consists of two spheres with center-to-center radius of R_{cc}; therefore a $R_{cc} = 1$ means the two spheres are touching each other. A capsule is defined as two half spheres with diameter d attached to each plane surface of a cylinder with height h. A rod is a cuboid with aspect ratio $\frac{y}{x}$ and $\frac{z}{x}$. z defines the length of the longest side. A rod is a cuboid with aspect ratios $\frac{y}{x}$ and $\frac{z}{x}$, where z is the length of the longest side. Euler angles of $\alpha = 0°$, $\beta = 90°$, and $\gamma = 0°$ orient the z axis of the shape parallel to the x axis of the flow cytometer, aligning the longest side of the particles with the flow direction.

[2] longest side divided by shortest side, $r = \frac{x}{y}$ in the coordinate system of the flow cytometer (laser in z direction, flowing in x direction, y perpendicular to x,z)

https://doi.org/10.7795/110.20260122

The single sphere diameter d_{sphere} can be converted to the longest side of the mentioned shapes as follows:

$$d_{\text{bisphere}} = \frac{2}{\sqrt[3]{2}} \cdot d_{\text{sphere}} \approx 1.59 \cdot d_{\text{sphere}} \tag{6.1}$$

$$d_{\text{rod}} = \sqrt[3]{\frac{32\pi}{3}} \cdot d_{\text{sphere}} \approx 3.22 \cdot d_{\text{sphere}} \tag{6.2}$$

$$d_{\text{capsule}} = 2 \cdot \sqrt[3]{\frac{2}{5}} \cdot d_{\text{sphere}} \approx 1.47 \cdot d_{\text{sphere}} \tag{6.3}$$

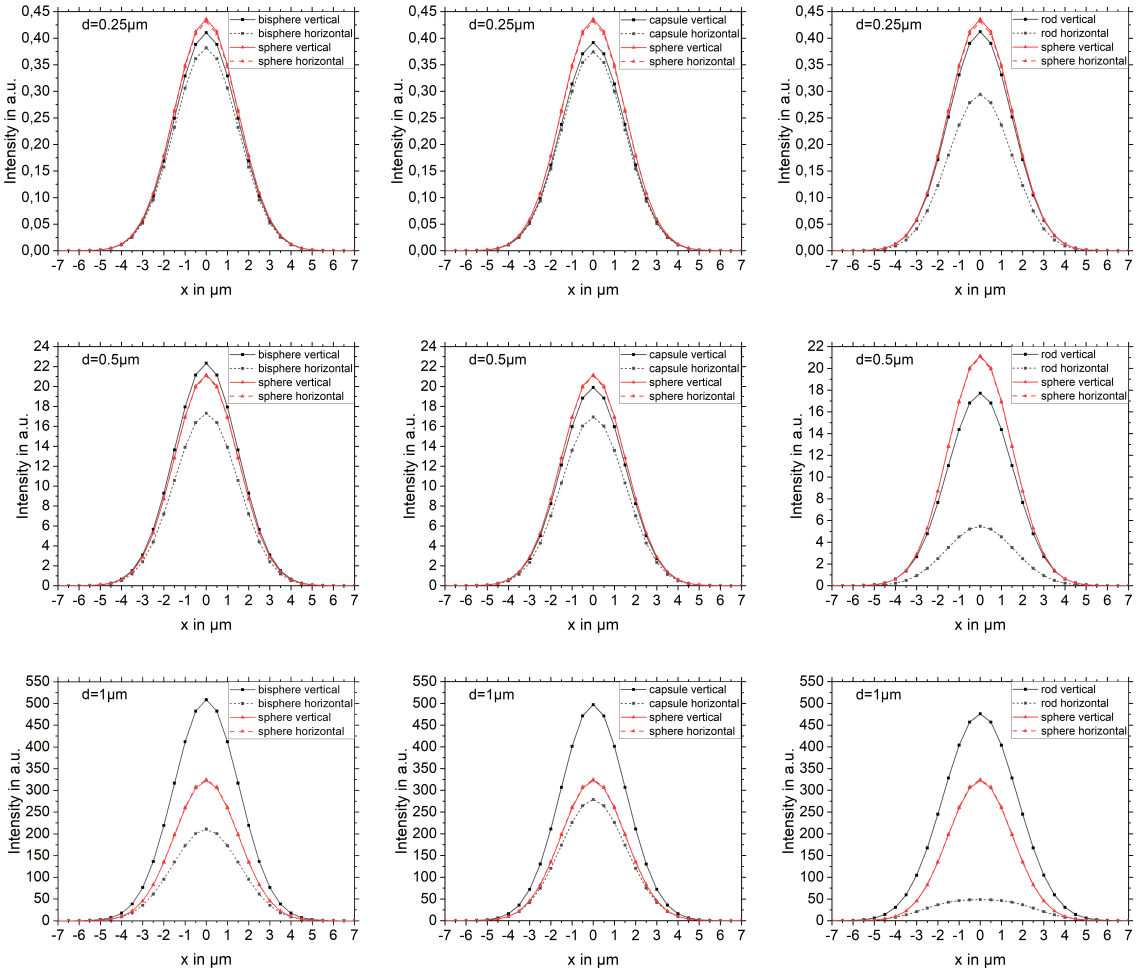

Figure 6.2: Pulse shapes of vertical (up+down) and horizontal (left+right) combination. The size is given in volume equivalent to a sphere with the diameter d_{sphere}.

In Figure 6.2 it is generally visible that the bigger the particle and the larger its aspect ratio, the more pronounced the difference becomes between vertical (up+down) and horizontal(left+right) intensity. This can be exploited to differentiate spherical and aspherical particles. Except for spheres of all sizes where significant difference between vertical and horizontal intensity is noted, with only a slight, negligible variation due to laser polarization.

As previously mentioned and clearly visible in Figure 6.2, the scattering intensity is strongly dependent on the scatterers size. To better compare different particle sizes one can e.g. form the ratio r of vertical and horizontal (referred to as simply 'ratio') intensity as depicted in

https://doi.org/10.7795/110.20260122

Figure 6.3. The ratio approach has several advantages. First, by taking the pairwise ratios of the intensities from two opposite quadrants, a wide range of particle volumes produce similar curves. Second, filters, amplifiers or parasitic effects that act linearly can be ignored. Additionally, it is easier to compare the unknown shape to a sphere, since a sphere has a ratio close to one. It is important to note again that these observations are made in the far-field, implying that an aspect ratio r greater than one results from an aspect ratio vertical/horizontal smaller than one of the particle.

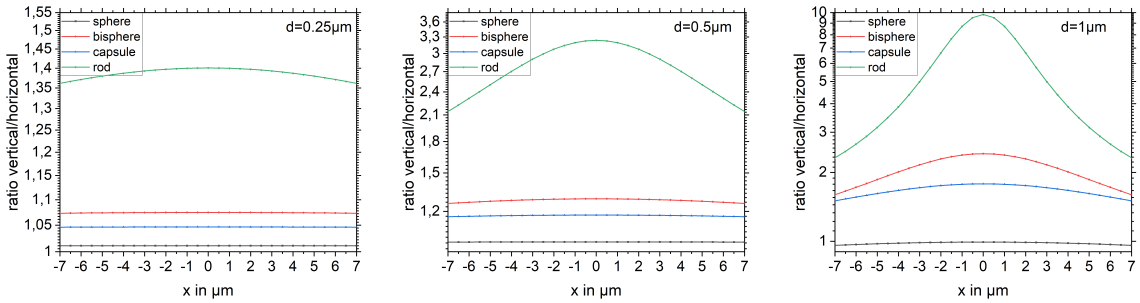

Figure 6.3: Ratio of vertical and horizontal signal shown for different shapes and sizes in logarithmic scale for an opening angle of 12°. The size is given in volume equivalent to a sphere with the diameter d_{sphere}.

It is evident from Figure 6.3 that the maximum ratio is achieved at $x = 0$ and for small particles, which are more of interest, the ratio resembles more a straight line than a pulse. Therefore for further analysis only the maximum ratio at $x = 0$ is considered. This also saves a lot of computation time. In an experiment it could still be beneficial to record the whole transit to better fit the maximum ratio. With only calculating the maximum ratio, a lot more computations of different sizes are possible. In Figure 6.4 the ratio r is plotted against different volume equivalent diameters d. As expected, the larger the particle and aspect ratio, the larger the ratio. This is an important relation for characterization. The ratio for a sphere is not perfectly one. For small particles the ratio is observed to be slightly above one, a phenomenon that can be attributed to polarization effects that intensify with smaller particles [3].

In contrast to that, in Figure 6.5, the relative total scattered intensity is plotted. With increasing size, the order of the shapes changes. At about 600 nm the intensity of the rod is about twice as high as that of a sphere with the same volume. If the shape is unknown, one could conclude that the particles either have different shape or a different volume. Both conclusions are valid. It is apparent that there is no consistent relationship between the maximum scattering intensity and the shape.

[3] see for example in Figure 6.10. The laser beam is polarized along $\phi = 0°$. This results in an induced dipole moment parallel to the laser beam polarization and more intensity scattered perpendicular to the dipole moment axis. The quadrants up and down (at 90° and 270°) contain therefore more intensity

https://doi.org/10.7795/110.20260122

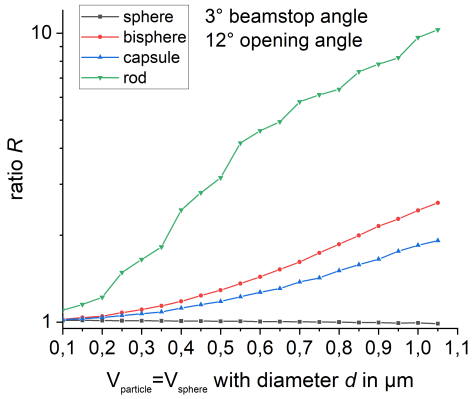

Figure 6.4: ratio r plotted against volume equivalent diameter of different particles. The ratio is plotted in logarithmic scale.

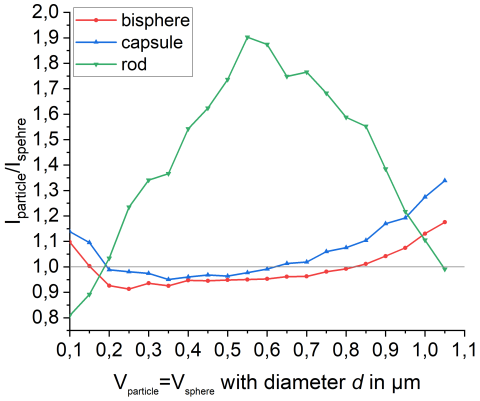

Figure 6.5: Intensity of aspherical particles in relation to the intensity of a volume equivalent sphere for different sizes.

Changes in the ratio with variations in the opening angle θ_o are particularly noteworthy, as demonstrated in Figure 6.6. The ratio of the non-spherical particles increases with increasing opening angle θ_o. For instance, increasing the opening angle from 12° to 30° increases the ratio of the capsule at d =250 nm from 1.047 to 1.28. This significantly facilitates the distinction of spheres and aspherical particles, underscoring the desirability of a larger opening angle, at least for small particles. However there seems to be a tipping point for large opening angles and particles at which the monotonously rising ratio seems to stop. Even the order of the bisphere and capsule change for large particles and opening angles of 20° and 30°. The explanation to this effect and how to avoid this will be explained in the next section.

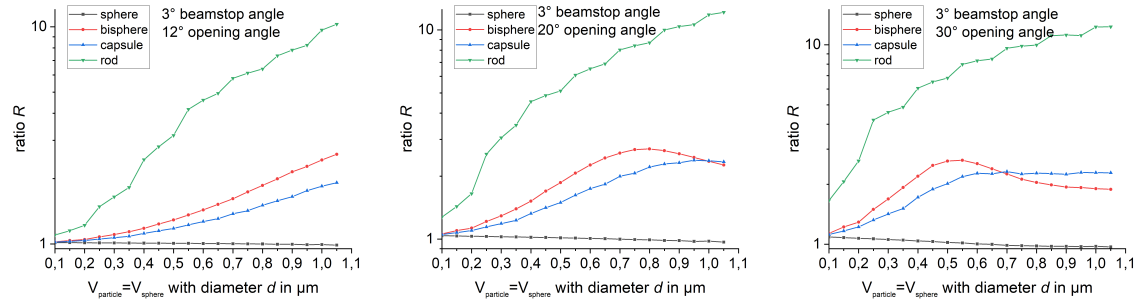

Figure 6.6: Ratio of vertical and horizontal shown for different shapes and sizes in logarithmic scale. The size is given in volume equivalent to a sphere with the diameter d.

6.2 Procedure of Characterization

When attempting to characterize particles by size and shape using this method, certain ambiguous cases arise. Initially, an estimation of the scattering volume by the scattering intensity, which is more sensitive to changes than the ratio, might be made. This can be achieved via determining a volume equivalent scattering volume of a sphere. Although the intensity can change by a factor of 2 or 3 compared to a sphere, the volume can still be estimated quite well, since the scattering intenstiy is heavily dependend on the scattering volume as visible in Figure 6.2.

https://doi.org/10.7795/110.20260122

For characterization purposes, only the maximum ratio at $x = 0$ is relevant. However, data points to the left and right of $x = 0$ can assist in interpolating. The ratio, while sensitive to different sizes as evidenced in Figure 6.3, is by far less sensitive than the intensity. Furthermore, the exact shape cannot be precisely reproduced; it only indicates a degree of 'asphericity' or aspect ratio. To conclude that the changes in the ratio are due to different aspect ratios, the rough size of the particles needs to be known before the analysis. Small variations in size, which usually occur, should not affect the ratio too much.

Based on previous measurements and experience, a measurement accuracy of 4% is assumed. With such a measurement accuracy, all particles and sizes could be distinguished from the corresponding sphere from up to d =250 nm in the simulation as seen in Figure 6.3. The bisphere and capsule, having the same aspect ratio but differing slightly in length, result in the capsule's peak potentially being slightly lower than that of the bisphere. According to the measurement accuracy, it would be feasible to differentiate capsules and bispheres if they are properly aligned.

However, particles do not align perfectly in the flow stream, leading to uncertainty about their orientation. To account for rotations, two angles are introduced: α, describing rotation around the laser axis, and β, indicating rotation in the laser-flow plane. A bisphere serves as a test particle.

At first the rotation around the α axis is looked at. This is a rather straightforward case as it is analogous to rotating the laser and detector. A rotation of the laser has only minor influence since the scattering pattern is only marginally dependent on the polarization. The dependency can be described with a sinus or cosine term as visible in Figure 6.9.

A rotation of the β angle is more complex. In Figure 6.7 the rotation of the β angle for different particle sizes and opening angles can be seen. Again, the particle sizes are chosen as volume equivalent to a sphere with the diameter d. It is observed that for 1 µm and 1.5 µm and opening angles of more than 20° the ratio does not rise monotonously. Also the order of the particles changes. From the measurement perspective it would be beneficial if the highest ratio is reached at $\beta = 90°$ for all parameter settings and if "the larger the aspect ratio of the particle, the larger the ratio R" is also true.

Explanation of non-monotonously rising ratio

To understand this behavior, the far-field scattering pattern of bispheres is considered, as shown in Figure 6.10. For the size d_{bisphere} of 400 nm, only the main maximum is visible within a 30° opening angle, and the minimum is excluded. Larger particles exhibit up to the main maximum, a second maximum, and the first one or two minima within the field of view. As the particle rotates from $\beta = 0°$ to $\beta = 90°$, increasing their projected aspect ratio in the laser field, the scattering pattern changes. The maxima along $\phi = 0$ shift to smaller angles, potentially moving in the field of view, increasing the intensity in the left and right quadrants. This leads to a decrease in the ratio r, well visible for d_{bisphere} =1.59 µm and d_{bisphere} =2.39 µm.

When varying sizes and a fixed opening angle the effect is similar. As the size increases, the maxima become denser, and side maxima may appear on the detector, altering the ratio. To avoid this, the opening angle θ_o should not exceed the scattering angle of the first minima along the shortest axes (corresponding to the longest axis in the near field).

https://doi.org/10.7795/110.20260122

To define an (analytical) estimation of such a criterion, the two axes of the geometrical cross section could be separated and the far field can be considered as a superposition of two far fields emerging from two small spheres with radii corresponding to the length of the axes. This of course will not resemble the exact field, but gives an estimate of the shortest axes angular diameter.

In the Rayleigh-Gans regime ($|m-1| \ll 1$ and $kd \cdot |m-1| \ll 1$) the form factor f can be expressed as follows for a particle with arbitrary shape as described in the book by Bohren & Huffmann [1]. The condition $|m-1| \ll 1$ is barely fulfilled with $m = 1.209$ for polystyrene. The condition $kd \cdot |m-1| < 1$ holds true for particles smaller than 230 nm. This is not fulfilled for most of the particles simulated, however it will still be used due to a lack of better alternatives.

$$f(\theta) = \frac{3}{u^3}\left(\sin(u) - u\cos(u)\right) \qquad u = 2x\sin\left(\frac{\theta}{2}\right) \tag{6.4}$$

The form factor f is zero if the condition $\tan(u) - u = 0$ holds true. The zeros are in good approximation given by the Expression 6.5

$$u_{\mathrm{n}}^2 = \left(n + \frac{1}{2}\right)\pi^2 - 2 \qquad \text{with } n \in \mathbb{N} \tag{6.5}$$

By finding the relation $\theta_{\mathrm{o}}(d)$ for the first minimum of the scattering distribution, a criterion for the maximum opening angle $\theta_{\mathrm{o}} = \theta_{\mathrm{n=1}}$ can be defined. For n=1 Equation 6.5 yields $u_1 = 4.49517... \approx 4.5$. Inserting u_1 into 6.4 gives Equation 6.6

$$d < \frac{4.5 \cdot \lambda}{2\pi \sin\left(\frac{\theta_o}{2}\right)} \Rightarrow \theta_o < 2 \cdot \arcsin\left(\frac{2.25\lambda}{\pi d}\right) \tag{6.6}$$

Note that the wavelength $\lambda = \frac{\lambda_0}{n_{\mathrm{medium}}}$ is the wavelength in the surrounding medium. In case θ_o is small, the condition $2\sin\left(\frac{\theta_o}{2}\right) = \sin\left(\theta_o\right)$ is valid which then reduces the Equation 6.6 to Abbes limit (see Equation 6.7) of resolving lines and grids with a prefactor of $\frac{9}{\pi}$. Recap that Abbes limit is defined as the distance at which the main diffraction maximum of the first object lies in the first diffraction minimum of the second object. Although Abbe considers two objects in a distance d compared to an object with diameter d mentioned above, the formulas are very similar.

$$d < \frac{\lambda}{\sin(\theta_o)} \Rightarrow \theta_o < \arcsin\left(\frac{\lambda}{d}\right) \tag{6.7}$$

Figure 6.8 shows a plot of equation 6.7 and 6.6. Plotted is the maximal opening angle θ_o versus the longest side of the particle.

The author is aware that this criterion is only a rough estimate, but simulations have shown it is quite feasible, even if the particles refractive index is not considered and the particle is too large for the Rayleigh approximation. By comparing Figures 6.4, 6.6,6.7 and 6.10 with Figure 6.8 the author concludes that Abbes limit underestimates and the limit derived from the form factor slightly overestimates the maximal opening angle θ. But in general it seems that the second criterion is in good agreement with the simulations.

A potential user of this setup can of course define their own refined criterion. A sophisticated model would be a numerical model containing the relative refractive index m, the particle size d

https://doi.org/10.7795/110.20260122

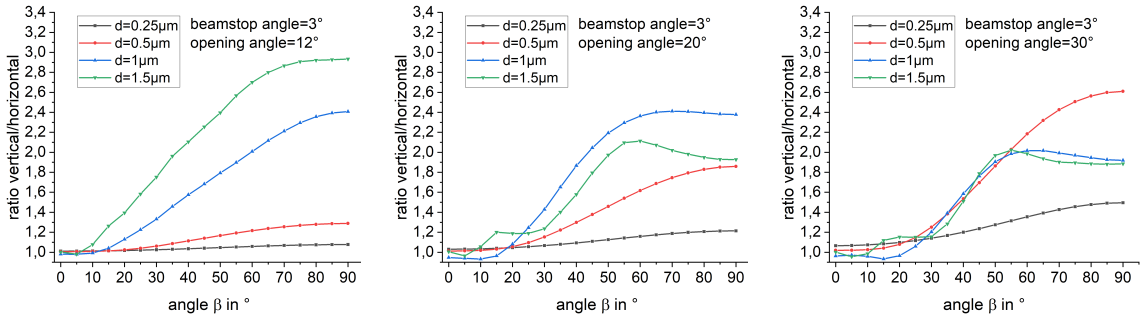

Figure 6.7: maximum ratio of vertical/horizontal plotted against the rotation angle β for different particle sizes. From left to right 12°,20°,30° of opening angle.

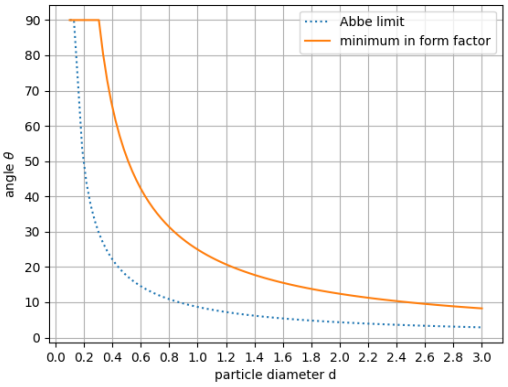

Figure 6.8: Equation 6.7 and 6.6 plotted

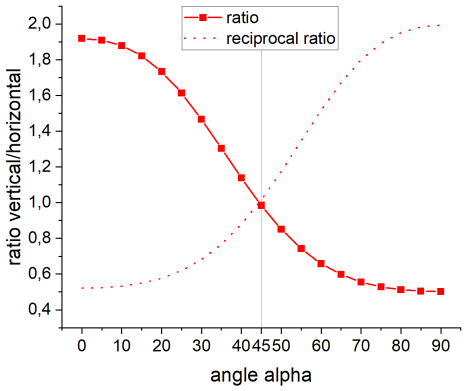

Figure 6.9: Change of the ratio vertical/horizontal versus rotation of the α angle around the laser axis.

and shape based probably on a finite-volume model. However, this can get very computational intense.

https://doi.org/10.7795/110.20260122

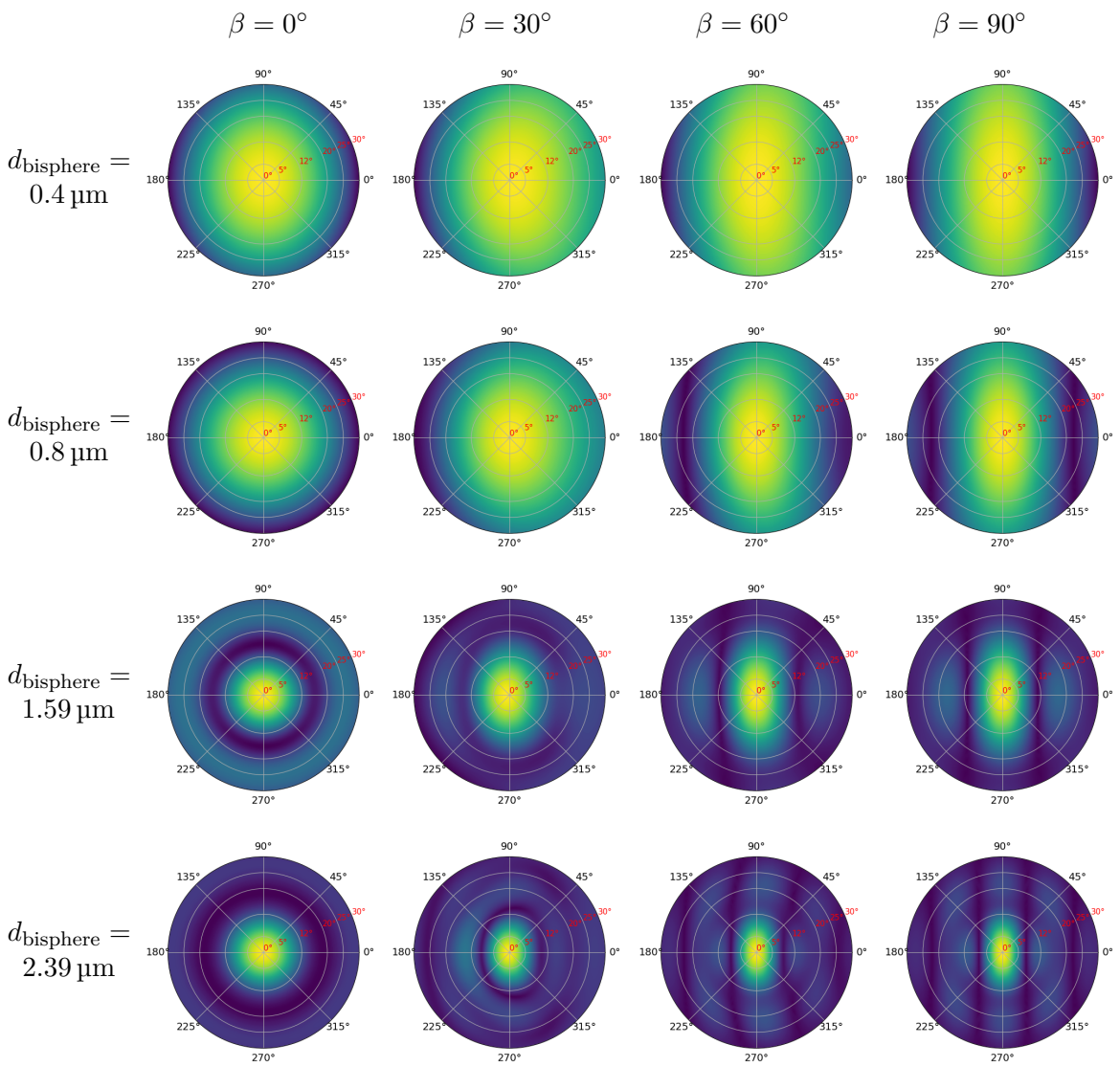

Figure 6.10: Scattered far-field pattern for bispheres with different diameters d_{bisphere} (i.e. length of longest side) and rotation β towards the laser. Volume equivalent diameters d_{sphere} are 0.25 µm, 0.5 µm, 1.0 µm and 1.5 µm. For better visibility the square root of the intensity is shown. Note that for $d_{\text{bisphere}} = 0.4\,\mu\text{m}$ the polarization effect of dipoles becomes visible.

6.3 Thoughts on Experimental Implementation and Outlook

When implementing the quadrant detector in the experiment, there are some additional challenges that needs to be discussed. It was theoretically shown that it is sufficient to record the maximum value, when the particle is in the center of the laser beam, of the ratio R. However, the accuracy of the measured maximum value could be further enhanced by fitting a polynomial to the whole recorded pulses of each quadrant, similar to Section 5.1.1. Since the signal at the end and beginning of the pulse is noisy and close to zero, forming the ratio of these leads to unsuitable results. To solve this problem, a cut-off time for the formation of the ratio should be defined.

Currently the experimental opening angle in forward direction is fixed at 12°. According to the analysis in this chapter, for a future setup, it would be useful to use an objective with a larger aperture to increase the sensitivity for small particles.

https://doi.org/10.7795/110.20260122

Another issue that needs to be addressed is an unknown particle orientation in the measurement, since the ratio R changes with particle rotation in flow. Fortunately, this problem can be mitigated for monodisperse suspensions by plotting the count numbers versus measured ratio R in a 1D histogram. It is known that the ratio R is maximal when the longest side of the particle is perfectly aligned in flow direction and minimal when it is shifted by 90° around the z axis (with respect to condition 6.7). The minimum ratio is the reciprocate of the maximum value. Using the histogram it is much easier to find the maximum and minimum possible ratio from the measurement, assuming that all orientation states are adopted. If all particles owe the same geometrical and optical properties, the maximum and minimum possible ratio represent the case of perfectly aligned particles. This value can then be analyzed and compared with simulations. When comparing the measured distribution of ratios to a theoretical uniformly distribution, orientation effects in the flow cell can estimated. Note that for particles approximately smaller than the wavelength it is no longer valid that a sphere obeys a ratio $R = 1$ due to polarization/dipole effects. However this is easy to estimate theoretically.

As a conclusion one can say that the presented detector design is in theory capable of distinguishing spherical particles and non-spherical particles in the sub-micrometer range. Unlike the simple intensity maximum, the relation in ratio (rod>bisphere>capsule>sphere) of vertical to horizontal intensity remains consistent across different sizes and opening angles if only the main maximum is present in the opening angle. With a large aperture, the distinction between e.g. bispheres and spheres should be feasible even for particles smaller than the wavelength, provided that the forward scattering signal is sufficiently strong for detection.

https://doi.org/10.7795/110.20260122

https://doi.org/10.7795/110.20260122

7

Summary

In this work, new measurement approaches were explored and introduced. However, before conducting any measurements, it is crucial to ensure that all relevant device parameters of the flow cytometer are well characterized. Determining these parameters is particularly challenging for the opening angles in the forward and sideward directions, as well as for the beam stop in the forward direction. While the numerical aperture of the lenses is typically well documented, it can be affected by the presence of additional optical components in the beam path, leading to a reduction in effective aperture and complicating precise angle measurements.

To address this challenge, a method was developed to determine these optical parameters by comparing the measured intensity of standardized polystyrene spheres with theoretically expected values. By analyzing a sufficiently large range of particle sizes, a distinct set of intensity ratios is obtained, which uniquely corresponds to the optical configuration of the system. The measured intensities can be mapped onto simulated values through a linear detector function. The optical parameters are then optimized using differential evolution, a statistical optimizer, to achieve a best-fit alignment between measured and simulated intensities. The scattering process is described by the Lorenz-Mie theory.

In the forward direction, this method proved to be effective. A numerical stable residual formulation was identified, which produces expected results, and exhibits low variance across repeated simulations. A beamstop angle of around $3.5 and opening angle of 12$ to $13 is assumed to be the correct value. The stablest residuum formulation found 3.7104 \pm 0.0031$ for the beamstop and $13.340 \pm 0.021 for the opening angle. An uncertainty of about 0.2$ is desired. However, due to the mentioned inherent uncertainties in parameter determination, it remains challenging to directly validate whether the extracted optical parameters match the actual system properties. In the sideward direction, while the method yields plausible results, repeated simulations exhibit substantial variance (i.e. more than tolerable). This variability is likely attributed to the pronounced sensitivity of side-scattered intensity to fluctuations in the opening angle. If this approach is validated as reliable, it has the potential to enable precise and efficient characterization of the flow cytometer with minimal effort, significantly enhancing the accuracy of particle property measurements.

https://doi.org/10.7795/110.20260122

Typically, flow cytometers utilize a photomultiplier tube to detect scattered light as a single intensity value. However, advancements in camera technology now enable the direct imaging of scattered light. In this work, a rigorous imaging model was employed to simulate these scattering images. Previous studies in related fields have relied on paraxial approximations, using methods such as the Fresnel diffraction integral or Fourier transformation as imaging models. Furthermore, most prior works applied geometrical optics rather than the numerically exact Lorenz-Mie theory.

Here, the scattering process is modeled using Lorenz-Mie theory for spherical particles. The scattered light is propagated towards a single lens, where its phase is transformed according to an ideal lens model. The imaging process itself is rigorously described by the Rayleigh-Sommerfeld diffraction integral.

When imaging spheres in the sideward direction, the particle does not appear as a simple spherical outline but instead exhibits two or more bright spots, known in other fields as *Glare Points*. It could be shown in this work that the bright spots observed in flow cytometry are in fact Glare Points. The simulated images reproduce the observed Glare Point structures well for polystyrene particles with diameters of 3 µm, 5 µm, and 10 µm.

By systematically varying the particle size and relative refractive index, resonances in the extinction efficiency Q_{ext} were identified. It was observed that the structure of the Glare Points undergoes significant changes when sweeping the relative refractive index m across a resonance.

To extend the model to aspherical particles, the discrete-dipole approximation was introduced. Using this approach, deformed particles— stretched or compressed—were theoretically examined for polystyrene and for a lower relative refractive index of $m = 1.04$, which corresponds well to biological tissue. Several scattering features emerged, including vertical stripes along the laser propagation direction and surface spots in the case of polystyrene. It was discussed on whether these surface spots originate from surface waves. While a definitive conclusion could not be reached, the observed effects are fully captured within the discrete-dipole approximation, regardless of their physical origin.

In commercial flow cytometers, only a single parameter per event—such as the maximum intensity or pulse area—is typically recorded. In this work, an alternative approach was pursued: recording the entire transit of a particle or cell through the laser, generating a one-dimensional intensity-versus-time pulse. This data is stored and post-processed to extract additional event characteristics.

It was demonstrated that by fitting the pulse data, both the intensity maximum and its exact temporal position could be determined with higher accuracy. Key extracted parameters include the maximum intensity, its temporal position, pulse area, standard deviation, skewness, kurtosis and the temporal distance to consecutive pulses.

Using the standard deviation, coincidences of same sized particles could be detected with significantly higher reliability. These coincidences would remain indistinguishable in conventional histograms based solely on maximum intensity or pulse area.

https://doi.org/10.7795/110.20260122

By modeling particle agglomerates and closely spaced coincidences, it was found that agglomerates exhibit lower pulse area and peak intensity than two separate coincidences due to interference effects. An upper boundary for distinguishing agglomerates was identified, which is beneficial for correcting counting statistics and improving sample preparation.

The inclusion of skewness allowed for the identification of most coincidences involving differently sized particles in polydisperse suspensions. These events are undetectable using conventional maximum intensity or pulse area histograms when the intensity contribution of the smaller particle is dominated by that of the larger one. The algorithm was successfully validated using suspensions of 1 µm and 5 µm polystyrene particles, as well as with thrombocytes and erythrocytes in whole blood.

A key advantage of this approach is that it does not rely on Poisson-distributed event rates, unlike traditional methods such as dead-time correction or dilution series analysis. Furthermore, it enables the identification of individual coincident pulses and can be extended to other counting measurement techniques that yield a temporally resolved, approximately Gaussian-shaped signal.

If the counting process follows Poisson statistics, coincidences can be corrected by using the exponentially distributed waiting times between consecutive events. In the presence of a dead time, waiting times shorter than the dead time are not recorded and instead appear as coincidences within other events.

To correct for this, the average waiting time $\langle t \rangle$ is measured for all events exceeding a defined cutoff time t_0 (where t_0 is greater than the dead time). From this, the mean waiting time $\frac{1}{a}$ for all measurements can be inferred in first correction. A second correction compensates for a systematic overestimation of the total waiting times due to undetected coincidences. Using the corrected mean waiting time $\frac{1}{a}$, the statistically correct total event count can be determined.

A comparison with dilution series and dead-time correction methods demonstrated that the waiting-time correction provides reliable results. A major advantage of this approach is that only a single measurement is required, in contrast to the four measurements needed for a dilution series. Furthermore, different particle populations can be gated and corrected separately using this algorithm.

The method is not limited to flow cytometry but is applicable to any event-counting system that follows Poisson statistics, such as single-photon counting. However, a key limitation is that the measurement setup must be capable of precisely determining the temporal distances between consecutive events, a feature that many commercial flow cytometers lack. Additionally, concentration-dependent counting effects can only be identified and addressed through dilution series measurements. For samples that have been verified to exhibit no concentration-dependent effects, this method has the potential to replace the current state-of-the-art dilution series approach.

Finally, the theoretical feasibility of using a quadrant photodetector as an alternative to the currently employed photomultiplier tube was evaluated for its ability to extract shape information of particles. To this end, simulations of the far-field intensity distribution were

https://doi.org/10.7795/110.20260122

conducted using the ADDA software, and the ratio R of the signals from the tilted horizontal to vertical quadrants as a measure of asphereness was analyzed.

The results indicate that a quadrant detector can provide a measure of both aspect ratio and size, even for particles smaller than the wavelength. A higher numerical aperture leads to an increased ratio R, thereby enhancing sensitivity to variations in aspect ratio. While the total scattered intensity depends on the particle's aspect ratio, this dependence is not consistent across different particle sizes when compared to a sphere.

In contrast to that, the relative ordering of aspect ratios for different particle types is preserved in the ratio R across the entire tested size range from 100 nm to 1100 nm for an opening angle of 12°. The upper size limit decreases for larger opening angles; however, this does not pose an issue. The numerical aperture must then be selected to match the particle size: large opening angles are suited for small particles, while small opening angles are better for large particles.

The theoretical analysis suggests that a quadrant detector could enable efficient differentiation between spherical and aspherical particles, even for sub-wavelength-sized particles, while also providing an estimate of the aspect ratio of the sample. An experimental validation is still pending.

https://doi.org/10.7795/110.20260122

Hilfsmittel

In dieser Arbeit wurde das Programm "ChatGPT" der Firma "OpenAI" als Hilfsmittel verwendet. Es wurde in der Version "GPT-4o" zur sprachliche Überprüfung und Verbesserung der Texte genutzt. Es wurden keine von Grund auf neu generierten Texte verwendet.

https://doi.org/10.7795/110.20260122

https://doi.org/10.7795/110.20260122

References

[1] C. F. Bohren and D. R. Huffman. *Absorption and Scattering of Light by Small Particles*. Wiley, 1983.

[2] S. I. Hajdu. **A note from history: The discovery of blood cells**. *Ann. Clin. Lab. Sci.*, **33**(2):237–238, 2003.

[3] I. M. Davis. **"Round, red globules floating in a crystalline fluid" – Antoni van Leeuwenhoek's observations of red blood cells and hemocytes**. *Micron*, **157**:103249, June 2022. doi:10.1016/j.micron.2022.103249.

[4] G. I. C. Ingram and P. M. Mannucci. **William Hewson and the blood which issued last but clotted first: the beginning of the story of desmopressin in haemophilia and vWD**. *Haemophilia*, **2**(3):180–183, July 1996. doi:10.1111/j.1365-2516.1996.tb00164.x.

[5] K. R. Kampen. **The discovery and early understanding of leukemia**. *Leukemia Research*, **36**(1):6–13, January 2012. doi:10.1016/j.leukres.2011.09.028.

[6] W. Coulter. **Means for counting particles suspended in a fluid**, 1953. [Online; last accessed 20-Feb-2025].

[7] Y. Song, H. Zhang, and M. Li. *Microfluidic Resistive Pulse Sensor*, page 1993–2000. Springer New York, 2015. doi:10.1007/978-1-4614-5491-5_1711.

[8] **Beckman Couter - Multisizer-4e**. [Online; last accessed 20-Feb-2025].

[9] M. R. Melamed. *Chapter 1 A brief history of flow cytometry and sorting*, page 3–17. Elsevier, 2001. doi:10.1016/s0091-679x(01)63005-x.

[10] J. P. Robinson. **Flow Cytometry: Past and Future**. *BioTechniques*, **72**(4):159–169, April 2022. doi:10.2144/btn-2022-0005.

[11] S. M. Manohar, P. Shah, and A. Nair. **Flow Cytometry: Principles, Applications and Recent Advances**. *Bioanalysis*, **13**(3):181–198, February 2021. doi:10.4155/bio-2020-0267.

[12] R. G. Ashcroft and P. A. Lopez. **Commercial high speed machines open new opportunities in high throughput flow cytometry (HTFC)**. *Journal of Immunological Methods*, **243**(1–2):13–24, September 2000. doi:10.1016/s0022-1759(00)00219-2.

[13] J. F. Keij, A. V. Rotterdam, A. C. Groenewegen, W. Stokdijk, and J. W. M. Visser. **Coincidence in high-speed flow cytometry: Models and measurements**. *Cytometry*, **12**(5):398–404, January 1991. doi:10.1002/cyto.990120504.

[14] H. M. Shapiro. *Practical Flow Cytometry*. John Wiley & Sons, Inc., 2003.

[15] A. Adan, G. Alizada, Y. Kiraz, Y. Baran, and A. Nalbant. **Flow cytometry: basic principles and applications**. *Critical Reviews in Biotechnology*, **37**(2):163–176, January 2016. doi:10.3109/07388551.2015.1128876.

https://doi.org/10.7795/110.20260122

[16] M. Kammel, A. Kummrow, and J. Neukammer. **Reference measurement procedures for the accurate determination of cell concentrations: present status and future developments/Referenzmessverfahren für die genaue Bestimmung von Zellkonzentrationen: Status und zukünftige Entwicklungen**. *LaboratoriumsMedizin*, **36**(1), January 2012. doi:10.1515/jlm-2011-0008.

[17] K. M. McKinnon. **Flow Cytometry: An Overview**. *Current Protocols in Immunology*, **120**(1), January 2018. doi:10.1002/cpim.40.

[18] S. M. Lewis, J. M. England, and F. Kubota. **Coincidence correction in red blood cell counting**. *Physics in Medicine and Biology*, **34**(9):1239–1246, September 1989. doi:10.1088/0031-9155/34/9/009.

[19] H. Bader, H. R. Gordon, and O. B. Brown. **Theory of Coincidence Counts and Simple Practical Methods of Coincidence Count Correction for Optical and Resistive Pulse Particle Counters**. *Review of Scientific Instruments*, **43**(10):1407–1412, October 1972. doi:10.1063/1.1685455.

[20] J. England. **Reference method for the enumeration of erythrocytes and leucocytes**. *Clinical and Laboratory Haematology*, **16**(2):131–138, June 2008. doi:10.1111/j.1365-2257.1994.tb00399.x.

[21] S. Lekhtmakher and M. Shapiro. **Registration Probabilities and Pulse-Height Distributions of Coincidences in Optical Particle Counters**. *Aerosol Science and Technology*, **38**(2):155–164, February 2004. doi:10.1080/02786820490250827.

[22] A. Corp. [Online; last accessed 29-Jan-2025]. [link].

[23] P. Morrissey, T. George, D. Basiji, K. Frost, W. Ortyn, and D. Williams. **Cell Classification in Human Peripheral Blood Using the Amnis ImageStream® System.** *Blood*, **104**(11):3826–3826, November 2004. doi:10.1182/blood.v104.11.3826.3826.

[24] T. C. George, D. A. Basiji, B. E. Hall, D. H. Lynch, W. E. Ortyn, D. J. Perry, M. J. Seo, C. A. Zimmerman, and P. J. Morrissey. **Distinguishing modes of cell death using the ImageStream® multispectral imaging flow cytometer**. *Cytometry Part A*, **59A**(2):237–245, May 2004. doi:10.1002/cyto.a.20048.

[25] D. A. Basiji. *Principles of Amnis Imaging Flow Cytometry*, page 13–21. Springer New York, November 2015. doi:10.1007/978-1-4939-3302-0_2.

[26] G. Warnes and S. Martins. **Real-time flow cytometry for the kinetic analysis of oncosis**. *Cytometry Part A*, **79A**(3):181–191, January 2011. doi:10.1002/cyto.a.21022.

[27] J. A. Sebastian, M. J. Moore, E. S. L. Berndl, and M. C. Kolios. **An image-based flow cytometric approach to the assessment of the nucleus-to-cytoplasm ratio**. *PLOS ONE*, **16**(6):e0253439, June 2021. doi:10.1371/journal.pone.0253439.

[28] F. Marchetti and P. Morrissey. *Sperm Scoring Using Multi-Spectral Flow Imaging and FISH-IS Final Report CRADA No. TC02088.0*. September 2017. doi:10.2172/1399741.

[29] C. C. Martin, C. Jayat-Vignoles, J.-L. Faucher, T. George, V. Venkatachalam, P. Morrissey, and J. Feuillard. **Novel Multiparametric Quantitative Immunocytomorphological Characterisation of Human Bone Marrow Precursor Differentiation and of Haematopoietic Neoplasms Using ImageStream® Cytometry**. *Blood*, **112**(11):4871–4871, November 2008. doi:10.1182/blood.v112.11.4871.4871.

[30] S. E. Headland, H. R. Jones, A. S. V. D'Sa, M. Perretti, and L. V. Norling. **Cutting-Edge Analysis of Extracellular Microparticles using ImageStreamX Imaging Flow Cytometry**. *Scientific Reports*, **4**(1), June 2014. doi:10.1038/srep05237.

[31] T. Tertel and B. Giebel. **Amnis ImageStream - Analysis of individual extracellular vesicles by imaging flow cytometry**. *Cytotherapy*, **22**(5):S55, May 2020. doi:10.1016/j.jcyt.2020.03.075.

https://doi.org/10.7795/110.20260122

[32] D. Basiji. **Multispectral Imaging in Flow: A Technique for**. *Flow cytometry for biotechnology*, page 57, 2005.

[33] P. Goktas, I. O. Sukharevsky, S. Larkin, F. A. Kuypers, O. Yalcin, and A. Altintas. **Image-Based Flow Cytometry and Angle-Resolved Light Scattering to Define the Sickling Process**. *Cytometry Part A*, **95**(5):488–498, April 2019. doi:10.1002/cyto.a.23756.

[34] S. Arnold, S. Holler, J. H. Li, A. Serpengüzel, W. F. Auffermann, and S. C. Hill. **Aerosol particle microphotography and glare-spot absorption spectroscopy**. *Opt. Lett.*, **20**(7):773–775, Apr 1995. doi:10.1364/OL.20.000773.

[35] R. Meng, J. Xu, and B. Ge. **Diffraction glare points: principle and application in particle sizing**. *Opt. Express*, **26**(18):22816–22825, Sep 2018. doi:10.1364/OE.26.022816.

[36] M. Fayngold. **Spherical particle imaging and glare-ring spectroscopy with backscattered light**. *J. Opt. Soc. Am. A*, **14**(8):1825–1835, Aug 1997. doi:10.1364/JOSAA.14.001825.

[37] M. Mokbel, D. Mokbel, A. Mietke, N. Träber, S. Girardo, O. Otto, J. Guck, and S. Aland. **Numerical Simulation of Real-Time Deformability Cytometry To Extract Cell Mechanical Properties**. *ACS Biomaterials Science & Engineering*, **3**(11):2962–2973, January 2017. doi:10.1021/acsbiomaterials.6b00558.

[38] Z. Dresden. [Online; last accessed 03-Feb-2025]. [link].

[39] B. Lincoln, H. M. Erickson, S. Schinkinger, F. Wottawah, D. Mitchell, S. Ulvick, C. Bilby, and J. Guck. **Deformability-based flow cytometry**. *Cytometry Part A*, **59A**(2):203–209, May 2004. doi:10.1002/cyto.a.20050.

[40] O. Otto, P. Rosendahl, A. Mietke, S. Golfier, C. Herold, D. Klaue, S. Girardo, S. Pagliara, A. Ekpenyong, A. Jacobi, M. Wobus, N. Töpfner, U. F. Keyser, J. Mansfeld, E. Fischer-Friedrich, and J. Guck. **Real-time deformability cytometry: on-the-fly cell mechanical phenotyping**. *Nature Methods*, **12**(3):199–202, February 2015. doi:10.1038/nmeth.3281.

[41] L. Van der Meeren, J. Verduijn, D. V. Krysko, and A. G. Skirtach. **High-throughput mechano-cytometry as a method to detect apoptosis, necroptosis, and ferroptosis**. *Cell Proliferation*, **56**(6), March 2023. doi:10.1111/cpr.13445.

[42] D. Kage, K. Heinrich, K. v. Volkmann, J. Kirsch, K. Feher, C. Giesecke-Thiel, and T. Kaiser. **Multi-angle pulse shape detection of scattered light in flow cytometry for label-free cell cycle classification**. *Communications Biology*, **4**(1), September 2021. doi:10.1038/s42003-021-02664-3.

[43] D. Kage, A. Eirich, K. Heinrich, J. Kirsch, J. Popien, A. Wolf, K. v. Volkmann, H.-D. Chang, and T. Kaiser. **Cell sorting based on pulse shapes from angle resolved detection of scattered light**. *Communications Biology*, **7**(1), August 2024. doi:10.1038/s42003-024-06759-5.

[44] Q. Liu, S. Zhang, X. Ren, B. Wang, C. Liu, A. Hu, and X. Guo. **A Positioning Method Based on Large-Area Four-Quadrant Photodetector**. *IEEE Photonics Technology Letters*, **35**(18):975–977, September 2023. doi:10.1109/lpt.2023.3292432.

[45] L. M. Manojlović. **Quadrant photodetector sensitivity**. *Applied Optics*, **50**(20):3461, July 2011. doi:10.1364/ao.50.003461.

[46] R. Esper-Chain, A. Medina Escuela, D. Farina, and J. R. Sendra. **Configurable Quadrant Photodetector: An Improved Position Sensitive Device**. *IEEE Sensors Journal*, **16**(1):109–119, January 2016. doi:10.1109/jsen.2015.2475597.

[47] J. Zhao and Z. You. **Microfluidic hydrodynamic focusing for high-throughput applications**. *Journal of Micromechanics and Microengineering*, **25**(12):125006, October 2015. doi:10.1088/0960-1317/25/12/125006.

https://doi.org/10.7795/110.20260122

[48] R. Scott, P. Sethu, and C. K. Harnett. **Three-dimensional hydrodynamic focusing in a microfluidic Coulter counter**. *Review of Scientific Instruments*, **79**(4), April 2008. doi:10.1063/1.2900010.

[49] Y. Hein, F. Zipfel, G. O'Connor, R. Macdonald, and M. Hussels. **Flow cytometer for a dilution-free measurement approach with sample recollection**. *Review of Scientific Instruments*, **95**(6), June 2024. doi:10.1063/5.0187052.

[50] M. D. Ward and G. Kaduchak. **Fundamentals of Acoustic Cytometry**. *Current Protocols in Cytometry*, **84**(1), April 2018. doi:10.1002/cpcy.36.

[51] G. Goddard, J. C. Martin, S. W. Graves, and G. Kaduchak. **Ultrasonic particle-concentration for sheathless focusing of particles for analysis in a flow cytometer**. *Cytometry Part A*, **69A**(2):66–74, January 2006. doi:10.1002/cyto.a.20205.

[52] N. I. Corp. [Online; last accessed 29-Jan-2025]. [link].

[53] M. Daimon and A. Masumura. **Measurement of the refractive index of distilled water from the near-infrared region to the ultraviolet region**. *Appl. Opt.*, **46**(18):3811–3820, Jun 2007. doi:10.1364/AO.46.003811.

[54] G. Mie. **Beiträge zur Optik trüber Medien, speziell kolloidaler Metallösungen ⟨ger.⟩ [Contributions to the optics of turbid media, particularly of colloidal metal solutions]**. *Annalen der Physik*, **330**(3):377–445, 1908.

[55] J. R. Frisvad and H. Kragh. **On Ludvig Lorenz and his 1890 treatise on light scattering by spheres**. *The European Physical Journal H*, **44**(2):137–160, July 2019. doi:10.1140/epjh/e2019-100022-y.

[56] P. Debye. **Der Lichtdruck auf Kugeln von beliebigem Material**. *Annalen der Physik*, **335**(11):57–136, January 1909. doi:10.1002/andp.19093351103.

[57] H. C. van de Hulst. *Light scattering by small particles*. John Wiley & Sons, Inc., 1957.

[58] H. Horvath. **Gustav Mie and the scattering and absorption of light by particles: Historic developments and basics**. *Journal of Quantitative Spectroscopy and Radiative Transfer*, **110**(11):787–799, July 2009. doi:10.1016/j.jqsrt.2009.02.022.

[59] T. Wriedt. *Mie Theory: A Review*, page 53–71. Springer Berlin Heidelberg, 2012. doi:10.1007/978-3-642-28738-1_2.

[60] A. Ungut, G. Grehan, and G. Gouesbet. **Comparisons between geometrical optics and Lorenz-Mie theory**. *Applied Optics*, **20**(17):2911, September 1981. doi:10.1364/ao.20.002911.

[61] J. C. Gienger. *Determination of optical and geometrical properties of blood cells and microparticles from light scattering measurements [Doctoral Thesis]*. Phd thesis, Technische Universität Berlin, 2019.

[62] G. Gouesbet and G. Grehan. **On the scattering of light by a Mie scatter center located on the axis of an axisymmetric light profile**. *Journal of Optics*, **13**(2):97–103, March 1982. doi:10.1088/0150-536x/13/2/006.

[63] G. Gouesbet and G. Gréhan. *Generalized Lorenz-Mie Theories*. Springer International Publishing, 2023. doi:10.1007/978-3-031-25949-4.

[64] G. Gouesbet, G. Grehan, and B. Maheu. **On the generalized Lorenz-Mie theory: first attempt to design a localized approximation to the computation of the coefficients gnm**. *Journal of Optics*, **20**(1):31–43, January 1989. doi:10.1088/0150-536x/20/1/004.

https://doi.org/10.7795/110.20260122

[65] J. P. Barton and D. R. Alexander. **Fifth-order corrected electromagnetic field components for a fundamental Gaussian beam**. *Journal of Applied Physics*, **66**(7):2800–2802, October 1989. doi:10.1063/1.344207.

[66] S. Prahl. **miepython: Pure python calculation of Mie scattering**, 2024. [Online; last accessed 20-Feb-2025]. doi:10.5281/ZENODO.14257432.

[67] H. DeVoe. **Optical Properties of Molecular Aggregates. I. Classical Model of Electronic Absorption and Refraction**. *The Journal of Chemical Physics*, **41**(2):393–400, July 1964. doi:10.1063/1.1725879.

[68] H. DeVoe. **Optical Properties of Molecular Aggregates. II. Classical Theory of the Refraction, Absorption, and Optical Activity of Solutions and Crystals**. *The Journal of Chemical Physics*, **43**(9):3199–3208, November 1965. doi:10.1063/1.1697294.

[69] E. M. Purcell and C. R. Pennypacker. **Scattering and Absorption of Light by Nonspherical Dielectric Grains**. *The Astrophysical Journal*, **186**:705, December 1973. doi:10.1086/152538.

[70] S. B. Singham and G. C. Salzman. **Evaluation of the scattering matrix of an arbitrary particle using the coupled dipole approximation**. *The Journal of Chemical Physics*, **84**(5):2658–2667, March 1986. doi:10.1063/1.450338.

[71] S. B. Singham and C. F. Bohren. **Light scattering by an arbitrary particle: a physical reformulation of the coupled dipole method**. *Optics Letters*, **12**(1):10, January 1987. doi:10.1364/ol.12.000010.

[72] B. T. Draine. **The discrete-dipole approximation and its application to interstellar graphite grains**. *The Astrophysical Journal*, **333**:848, October 1988. doi:10.1086/166795.

[73] B. T. Draine and P. J. Flatau. **Discrete-Dipole Approximation For Scattering Calculations**. *Journal of the Optical Society of America A*, **11**(4):1491, April 1994. doi:10.1364/josaa.11.001491.

[74] A. Lakhtakia. **strong and weak forms of the method and the coupled dipole method for scattering of time-harmonic electromagnetic fields**. *International Journal of Modern Physics C*, **03**(03):583–603, 1992. doi:https://doi.org/10.1142/S0129183192000385.

[75] M. Yurkin and A. Hoekstra. **The discrete dipole approximation: An overview and recent developments**. *Journal of Quantitative Spectroscopy and Radiative Transfer*, **106**(1–3):558–589, July 2007. doi:10.1016/j.jqsrt.2007.01.034.

[76] P. C. Chaumet. **The Discrete Dipole Approximation: A Review**. *Mathematics*, **10**(17):3049, August 2022. doi:10.3390/math10173049.

[77] M. A. Yurkin and A. G. Hoekstra. **The discrete-dipole-approximation code ADDA: Capabilities and known limitations**. *Journal of Quantitative Spectroscopy and Radiative Transfer*, **112**(13):2234 – 2247, 2011. doi:https://doi.org/10.1016/j.jqsrt.2011.01.031.

[78] F. Kahnert. **Numerical methods in electromagnetic scattering theory**. *Journal of Quantitative Spectroscopy and Radiative Transfer*, **79–80**:775–824, June 2003. doi:10.1016/s0022-4073(02)00321-7.

[79] M. Huntemann, G. Heygster, and G. Hong. **Discrete dipole approximation simulations on GPUs using OpenCL—Application on cloud ice particles**. *Journal of Computational Science*, **2**(3):262–271, August 2011. doi:10.1016/j.jocs.2011.05.011.

[80] M. Yurkin. [Online; last accessed 16-Jan-2025]. [link].

[81] L. Wang and R. A. Hoffman. **Standardization, Calibration, and Control in Flow Cytometry**. *Current Protocols in Cytometry*, **79**(1), January 2017. doi:10.1002/cpcy.14.

https://doi.org/10.7795/110.20260122

[82] S. P. Perfetto, D. Ambrozak, R. Nguyen, P. K. Chattopadhyay, and M. Roederer. **Quality assurance for polychromatic flow cytometry using a suite of calibration beads**. *Nature Protocols*, **7**(12):2067–2079, November 2012. doi:10.1038/nprot.2012.126.

[83] W. CHANDLER, W. YEUNG, and J. TAIT. **A new microparticle size calibration standard for use in measuring smaller microparticles using a new flow cytometer**. *Journal of Thrombosis and Haemostasis*, **9**(6):1216–1224, June 2011. doi:10.1111/j.1538-7836.2011.04283.x.

[84] J. A. Welsh, J. C. Jones, and V. A. Tang. **Fluorescence and Light Scatter Calibration Allow Comparisons of Small Particle Data in Standard Units across Different Flow Cytometry Platforms and Detector Settings**. *Cytometry Part A*, **97**(6):592–601, June 2020. doi:10.1002/cyto.a.24029.

[85] V. Ost, J. Neukammer, and H. Rinneberg. **Flow cytometric differentiation of erythrocytes and leukocytes in dilute whole blood by light scattering**. *Cytometry*, pages 191–7, July 1998.

[86] E. van der Pol, F. Coumans, A. Grootemaat, C. Gardiner, I. Sargent, P. Harrison, A. Sturk, T. van Leeuwen, and R. Nieuwland. **Particle size distribution of exosomes and microvesicles determined by transmission electron microscopy, flow cytometry, nanoparticle tracking analysis, and resistive pulse sensing**. *Journal of Thrombosis and Haemostasis*, **12**(7):1182–1192, July 2014. doi:10.1111/jth.12602.

[87] L. de Rond, F. A. W. Coumans, R. Nieuwland, T. G. van Leeuwen, and E. van der Pol. **Deriving Extracellular Vesicle Size From Scatter Intensities Measured by Flow Cytometry**. *Current Protocols in Cytometry*, **86**(1), August 2018. doi:10.1002/cpcy.43.

[88] W. W. Woud, H. R. Pugsley, B. A. Bettin, Z. Varga, and E. van der Pol. **Size and fluorescence calibrated imaging flow cytometry: From arbitrary to standard units**. *Cytometry Part A*, **105**(10):752–762, September 2024. doi:10.1002/cyto.a.24895.

[89] J. A. L. Kenneth V. Price, Rainer M. Storn. *Differential Evolution*. Springer-Verlag, 2005. doi:10.1007/3-540-31306-0_2.

[90] P. N. Suganthan. *Differential Evolution Algorithm: Recent Advances*, page 30–46. Springer Berlin Heidelberg, 2012. doi:10.1007/978-3-642-33860-1_4.

[91] R. Storn. **On the usage of differential evolution for function optimization**. In *Proceedings of North American Fuzzy Information Processing*, NAFIPS-96. IEEE, 1996. doi:10.1109/nafips.1996.534789.

[92] J. A. Lock. **Theory of the observations made of high-order rainbows from a single water droplet**. *Appl. Opt.*, **26**(24):5291–5298, Dec 1987. doi:10.1364/AO.26.005291.

[93] H. C. van de Hulst and R. T. Wang. **Glare points**. *Appl. Opt.*, **30**(33):4755–4763, Nov 1991. doi:10.1364/AO.30.004755.

[94] S. A. Schaub, D. R. Alexander, and J. P. Barton. **Glare spot image calculations for a spherical particle illuminated by a tightly focused beam**. *J. Opt. Soc. Am. A*, **9**(2):316–330, Feb 1992. doi:10.1364/JOSAA.9.000316.

[95] K. F. Ren, G. Gouesbet, G. Géhan, D. Lebrun, C. Özkul, and A. Kleitz. **On the measurements of particles by imaging methods: Theoretical and Experimental Aspects**. *Particle & Particle Systems Characterization*, **13**(2):156–164, 1996. doi:https://doi.org/10.1002/ppsc.19960130215.

[96] C. Probst, Y. Zeng, and R.-R. Zhu. **Characterization of Protein Particles in Therapeutic Formulations Using Imaging Flow Cytometry**. *Journal of Pharmaceutical Sciences*, **106**(8):1952–1960, August 2017. doi:10.1016/j.xphs.2017.04.034.

[97] I. D. Nikolov and C. D. Ivanov. **Optical plastic refractive measurements in the visible and the near-infrared regions**. *Appl. Opt.*, **39**(13):2067–2070, May 2000. doi:10.1364/AO.39.002067.

https://doi.org/10.7795/110.20260122

[98] J. Gienger, M. Bär, and J. Neukammer. **Extinction spectra of suspensions of microspheres: determination of the spectral refractive index and particle size distribution with nanometer accuracy**. *Appl. Opt.*, **57**(2):344–355, Jan 2018. doi:10.1364/AO.57.000344.

[99] S. Dehaeck and J. P. A. J. van Beeck. **Simultaneous determination of bubble diameter and relative refractive index using glare circles**. *Appl. Opt.*, **46**(23):5957–5963, Aug 2007. doi:10.1364/AO.46.005957.

[100] J. A. Lock. **Interference enhancement of the internal fields at structural scattering resonances of a coated sphere**. *Applied Optics*, **29**(21):3180, July 1990. doi:10.1364/ao.29.003180.

[101] P. Chýlek, J. T. Kiehl, and M. K. W. Ko. **Narrow resonance structure in the Mie scattering characteristics**. *Applied Optics*, **17**(19):3019, October 1978. doi:10.1364/ao.17.003019.

[102] A. Ashkin and J. M. Dziedzic. **Observation of Resonances in the Radiation Pressure on Dielectric Spheres**. *Physical Review Letters*, **38**(23):1351–1354, June 1977. doi:10.1103/physrevlett.38.1351.

[103] A. B. Stilgoe, T. A. Nieminen, G. Knöener, N. R. Heckenberg, and H. Rubinsztein-Dunlop. **The effect of Mie resonances on trapping in optical tweezers**. *Optics Express*, **16**(19):15039, September 2008. doi:10.1364/oe.16.015039.

[104] H. S. Bennett and G. J. Rosasco. **Resonances in the efficiency factors for absorption: Mie scattering theory**. *Applied Optics*, **17**(4):491, February 1978. doi:10.1364/ao.17.000491.

[105] R. M. Waxler and G. Cleek. **The effect of temperature and pressure on the refractive index of some oxide glasses**. *Journal of Research of the National Bureau of Standards Section A: Physics and Chemistry*, **77A**(6):755, November 1973. doi:10.6028/jres.077a.046.

[106] Dehaeck, Sam. *Development of glare point, shadow and interferometric planar techniques for gas bubble sizing / Sam Dehaeck.* PhD thesis, Ghent University, 2007.

[107] Lock and Selmke. **Glare Points and Near-Zone Sagittal Caustic for Scattering of a Plane Wave by a Spherical or Spheroidal Bubble Floating in Air**. In *Laser-light and Interactions with Particles (LIP2022)*, LIP2022. Institute of Physics, Polish Academy of Sciences, Warsaw, Poland, 2022, 2022.

[108] N. Bezugla, O. Romodan, P. Komada, N. Stelmakh, and M. Bezuglyi. **Fundamentals of Determination of the Biological Tissue Refractive Index by Ellipsoidal Reflector Method**. *Photonics*, **11**(9):828, September 2024. doi:10.3390/photonics11090828.

[109] R. E. Durand and P. L. Olive. **Cytotoxicity, Mutagenicity and DNA damage by Hoechst 33342.** *Journal of Histochemistry and Cytochemistry*, **30**(2):111–116, February 1982. doi:10.1177/30.2.7061816.

[110] P. R. Turner and W. A. Denny. **The mutagenic properties of DNA minor-groove binding ligands**. *Mutation Research/Fundamental and Molecular Mechanisms of Mutagenesis*, **355**(1–2):141–169, August 1996. doi:10.1016/0027-5107(96)00027-9.

[111] **Patent:US4447883A**.

[112] L. Wheeless, J. Hardy, and N. Balasubramanian. **Slit-scan flow system for automated cytopathology**. *Acta cytologica*, **19**(1):45—52, 1975.

[113] J. L. Cambier, D. B. Kay, and L. L. Wheeless. **A multidimensional slit-scan flow system.** *Journal of Histochemistry and Cytochemistry*, **27**(1):321–324, January 1979. doi:10.1177/27.1.374595.

[114] C. van Oven and J. A. Aten. **Instrument for real-time pulse-shape analysis of slit-scan flow cytometry signals**. *Cytometry*, **11**(5):630–635, January 1990. doi:10.1002/cyto.990110511.

https://doi.org/10.7795/110.20260122

[115] N. A. Zilmer, M. Godavarti, J. J. Rodriguez, T. A. Yopp, G. M. Lambert, and D. W. Galbraith. **Flow cytometric analysis using digital signal processing**. *Cytometry*, **20**(2):102–117, June 1995. doi:10.1002/cyto.990200203.

[116] M. Godavarti, J. J. Rodriguez, T. A. Yopp, G. M. Lambert, and D. W. Galbraith. **Automated particle classification based on digital acquisition and analysis of flow cytometric pulse waveforms**. *Cytometry*, **24**(4):330–339, August 1996. doi:10.1002/(sici)1097-0320(19960801)24:4<330::aid-cyto4>3.0.co;2-j.

[117] M. Hussels, S. Engel, and N. Bock. **Investigation of direct counting and sizing of DNA fragments in flow applying an improved data analysis and correction method**. *Biomolecular Detection and Quantification*, **17**:100083, March 2019. doi:10.1016/j.bdq.2019.100083.

[118] A. I. Barreda, H. Saleh, A. Litman, F. Gonzalez, J.-M. Geffrin, and F. Moreno. **On the scattering directionality of a dielectric particle dimer of High Refractive Index**. *Scientific Reports*, **8**(1), May 2018. doi:10.1038/s41598-018-26359-8.

[119] G. Trefalt, I. Szilagyi, T. Oncsik, A. Sadeghpour, and M. Borkovec. **Probing Colloidal Particle Aggregation by Light Scattering**. *CHIMIA*, **67**(11):772, November 2013. doi:10.2533/chimia.2013.772.

[120] H. Lichtenfeld, H. Stechemesser, and H. Möhwald. **Single particle light-scattering photometry—some fields of application**. *Journal of Colloid and Interface Science*, **276**(1):97–105, August 2004. doi:10.1016/j.jcis.2004.03.038.

[121] H. Yu, H. Park, Y. Kim, M. W. Kim, and Y. Park. **Fourier-transform light scattering of individual colloidal clusters**. *Optics Letters*, **37**(13):2577, June 2012. doi:10.1364/ol.37.002577.

[122] C.-L. Shen and Y.-F. Wu. **Flow cytometry for evaluating platelet immunophenotyping and function in patients with thrombocytopenia**. *Tzu Chi Medical Journal*, **34**(4):381–387, October 2022. doi:10.4103/tcmj.tcmj_117_22.

[123] G. L. Salvagno, M. Montagnana, M. Degan, P. L. Marradi, M. M. Ricetti, P. Riolfi, G. Poli, P. Minuz, C. L. Santonastaso, and G. C. Guidi. **Evaluation of platelet turnover by flow cytometry**. *Platelets*, **17**(3):170–177, January 2006. doi:10.1080/09537100500437851.

[124] O. Garraud and F. Cognasse. **Are Platelets Cells? And if Yes, are They Immune Cells?** *Frontiers in Immunology*, **6**, February 2015. doi:10.3389/fimmu.2015.00070.

[125] G. A. Morton. **Photon Counting**. *Applied Optics*, **7**(1):1, January 1968. doi:10.1364/ao.7.000001.

[126] C. Santori, D. Fattal, J. Vučković, G. S. Solomon, and Y. Yamamoto. **Indistinguishable photons from a single-photon device**. *Nature*, **419**(6907):594–597, October 2002. doi:10.1038/nature01086.

[127] P. W. Helleman. **Quality control in blood cell analysis**. *Comparative Haematology International*, **1**(1):21–28, February 1991. doi:10.1007/bf00422689.

[128] **Patent:US6744245**.

[129] D. F. Yu and J. A. Fessler. **Mean and variance of single photon counting with deadtime**. *Physics in Medicine and Biology*, **45**(7):2043–2056, June 2000. doi:10.1088/0031-9155/45/7/324.

[130] J. E. Weaver, J. C. Williams, J. J. Ducoste, and F. L. de los Reyes III. **Measuring the Shape and Size of Activated Sludge Particles Immobilized in Agar with an Open Source Software Pipeline**. *Journal of Visualized Experiments*, (143), January 2019. doi:10.3791/58963-v.

[131] J. Wu, X. Jiang, and A. Wheatley. **Characterizing activated sludge process effluent by particle size distribution, respirometry and modelling**. *Desalination*, **249**(3):969–975, December 2009. doi:10.1016/j.desal.2009.06.061.

https://doi.org/10.7795/110.20260122

[132] P. Yupapin and P. Suwandee. **Nano-particles for Cosmetic Use: Particle Sizing, Cytotoxicity Test, and Facial Gesture Monitoring Model**. *Journal of Cosmetology and Trichology*, **2**(2), 2016. doi:10.4172/2471-9323.1000112.

[133] D. G. e. Silva, F. D. Sarruf, L. C. D. d. Oliveira, E. P. G. Arêas, T. M. Kaneko, V. O. Consiglieri, M. V. R. Velasco, and A. R. Baby. **Influence of particle size on appearance and in vitro efficacy of sunscreens**. *Brazilian Journal of Pharmaceutical Sciences*, **49**(2):251–261, June 2013. doi:10.1590/s1984-82502013000200007.

[134] K. Goto-Azuma, Y. Ogawa-Tsukagawa, K. Fukuda, K. Fujita, M. Hirabayashi, R. Dallmayr, J. Ogata, N. Moteki, T. Mori, S. Ohata, Y. Kondo, M. Koike, S. Matoba, M. Kadota, A. Tsushima, N. Nagatsuka, and T. Aoki. **High-resolution analyses of concentrations and sizes of refractory black carbon particles deposited in northwestern Greenland over the past 350 years – Part 2: Seasonal and temporal trends in refractory black carbon originated from fossil fuel combustion and biomass burning**. *Atmospheric Chemistry and Physics*, **25**(1):657–683, January 2025. doi:10.5194/acp-25-657-2025.

[135] M. Kahnert, T. Nousiainen, and H. Lindqvist. **Review: Model particles in atmospheric optics**. *Journal of Quantitative Spectroscopy and Radiative Transfer*, **146**:41–58, October 2014. doi:10.1016/j.jqsrt.2014.02.014.

[136] P. Kollias, B. A. Albrecht, and F. Marks. **Why Mie?: Accurate Observations of Vertical Air Velocities and Raindrops Using a Cloud Radar**. *Bulletin of the American Meteorological Society*, **83**(10):1471–1484, October 2002. doi:10.1175/bams-83-10-1471.

[137] E. Costantini, M. J. Freyberg, and P. Predehl. **Absorption and scattering by interstellar dust: an XMM-Newton observation of Cyg X-2**. *Astronomy and Astrophysics*, **444**(1):187–200, November 2005. doi:10.1051/0004-6361:20042562.

[138] A. J. Brown. **Spectral bluing induced by small particles under the Mie and Rayleigh regimes**. *Icarus*, **239**:85–95, September 2014. doi:10.1016/j.icarus.2014.05.042.

[139] F. Hoyle and C. Wickramasinghe. **On The Nature of Interstellar Grains**. *Astrophysics and Space Science*, **268**(1/3):249–261, 1999. doi:10.1023/a:1002462602776.

[140] N. Moteki. **Capabilities and limitations of the single-particle extinction and scattering method for estimating the complex refractive index and size-distribution of spherical and non-spherical submicron particles**. *Journal of Quantitative Spectroscopy and Radiative Transfer*, **243**:106811, March 2020. doi:10.1016/j.jqsrt.2019.106811.

[141] N. Moteki. **Measuring the complex forward-scattering amplitude of single particles by self-reference interferometry: CAS-v1 protocol**. *Optics Express*, **29**(13):20688, June 2021. doi:10.1364/oe.423175.

[142] F. Mariani, V. Bernardoni, F. Riccobono, R. Vecchi, G. Valli, T. Sanvito, B. Paroli, A. Pullia, and M. A. C. Potenza. **Single Particle Extinction and Scattering allows novel optical characterization of aerosols**. *Journal of Nanoparticle Research*, **19**(8), August 2017. doi:10.1007/s11051-017-3995-3.

[143] M. A. C. Potenza, T. Sanvito, and A. Pullia. **Accurate sizing of ceria oxide nanoparticles in slurries by the analysis of the optical forward-scattered field**. *Journal of Nanoparticle Research*, **17**(2), February 2015. doi:10.1007/s11051-015-2925-5.

[144] M. A. C. Potenza, Z. Krpetic, T. Sanvito, Q. Cai, M. Monopoli, J. M. de Araujo, C. Cella, L. Boselli, V. Castagnola, P. Milani, and K. A. Dawson. **Detecting the shape of anisotropic gold nanoparticles in dispersion with single particle extinction and scattering**. *Nanoscale*, **9**(8):2778–2784, 2017. doi:10.1039/c6nr08977a.

[145] M. Castello, C. J. R. Sheppard, A. Diaspro, and G. Vicidomini. **Image scanning microscopy with a quadrant detector**. *Optics Letters*, **40**(22):5355, November 2015. doi:10.1364/ol.40.005355.

https://doi.org/10.7795/110.20260122

Bundesministerium
für Wirtschaft
und Energie

Die Physikalisch-Technische Bundesanstalt, das nationale Metrologieinstitut, ist eine wissenschaftlich-technische Bundesoberbehörde im Geschäftsbereich des Bundesministeriums für Wirtschaft und Energie.

Physikalisch-Technische Bundesanstalt
Nationales Metrologieinstitut
ISNI: 0000 0001 2186 1887

Bundesallee 100
38116 Braunschweig

Presse- und Öffentlichkeitsarbeit

Telefon: (0531) 592-93 21
Fax: (0531) 592-30 08
E-Mail: presse@ptb.de
www.ptb.de

https://doi.org/10.7795/110.20260122